QCD-driven dark matter: AQNs formation and observational tests

Ludovic Van Waerbeke

November 14, 2026

Contents

1 Introduction **3**

2 A critical perspective on model-independent constraints **4**
2.1 Where is dark matter ? . . . 4
2.2 How dark is dark matter ? . . . 5
2.3 Cold dark matter . . . 6
2.4 Collisionless dark matter . . . 7
2.5 Dark matter interactions with baryons and photons . . . 8
2.6 Observational constrains from Big Bang Nucleosynthesis . . . 10
2.7 An overlooked hypothesis: rare dark matter . . . 10
2.8 Bayesian perspectives on dark-matter models . . . 11

3 Confronting QCD-AQN to observations **13**
3.1 AQNs structure and properties . . . 13
3.2 Cosmological behaviour of AQNs: cold and collisionless . . . 15
3.3 Radiative signatures of A$\overline{\text{Q}}$Ns in dilute environments . . . 16
3.3.1 A$\overline{\text{Q}}$N-baryon capture cross-section in dilute media . . . 17
3.3.2 A$\overline{\text{Q}}$Ns emission in a predominatly neutral, dilute medium . . . 18
3.3.3 A$\overline{\text{Q}}$Ns emission in an ionised dilute medium . . . 20
3.4 Observations in dilute environments . . . 21
3.4.1 A$\overline{\text{Q}}$Ns contribution to the sky monopole . . . 21
3.4.2 A$\overline{\text{Q}}$Ns and South Pole Telescope observations . . . 22
3.4.3 A$\overline{\text{Q}}$Ns and Galactic UV background observations . . . 23
3.4.4 A$\overline{\text{Q}}$Ns and CMB observations . . . 25
3.5 A$\overline{\text{Q}}$Ns interactions with dense objects . . . 25
3.5.1 Example 1: the Sun . . . 26
3.5.2 Example 2 : the Earth . . . 27
3.5.3 Example 3: neutron-stars . . . 27
3.5.4 Additional constrains on the mean A$\overline{\text{Q}}$N mass . . . 28
3.5.5 Synthesis of observational constraints . . . 29
3.6 Upcoming tests for the QCD-AQN framework . . . 30
3.6.1 511 keV emission in the Galactic bulge . . . 30
3.6.2 Cosmic dawn and 21-cm cosmology . . . 31
3.6.3 ARCADE 2 and the cosmic radio background . . . 31
3.6.4 Where and how to search for A$\overline{\text{Q}}$N signatures . . . 32
3.7 Prediction: the dark glow . . . 33

3.8 AQN detection on Earth (2026 update) . . . 35

4 AQNs in the early Universe **36**
4.1 AQN formation . . . 36
4.2 Matter-antimatter asymmetry . . . 41
4.3 AQNs remarkable stability . . . 42
4.4 Photon to baryon ratio, η . . . 43
4.5 Primordial ^{7}Li abundance . . . 44
4.6 AQN mass distribution . . . 45
4.6.1 AQN mass range at formation freeze-out . . . 45
4.6.2 A mass distribution constrained by observations . . . 47
4.7 Two inflation scenarios . . . 48
4.8 Broadening the dark-matter paradigm . . . 49

5 The QCD axion **49**
5.1 QCD axion mass range . . . 50
5.2 Other types of axions . . . 51
5.3 Current and upcoming experiments . . . 52
5.4 The importance of inflation in axion cosmology . . . 53
5.4.1 Axion mass and inflation . . . 53
5.4.2 Inflationary Hubble scale upper bound . . . 54
5.5 Dark matter as a two-component system . . . 55

6 Conclusion **56**

References **57**

1 Introduction

Since the pioneering work of Fritz Zwicky in the 1930s Zwicky (1933), the quest to understand the nature of dark matter (DM) has stood at the centre of modern cosmology. Subsequent observations – from the rotation curves measured by Vera Rubin Rubin and Ford (1970); Rubin et al. (1980) to the precision cosmology of Planck – have transformed DM into a cornerstone of the standard cosmological model. Yet despite overwhelming evidence for its existence, the nature of DM remains one of the most profound open questions at the intersection of cosmology and particle physics Cirelli et al. (2024); Di Valentino et al. (2025). One of the striking facts is that its abundance is so close to that of ordinary matter:

$$\Omega_{\rm DM} \approx 5\,\Omega_b.$$

Within the standard paradigm, there is no structural reason for the two densities to be comparable: The visible baryon[1] population is generated through a high-scale baryogenesis mechanism, while dark matter is produced independently.

The QCD–AQN framework, developed by Ariel R. Zhitnitsky Zhitnitsky (2003), proposes a different interpretation rooted in quantum chromodynamics (QCD) and matter–antimatter symmetry. The foundational idea emerged in part from earlier work by Witten (1984); Madsen et al. (1986); Lugones and Horvath (2004): aggregates of condensed quark matter carrying a large baryon number in the colour superconducting phase may become stable against decay into ordinary hadronic matter at temperatures $T \lesssim 60\,\mathrm{MeV}$.

In this framework, the Universe may remain globally symmetric,

$$B_{\rm universe} = B_{\rm matter} + \bar{B}_{\rm antimatter} = 0,$$

where B is the baryon number.

During the QCD transition at $T \sim 170\,\mathrm{MeV}$, a baryon-charge separation mechanism gives rise to the formation of quark and antiquark aggregates, known as Axion Quark Nuggets (AQNs), with a dynamical imbalance favouring the antimatter AQNs. The visible sector consists of the leftover unbound baryons. Because both AQN dark matter and the visible baryons emerge from the same underlying QCD dynamics, their present-day mass densities are correlated. Being remarkably stable, AQNs survive to the present epoch and, owing to their macroscopic masses and consequent rarity, have so far evaded direct detection.

The conceptual shift is significant:

- DM abundance is a consequence of QCD-scale physics;
- The photon-to-baryon ratio is controlled by the QCD binding scale of the Color Superconducting phase;
- Matter–antimatter symmetry is preserved globally;
- One additional fundamental particle is involved, the QCD axion.

A major strength of the framework lies in its multi-wavelength testability and its clear falsifiability. Subsequent studies by several authors have examined how AQN–baryon interactions may produce observable signatures across a wide range of astrophysical environments, through electromagnetic emission and/or localised energy deposition.

This lecture begins with an overview of the current observational constraints on dark matter, with a strong emphasis on distinguishing firmly established results from model-dependent interpretations (Section 2), and on highlighting regions of the DM parameter space to which

[1] When dealing with condensed matter, baryon (B) will be understood stricto sensu as a composite hadron made of three quarks bound together by the strong interaction ($B = +1$, e.g. protons and neutrons). In cosmology, baryons (b) are defined in contrast to dark matter and radiation, and refer to all ordinary matter composed of hadrons. This includes protons and neutrons, the light nuclei produced during Big Bang nucleosynthesis, as well as gas, dust, stars, etc.

additional theoretical and observational effort could profitably be devoted. Before discussing the condensed-matter aspects of the QCD-AQN framework, we first review the observational evidence that motivates the study of AQNs (Section 3). We then present a concise overview of the theoretical foundations of the QCD-AQN model (Section 4). This is followed by a very brief review of axion physics and a discussion of the possibility that DM consists of AQNs together with a subdominant component of QCD axions (Section 5). Finally, to complement this excursion into applications of QCD in cosmology, we outline a QCD-based approach to the dark-energy problem (Section **??**).

2 A critical perspective on model-independent constraints

Cosmology is currently at a turning point, with the community actively diversifying both theoretical and experimental strategies to address the dark matter problem Bertone and Tait (2018). This section reviews the set of model-independent observational constraints that any viable DM candidate must satisfy. It is important to distinguish between *direct* empirical constraints and conclusions that rely on additional theoretical assumptions about the nature of DM. As we shall see, some commonly stated "properties" of dark matter are not direct observations, but interpretations that depend on specific modelling choices.

2.1 Where is dark matter ?

Observations of galaxy rotation curves, galaxy velocity dispersions, hot intracluster gas, gravitational lensing, and anisotropies in the Cosmic Microwave Background (CMB) leave little doubt that dark matter exists and constitutes a substantial fraction of the Universe's total energy density.

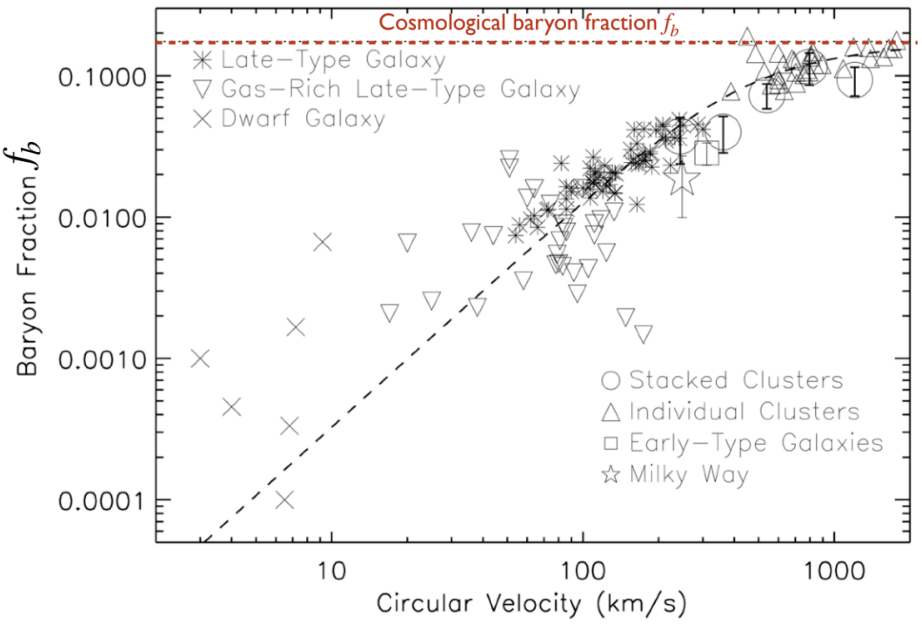


Figure 1: Fraction of baryon mass relative to total mass (circular velocity) in various systems and environments (from Dai et al. (2010)).

From the latest Planck results Planck Collaboration et al. (2020) the baryon density today is $\Omega_b h^2 \simeq 0.0224 \pm 0.0001$ and the DM density is $\Omega_c h^2 \simeq 0.120 \pm 0.001$. The cosmological baryon fraction is therefore given by

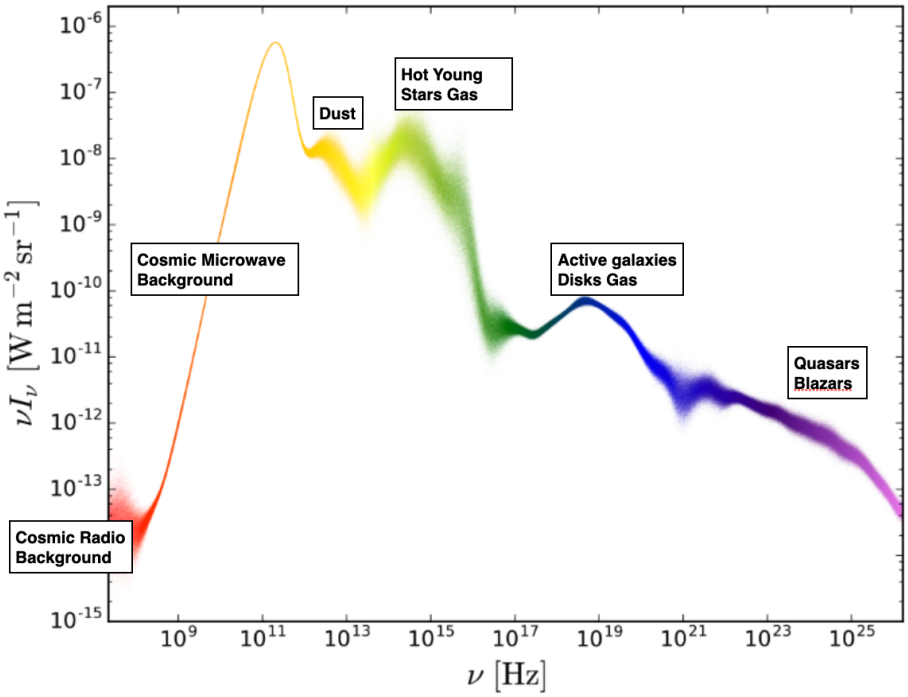


Figure 2: Intensity of the sky monopole as a function frequency Hill et al. (2018). The width of scattered points along the vertical direction indicate the measurement errors.

$$f_{b,\mathrm{cosmo}} \equiv \frac{\Omega_b}{\Omega_b + \Omega_c} \simeq 0.156 \tag{1}$$

Although DM is present throughout the Universe, its spatial distribution is highly biased towards lower mass systems. Fig. 1 shows the baryon fraction $f_b(V_c)$ as a function of circular velocity V_c, which serves as a proxy for the depth of the gravitational potential well. Observations indicate that dwarf galaxies are at least two orders of magnitude more DM dominated than massive galaxy clusters.

2.2 How dark is dark matter ?

The qualifier *dark* is understood to mean that DM does not emit electromagnetic radiation above the sensitivity thresholds of current instruments; it should not be conflated with *black*, which would imply the complete absence of any emission. Fig 2 show the measured sky intensity frequency spectrum, together with the dominant sources responsible for this emission Hill et al. (2018). The integrated emission from known sources over the whole sky is in good agreement with the measurement, which means that no significant excess has been seen relative to the expectations. One exception is the ARCADE excess at $\nu < 1\,\mathrm{GHz}$ which remains significant, even after all known galactic and extragalactic sources have been taken into account Fixsen et al. (2011).

In principle, DM could emit radiation at any frequency, provided that its intensity remains below the error bars. Interestingly, it is considerably easier for rare, macroscopic DM candidates to produce such an emission without violating observational constraints than for DM composed of elementary particles. The reason is that the very high number density of elementary-particle DM would lead to a substantial cumulative emission, which is not observed. By contrast, a rare population of massive DM objects could emit significantly on an individual basis, yet still produce a negligibly small total luminosity owing to their low number density.

Key takeaway. Dark matter is dark, yet this does not preclude the possibility that it emits a faint glow below current detection thresholds.

2.3 Cold dark matter

Dark matter is termed *cold* if its typical velocity $v_{\rm eq}$ at the epoch of matter–radiation equality ($z_{\rm eq} \sim 3400$) is much smaller than the speed of light c, such that its free-streaming length $\lambda_{\rm FS}$ remains below galactic scales[2]. $\lambda_{\rm FS}$ is defined as:

$$\lambda_{\rm FS} = \int_0^{t_0} \frac{v(t)}{a(t)} \mathrm{d}t = \int_0^{a_{\rm nr}} \frac{1}{a^2 H(a)} \mathrm{d}a + \int_{a_{\rm nr}}^{1} \frac{v(a)}{a^2 H(a)} \mathrm{d}a, \tag{2}$$

where $v(t)$ is the DM velocity and $a(t)$ is the cosmological scale factor. $a_{\rm nr}$ is the scale factor when DM becomes non-relativistic. Although the free-streaming integral formally depends on the epoch at which dark matter becomes non-relativistic, the classification into cold, warm, and hot dark matter is set by whether the relativistic–to–non-relativistic transition occurs well before the time of matter–radiation equality. If $a_{\rm nr} \ll a_{\rm eq}$, the relativistic contribution to free streaming is negligible and dark matter behaves as cold.

The existence of an observational upper bound on the free-streaming length is largely model independent: structure formation data imply that dark matter cannot erase density fluctuations on scales comparable to galaxies. However, the exact *calculation* of the free-streaming length $\lambda_{\rm FS}$ is model dependent, since it depends on the detailed velocity history of the DM particles. For example, consider a thermal relic of mass $m_{\rm DM}$. While it remains in thermal equilibrium, its typical momentum scales as $p \sim T$. The particle becomes non-relativistic when the temperature drops to $T \sim m_{\rm DM}$. In this case, there is a relatively direct relation between the particle mass and its velocity at matter–radiation equality, which can be translated into a lower bound on $m_{\rm DM}$. By contrast, if dark matter is produced through a non-thermal mechanism, its momentum distribution can be significantly different.

The key point is that free-streaming constraint limit the DM *velocity* at matter–radiation equality. It does not directly impose a universal bound on the particle mass, since the specifics of the production mechanism plays a decisive role in determining the velocity distribution. What observations constrain in a truly model-independent way is the relative transfer function with respect to CDM:

$$T(k) \equiv \frac{P(k)}{P_{\rm CDM}(k)},$$

where $P(k)$ is the three-dimensional power spectrum of a given model. $P_{\rm CDM}(k)$ is the Cold Dark matter (CDM) reference spectrum corresponding to a negligible free-streaming length ($\lambda_{\rm FS} \ll 1\,\mathrm{kpc}$).

The solid red line in Fig. 3 shows the CDM power spectrum fitted to multiple datasets. One can see that it retains significant power on very small scales, extending to $k \gg 10\,h\,\mathrm{Mpc}^{-1}$. Not shown on Fig. 3, is that hot DM models predict a strong suppression for $k \gtrsim 0.01$–$0.1\,h\,\mathrm{Mpc}^{-1}$, while warm DM leads to suppression at intermediate scales, typically $k \gtrsim 5$–$30\,h\,\mathrm{Mpc}^{-1}$, depending on the specific model parameters.

Observations of the CMB, represented by the yellow region in Fig. 2, probe $P(k)$ on large scales ($k \lesssim 0.2\,h\,\mathrm{Mpc}^{-1}$) and show no significant deviation from the CDM prediction, thereby excluding hot dark matter and strongly constraining warm dark matter scenarios in this regime. On sufficiently large scales, DM behaves effectively as cold and has already begun to cluster gravitationally by the epoch of recombination.

[2]The definition of a galactic scale is somewhat arbitrary, but it is generally accepted that a typical halo mass of a dwarf galaxy, $M \sim 10^8\,\mathrm{M}_\odot$, provides a reasonable reference value.

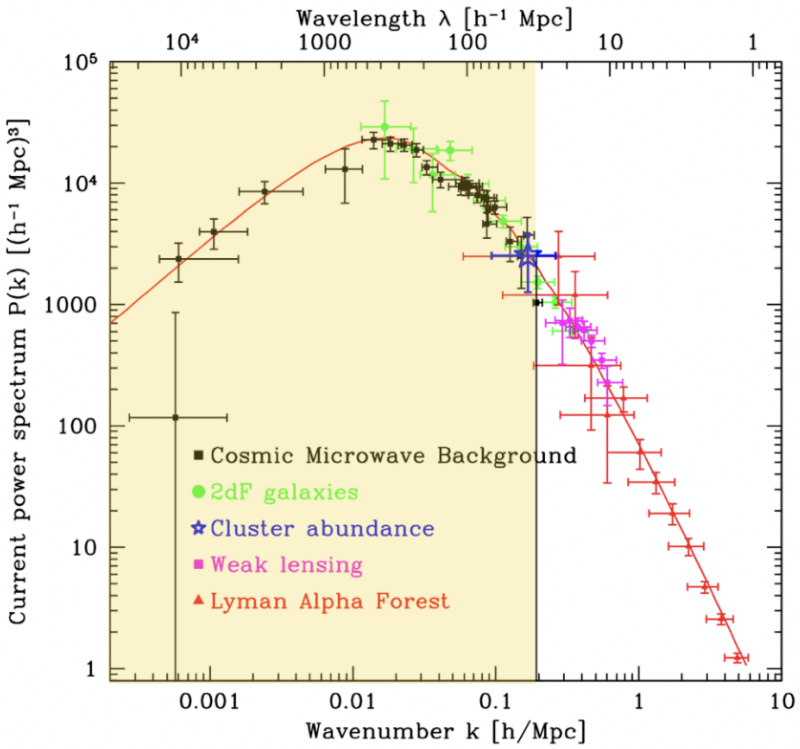


Figure 3: Power spectrum from a combination of observational probes, by Tegmark and Zaldarriaga (2002). The red line shows the CDM power spectrum fitted to the multiple datasets.

The Lyman-α forest provides access to intermediate scales, $k \sim 0.5$–$5\,h\,\mathrm{Mpc}^{-1}$. Galaxy redshift surveys and counts of dwarf galaxies probe substantially smaller scales, reaching $k \gtrsim 10\,h\,\mathrm{Mpc}^{-1}$. The absence of any suppression of power on these scales provides strong empirical support for the CDM paradigm and rules out hot DM.

Key takeaways. Cold dark matter is empiricially supported. Warm dark matter scenarios are now tightly constrained (e.g. Palanque-Delabrouille et al. (2020); Nadler et al. (2021)). Hot dark matter is incompatible with current data.

2.4 Collisionless dark matter

The interaction rate of DM is strongly constrained by observations. Consider DM-DM collisions. The mean free path is given by $\lambda = (\sigma n)^{-1}$, where n is the DM number density and σ the DM-DM cross-section. Dark matter is described as collisionless within a system of characteristic size L when its mean free path λ is much larger than L, i.e. $\lambda \gg L$. This can be rewritten as:

$$\left(\frac{\sigma}{m}\right)\rho L \ll 1,$$

where $\rho = n\,m$ is the DM mass density. Hence $\Sigma_{\mathrm{obs}} = \rho L$ is the surface mass density of the system. Observations indicate that $\Sigma_{\mathrm{obs}} \sim 0.05$–$0.3\,\mathrm{g\,cm}^{-2}$ across a broad range of systems, including galaxy clusters, groups, and individual galaxies.

At cluster and larger scales, observations show that (see Table 1):

$$\frac{\sigma}{m} \lesssim 1\,\mathrm{cm}^2\,\mathrm{g}^{-1},$$

which is $\ll \Sigma_{\mathrm{obs}}^{-1}$, indicating that dark matter is collisionless at these scales. This constraint is

Constraints	σ/m	Velocity	Observable / Method
Halo shapes / ellipticity	$\lesssim 1\,\mathrm{cm}^2\,\mathrm{g}^{-1}$	$1300\,\mathrm{km\,s}^{-1}$	Cluster lensing surveys
Substructure mergers	$\lesssim 2\,\mathrm{cm}^2\,\mathrm{g}^{-1}$	~ 500–$4000\,\mathrm{km\,s}^{-1}$	DM–galaxy offset
Merging clusters	$\lesssim$ few $\mathrm{cm}^2\,\mathrm{g}^{-1}$	2000–$4000\,\mathrm{km\,s}^{-1}$	Post–merger halo survival
Bullet Cluster	$\lesssim 0.7\,\mathrm{cm}^2\,\mathrm{g}^{-1}$	$4000\,\mathrm{km\,s}^{-1}$	Mass–to–light ratio

Table 1: Astrophysical constraints on the dark matter self–interaction cross-section per unit mass σ/m from cluster-scale observations. From Tulin and Yu (2018)

model-independent, as it follows directly from gravitational lensing measurements and basic dynamical arguments, without invoking assumptions about baryonic physics or halo modelling.

On smaller scales, such as dwarf galaxies, galaxy groups, and cluster cores, larger values are favoured:

$$\frac{\sigma}{m} \sim 1\text{–}10\,\mathrm{cm}^2\,\mathrm{g}^{-1},$$

and may even provide an attractive feature of self-interacting DM models Spergel and Steinhardt (2000). However, unlike the cluster-scale upper bound, such interpretation relies on a complete understanding of the complex astrophysical processes, such as stellar and active galactic nuclei feedback, gas stripping, gas outflows and gas cooling to name a few Pontzen and Governato (2012); Tulin and Yu (2018). No observations currently exclude collisionless DM at any scales.

Key takeaway. Although observational bounds on σ/m are model-independent in nature, their theoretical interpretation and calculation depend on the specific DM scenario under consideration.

2.5 Dark matter interactions with baryons and photons

Observational data impose limits on the strength of DM interactions with baryons and photons. If DM scatters with baryons then we can define the interaction rate $\Gamma_{\mathrm{DM-b}}$:

$$\Gamma_{\mathrm{X}-b} = \frac{\rho_b}{m_{\mathrm{X}}}\langle\sigma_{\mathrm{X}-b}\,v\rangle,$$

where $\langle\sigma_{\mathrm{X}-b}\,v\rangle$is the velocity dependent cross-section of the DM-baryon interaction. Momentum exchange between the two fluids will modify the acoustic oscillations in the primordial plasma. This will alter the heights and phases of the CMB acoustic peaks, suppress the growth of small-scale density perturbations, and consequently distort the CMB temperature and polarisation power spectra. Such deviations will accumulate prior to recombination. They will also affect the subsequent formation of structure, leaving observable imprints in large-scale structure probes such as the Lyman-α forest.

Since neither Planck CMB measurements nor redshift surveys detect such departures from the standard cosmological model, one obtains the robust requirement that $\Gamma_{X-b} \ll H$ around recombination, a condition which is independent of the DM model. However, the corresponding constraint on the cross-section per unit mass, σ_{X-b}/m_X, depends on the velocity dependence of the DM–baryon interaction, and more generally on the DM model under consideration. For different velocity scalings of the cross-section, the resulting bounds are given by Dvorkin et al. (2014); Gluscevic and Boddy (2018); Boddy and Gluscevic (2018); Boddy et al. (2018):

$$\frac{\sigma_{X-b}}{m_X} \lesssim 10^{-9} - 10^{-6}\,\mathrm{cm}^2\mathrm{g}^{-1}$$

The interaction between DM and photons would lead to similar effects. The absence of such signature also leads to an upper bound for the DM-photon cross-section Wilkinson et al. (2014); Stadler and Bœhm (2018):

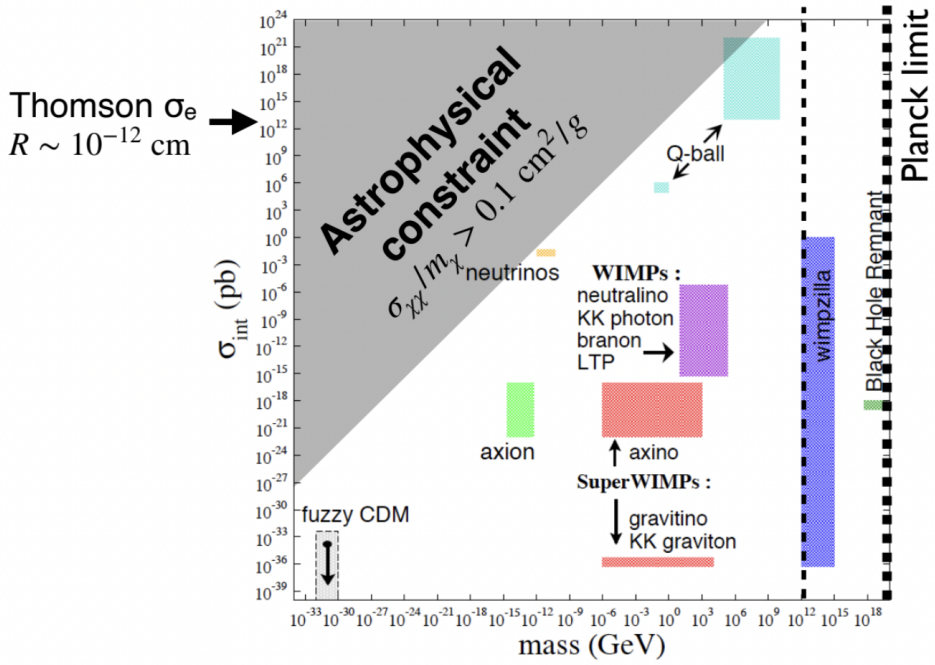


Figure 4: Limits on the annihilation cross-section of DM as a function of DM mass Baer (2009). The top-left gray region is excluded because DM must be collisionless.

$$\frac{\sigma_{X-\gamma}}{m_X} \lesssim 10^{-6} - 10^{-4}\,\mathrm{cm^2 g^{-1}}$$

These are robust bounds on DM–baryon and DM–photon scattering, obtained from the requirement that dark matter must have decoupled from the primordial plasma before recombination. However, unlike the cluster-scale self-interaction limit, these constraints stem from early-Universe drag effects, and their translation into limits on the cross-section depends on the specific DM model. By contrast, the optical-depth constraint on DM–DM interactions is largely geometric in nature and therefore model independent.

By comparison, for WIMPs the self-interaction cross-section cannot be inferred directly from observations and must instead be estimated within a specific particle-physics framework. In the minimal weak-scale scenario, i.e. point-like WIMPs without a light mediator[3], one typically obtains $\sigma_{XX}/m_X \sim 10^{-17} - 10^{-13}$ cm^2 g^{-1}. Direct-detection experiments constrain the WIMP–nucleon interaction cross-section to approximately $\sigma_{Xb}/m_X \sim 10^{-26} - 10^{-24}$ cm^2 g^{-1} for weak-scale masses (see for example Aalbers et al. (2023)). Finally, still for minimal WIMP models, the particle does not couple to photons at tree level, so the WIMP–photon cross-section is expected to be extremely small (i.e. suppressed at the loop level). These estimates demonstrate that more than ten orders of magnitude in parameter space separate the canonical WIMP expectation for self-interactions from the current astrophysical upper limits. A substantial region of the parameter space remains largely unexplored: This wide open regime is illustrated in Fig. 4, which displays only the self-interaction cross-section.

Key takeaway. A substantial region of the σ–mass parameter space for DM candidates remains largely unexplored.

[3]This model is closely aligned with the historical WIMP paradigm

2.6 Observational constrains from Big Bang Nucleosynthesis

Big Bang Nucleosynthesis (BBN) provides a powerful model-independent probe of DM, as it occurs during a particularly well-controlled epoch in cosmic history ($t \sim 1\text{–}10^3$ s, $T \sim 0.1\text{–}10$ MeV), during which both the expansion rate of the Universe and energy injection processes are tightly restricted by observations. The constraints come from the primordial abundances of light elements (D, ^{3}He, ^{4}He, and ^{7}Li): an additional energy injection from DM and/or an increase of relativistic species $\Delta N_{\rm eff}$ (e.g. sterile neutrino as DM) at this epoch, would leave an imprint on the light elements abundances. Energy injection will generally photodissociate light elements, over producing deuterium and ^{3}He and decrease ^{4}He. If DM produces hadrons instead, e.g. from decay or annihilation, the n/p ratio will differ, which can subsequently modify the abundance of certain light elements. Letting the ^{7}Li problem asside, the current constraints on D/H and ^{4}He$/H$, combined with CMB, set a strong upper bound on $\Delta N_{\rm eff} \lesssim 0.2-0.3$ Fields et al. (2020); Pitrou et al. (2018).

Let's emphasise that the baryon–to–photon ratio,

$$\eta \equiv n_b/n_\gamma \simeq 6.1 \times 10^{-10} \tag{3}$$

is determined independently by BBN and by the CMB. The agreement between these two measurements – spanning the period from ~ 3 min after the Big Bang to about 380,000 years later – provides one of the most compelling consistency tests of the standard cosmological model. Since η fixes the baryon density, one infers that:

$$\Omega_{\rm DM} \sim 5\Omega_b. \tag{4}$$

This fact is often invoked as evidence that dark matter must be non-baryonic, since a dominant baryonic-DM component would have significantly altered the primordial light-element abundances. However, it is important to clarify what BBN really implies. BBN does not rule out baryonic dark matter in a model-independent way; rather, it constrains the abundance of baryons that were thermally coupled and participated in nucleosynthesis at the MeV epoch. In other words, DM must not have been overwhelmingly coupled to the baryon–photon plasma during BBN.

If dark matter consists of elementary particles interacting with baryons, the simplest way to satisfy this requirement is indeed for it to be non-baryonic. However, another possibility is that DM is composed of rare, compact, stable *macros*: even if such objects were of baryonic origin, their rarity would prevent them from significantly modifying primordial nucleosynthesis.

Key takeaways. The observed light-element abundances impose stringent constraints: DM must be cold, non-relativistic, and non-disruptive at MeV temperatures Cyburt et al. (2016). Dark matter must interact only weakly with ordinary matter. This requirement may be satisfied either by abundant non-baryonic particles with very small interaction cross-sections, or by massive but extremely rare objects. BBN does not exclude dark-matter candidates composed of quark matter.

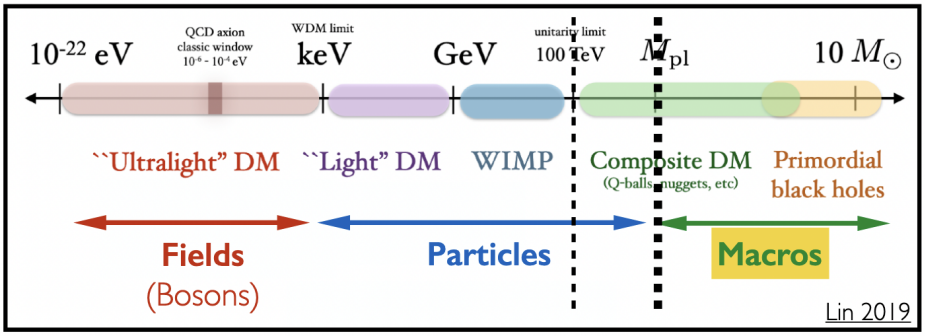
2.7 An overlooked hypothesis: rare dark matter

An observational upper bound on the ratio σ/m_X does not, by itself, place independent constraints on the interaction cross-section σ or on the number density n_X separately. Let us rewrite the upper bound constraints in terms of n_X. For the self-interaction rate in a halo:

$$\sigma_{XX} n_X L_{\rm halo} \ll 1.$$

For DM-baryon, we obtain:

$$\sigma_{X-b} n_X (v_{\rm rel}/H) \ll 1,$$



"Interacting weakly" ⟶ "interactions are rare"

Figure 5: Mass range for various DM candidates. The thicker dashed line indicates the Planck mass. AQNs belong to the composite DM region, with $m_{\rm AQN} \sim 10^{20}$–10^{23} TeV. From Lin (2019).

and for DM-photon:

$$\sigma_{X-\gamma} n_X (v_{\rm rel}/H) \ll 1.$$

One can see that the same upper bound can be realised either with a small cross-section and a large number density n_X, or with a large cross-section and a small n_X.

It is common to hypothesize that DM is composed of abundant subatomic particles. In the Solar System environment, where the DM mass density is $\rho_x \simeq 0.3\,{\rm GeV\,cm^{-3}}$, their number density is extremely large, $n_X \simeq 3 \times 10^5 ({\rm GeV/m_X})\, m^{-3}$. Given the current absence of direct detection of subatomic DM, such particles must interact only very weakly with baryons, hence their very small cross-sections $\sigma_{XX}, \sigma_{X-b}$ and $\sigma_{X-\gamma}$.

An alternative possibility is that DM consists of macroscopic objects with mass $m_X \gg M_{\rm Planck}$, characterised by extremely low number densities $n_X \ll 10^{-14}\,{\rm m^{-3}}$. In this case, even large values of $\sigma_{XX}, \sigma_{X-b}$ and $\sigma_{X-\gamma}$ can produce a low total emission rate to have so far evaded detection. Moreover, for $n_X \ll 1\,{\rm m^{-3}}$, direct detection on Earth would be unlikely.

Key takeaway. Massive, rare DM particles with a large interaction cross-section are not ruled out by observations.

2.8 Bayesian perspectives on dark-matter models

Astrophysical measurements establish that a dark, cold, and collisionless matter component exists, but no observation to date demonstrates that dark matter is composed of elementary particles. We are left with two hypotheses: Either DM is composed of abundant, weakly interacting particles or it is made of rare, strongly interacting macroscopic objects. The latter has received comparatively little attention and remains the largest unexplored region of parameter space among DM models Jacobs et al. (2015). Fig. 5 illustrates the wide range of viable DM mass scales. With these conclusions in mind, we now proceed to examine the Bayesian evidence associated with the leading DM candidates.

Alternative dark matter models refer to theoretical proposals beyond the Weakly Interacting Massive Particle (WIMP) scenario. Examples include axions, sterile neutrinos, primordial black holes (PBHs), self-interacting DM (SIDM) and macroscopic composite objects such as AQNs. Each of these models makes different assumptions about the mass, interactions, and cosmological behaviour of dark matter. Given the variety of DM models and the size of the parameter space, a quantitative comparison based on Bayesian inference provides a systematic framework for assessing their relative plausibility.

A common concept in evaluating these models is falsifiability: does the model make clear predictions that could, in principle, be proven wrong? For example, WIMPs predict signals in underground direct detection experiments, axions predict narrow-band signals in resonant cavity experiments. These are examples of observational tests, where theory is confronted with independent measurements. In a Bayesian framework, we do not ask if a model is falsifiable, rather we consider the **posterior probability** $P(M|D)$ that model M is correct after taking the data D into account:

$$P(M|D) \propto P(D|M)P(M)$$

where $P(D|M)$ is the **likelihood**, which quantifies how well the model explains the data. $P(M)$ is the **prior probability**, i.e. the degree of plausibility assigned to the model before considering the current data. It encodes theoretical motivation, simplicity, and previous knowledge.

Now consider that model M has a parameter space θ, then by marginalizing over the parameter space, the Bayesian evidence can be written as:

$$P(D|M) = \int_{\text{Priors}} P(D|\theta, M)P(\theta|M)\mathrm{d}\theta$$

One can see that for models in which only a small fraction of the parameter space θ yields a high likelihood, while most of the space gives a poor likelihood, the Bayesian evidence $P(D|M)$ is small. This is known as the Occam penalty. It arises when a model has a large parameter space, but only a small region of that space produces predictions consistent with the data. In such cases, most of the prior volume contributes little to the likelihood, which reduces the overall Bayesian evidence. Importantly, this penalty is not imposed by hand; it appears automatically when the likelihood is marginalised over the full parameter space.

To illustrate these definitions, let us consider the example of WIMPs:

- With the original WIMPs miracle, the prior $P(M_{\text{WIMPs}})$ was high for several reasons: WIMPs were naturally linked to the electroweak scale; the thermal freeze-out explained $\Omega_{\text{DM}} \sim \Omega_b$; the model had very few parameters and appeared natural. Its Occam penalty was low.
- The null results from direct, indirect, and collider searches progressively reduced the likelihood $P(D|M_{\text{WIMPs}})$, since an increasing fraction of the parameter space became incompatible with the data;
- The absence of supersymmetry at the LHC, together with the lack of evidence for new weak-scale physics, has led to a substantial reduction of the prior plausibility $P(M_{\text{WIMPs}})$.

As a result, the posterior $P(M_{\text{WIMPs}}|D)$ has significantly reduced over the last twenty years.

In contrast, many DM alternatives (see Table. 2) are characterized by broad prior parameter spaces and have limited, often single-channel, phenomenological predictions. These models distribute likelihood over a wide range of possible datasets and incur only a mild Occam penalty, even as observational constraints accumulate. In other words, *the field now tolerates less predictive models, broader parameter spaces, and weaker experimental commitments.*

What about QCD-AQN ?

The QCD–AQN framework is rooted in QCD-scale physics and axion dynamics. It belongs to a well-motivated Standard Model extension, the QCD axion. Its extensive explanatory scope will be explained in Section 4. Sociogically, such a broad scope elicits scepticism within the scientific community, not because Bayesian reasoning penalises it, but because of historical factors. Past experience has fostered a culture of caution. Unified frameworks that claim to explain many seemingly unrelated phenomena can appear too ambitious. Scientists tend to apply an *informal epistemic prior*: the broader the claim, the more rigorous the required evidence.

QCD-AQN carries a historical burden stemming from an earlier proposal. In 1984, Edward Witten Witten (1984) introduced the idea that stable lumps of strange quark matter could have

formed during a first-order QCD transition, carry a large baryon number and behave as DM: the so-called *quark nuggets*. However, later lattice QCD studies indicated that, at zero baryon chemical potential, the cosmological QCD transition is a smooth crossover Karsch (2002) rather than a strong first-order phase transition, thereby weakening Witten's nuggets formation mechanism. The QCD-AQN scenario, which introduces new ingredients to provide a radically different formation pathway (see Section 4), has sometimes mistakenly been viewed through the lens of Witten's quark nuggets fall out.

QCD-AQN makes unavoidable, multi-channel predictions arising from the coupling of AQNs with a large variety of baryonic environments, which results in a heavy Occam penalty. These astrophysical environments span several fields of study: cosmology, high-energy astrophysics, stellar physics, interstellar medium, planetary science etc. Modern research is highly specialised, with distinct subfields operating semi-independently. From a sociological perspective, a model that connects disparate domains challenges disciplinary boundaries and may face resistance simply for crossing them. There is concern that wide explanatory scope might conceal hidden fine-tuning or selective interpretation of data, thereby requiring stronger empirical support to achieve comparable evidence.

On the positive side, QCD-AQN is governed by a single fundamental parameter, the mean AQN mass, $\langle m_{AQN} \rangle$, which is restricted to a relatively narrow window by independent observational and theoretical considerations (see Section 3.5.5).

Key takeaways. QCD-AQN is high-risk but potentially high-reward framework. It is neither easily excluded nor easily accommodated. Its ultimate viability hinges on the emergence of distinctive, environment-specific signatures that cannot be replicated by more weakly predictive DM scenarios.

3 Confronting QCD-AQN to observations

Having reviewed the observational constraints that any viable dark matter model must satisfy, we now turn to the observational aspects of the QCD-AQN framework, which constitute the principal motivation for its investigation. In this scenario, when the QCD transition begins, at $T \sim 170\,\mathrm{MeV}$, the pre-existing small asymmetric coupling between quarks (antiquarks) to the axion field, combined with the collapsing of the axion domain walls, leads to the formation of aggregates with large baryon numbers ($|B| \gtrsim 10^{24}$), the so called Axion Quark Nuggets (AQNs). The formation of AQNs, the baryon-charge separation process and the AQNs survival in the early Universe will be discussed in Section 4. For the purpose of observational tests, it is sufficient to focus on the structure of the aggregates. In this section, after reviewing their fundamental properties, we explore a range of potential AQN signatures, considering first their behaviour in dilute media and then in dense environments.

3.1 AQNs structure and properties

Matter (antimatter) AQNs are macroscopic aggregates of quarks (antiquarks) in a Colour-Superconducting (CS) phase, stabilised by an axion domain wall that acts as a confining shell. The quark (antiquark) core is surrounded by an electron (positron) cloud that ensures overall electric neutrality (Fig. 6).

Convention: Throughout the remainder of this lecture, $\mathrm{A\overline{Q}N}$ *will denote antimatter aggregates and* $\mathrm{A\underline{Q}N}$ *will denote matter aggregates.*

Candidate	Prior theoretical motivation	Explanatory scope beyond DM	Main penalties / tensions
QCD axions	Very high: solves the strong CP problem within a well-motivated Standard Model extension; no dark sector	High: DM + resolution of the strong CP problem	No confirmed detection; broad but narrowing parameter space
QCD-AQNs	Moderate–high: QCD and axion physics with additional dynamical assumptions; no dark sector	Very high: matter-antimatter asymmetry; natural link $\Omega_{\rm DM} \sim \Omega_b$, baryon-to-photon ratio η, possible lithium-7 tension, possibility of avoiding baryogenesis; potential multi-messenger signatures	No decisive detection; historical scepticism from earlier nugget models; structural complexity
WIMPs	Historically very high ("WIMP miracle"); electroweak-scale new physics	Moderate: primarily relic abundance via thermal freeze-out	Strong null results from direct detection, indirect searches, and LHC; shrinking parameter space
ALPs	Moderate: generic prediction of string compactifications and hidden sectors	Moderate: DM candidate; possible astrophysical transparency anomalies	Highly flexible parameter space; reduced predictivity; no confirmed detection
Sterile neutrinos	Moderate: minimal extension of the neutrino sector; motivated by neutrino mass generation	Moderate: DM + possible links to neutrino physics	X-ray constraints; structure formation limits; uncertainties in production mechanisms
Primordial Black Holes (PBH)	Moderate: no new particle physics required; arises from early-universe collapse	Moderate: DM; possible connection to gravitational-wave events	Strong constraints across many mass ranges (microlensing, CMB, evaporation, dynamics)
Self-Interacting DM (SIDM)	Moderate: phenomenological extension of CDM addressing small-scale tensions	Moderate–high: DM + potential resolution of core–cusp and diversity problems	Requires tuned interaction cross sections; not a unique underlying particle model

Table 2: Qualitative comparison of major dark matter candidates, highlighting theoretical motivation, explanatory scope, and principal tensions.

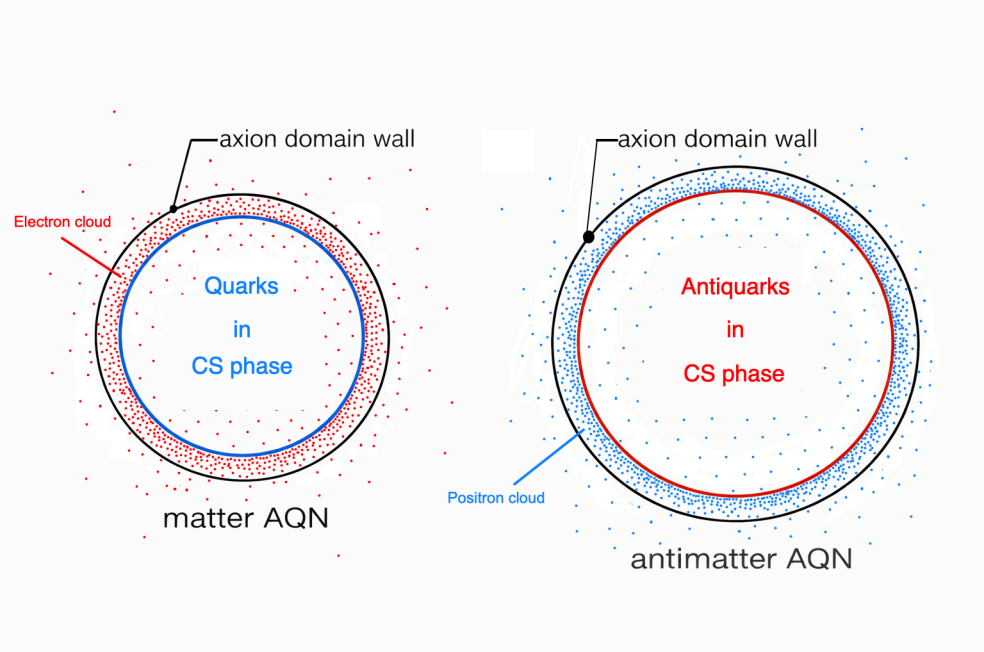


Figure 6: The quarks (antiquarks) in an AQN core are bound by an axion domain wall and stabilised by a superconducting energy gap, $\Delta_{\rm gap} \sim 100\,{\rm MeV}$. Matter A$\underline{\rm Q}$Ns are surrounded by an electron cloud. Antimatter A$\overline{\rm Q}$Ns are composed of an antiquark core surrounded by a positron cloud. The cosmological distribution of matter and antimatter AQNs is asymmetric (see 4.2).

.

The baryon number of AQNs is not a freely adjustable parameter but emerges from QCD dynamics at the axion domain-wall formation epoch; theoretical estimates based on the balance between domain-wall tension, Fermi pressure, and colour-superconducting energy gaps lead to typical values in the range $|B| \sim 10^{22}$–10^{28} (see 4.6), corresponding to macroscopic masses $\sim 10^{-2}$ – 10^{4} grams.

Matter A$\underline{\rm Q}$Ns do not produce observable annihilation signatures: Because of the low abundance of antimatter cosmic rays, quark aggregates remain dark. Their interactions can be studied mainly through their gravitational effects as a CDM component. They are not the primary focus of this lecture.

Of particular interest is the population of antimatter A$\overline{\rm Q}$Ns which collide with ambient baryons, thereby generating observable signatures across a broad range of wavelengths and astrophysical environments.

The dense CS core of the A$\overline{\rm Q}$N generates an electric field that binds positrons in an extended structure outside the sharp surface. This positron cloud, also know as positron electrosphere, behaves like a Thomas-Fermi gas Thomas (1927); Fermi (1928) and has a stratified profileForbes et al. (2010):

- degenerate inside the antiquark core;
- distributed as a thin classical relativistic gas layer at the core surface;
- non-relativistic Boltzmann gas above the surface .

3.2 Cosmological behaviour of AQNs: cold and collisionless

Because the QCD-AQN framework lies at the intersection of cosmology and condensed matter physics, differences in terminology can obscure the discussion. It is therefore useful to clarify what is meant by baryonic matter.

From a particle physics perspective, AQNs are baryons because they are made of quarks bound

Physical quantity	Characteristic value
Geometric cross section	$\sigma/M \sim 10^{-10}\ \mathrm{cm}^2\,\mathrm{g}^{-1}$
Radius	$R \sim 10^{-5}$ cm
Mass	$m \gtrsim 10^{24}\, m_p \sim 1$ g
Density	$\rho \gtrsim \rho_{\mathrm{nucl}} = 3.5 \times 10^{14}\mathrm{g.cm}^{-3}$
Number density (Earth environment)	$(10^6\,\mathrm{km})^{-3} \lesssim n_{\mathrm{AQN}} \lesssim (10^3\,\mathrm{km})^{-3}$

Table 3: Main physical characteristics of AQNs.

into dense quark matter and therefore $B \neq 0$. Their mass originates from QCD-scale strong interactions, just like ordinary protons and neutrons.

In cosmology, baryonic matter is defined by its role in early-Universe rather than by its quark content. Here, a baryon refers to ordinary matter that carries baryon number and participates in the thermal and nuclear processes of the early Universe, i.e. the matter component that was tightly coupled to photons before recombination. In this context, AQNs are not baryons because their baryon number is confined within compact objects before BBN, preventing them from participating in primordial element formation or in the photon–baryon plasma that shapes the CMB acoustic peaks.

In short, AQNs are baryonic in their microscopic composition yet non-baryonic in their cosmological behaviour.

AQNs are non-relativistic very early on. Being macroscopic objects with gram-scale masses, their thermal velocities after formation at the QCD transition are negligible compared to the speed of light. As the Universe expands, their velocities redshift further, so they behave as non-relativistic matter well before matter–radiation equality. This gives them an equation of state

$$w \equiv \frac{P}{\rho} \approx 0,$$

just like standard cold DM.

AQNs are collisionless on large scales. Although annihilation events happen when an $\mathrm{A\overline{Q}N}$ collides with baryons, their geometric cross section per unit mass is extremely small. In the dilute intergalactic medium, interaction rates are negligible compared to the Hubble expansion rate. Finally, the free-streaming length of AQNs is negligible, as these objects move with very small, non-relativistic velocities. They cluster gravitationally and seed structure formation as expected for cold DM.

Key takeaways. Despite being baryonic in composition, AQNs behave cosmologically as non-baryonic cold, collisionless DM. They are massive, slow-moving, and dynamically decoupled objects.

Having reviewed the large-scale cosmological behaviour of AQNs, we now focus on the thermal emission produced locally as they pass through baryon-rich environments.

3.3 Radiative signatures of $\mathrm{A\overline{Q}N}$s in dilute environments

In this section, we will discuss the electromagnetic radiation arising from the interaction of $\mathrm{A\overline{Q}N}$s with ordinary baryons in a dilute medium, which was first described by Forbes et al. (2010). Dense media will be discussed in 3.5 and prospects for future tests in various astrophysical environments are detailed in 3.6 and 3.7.

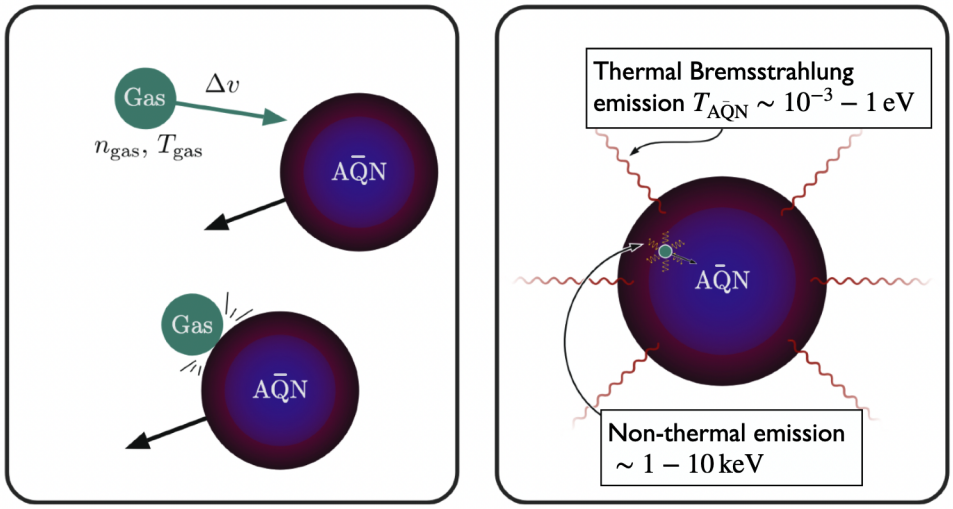


Figure 7: Left: A baryon (i.e. proton) collides with an AQ̄N [not to scale]. Right: The matter-antimatter annihilation emits ~ 2 GeV of energy in the form of thermal Bremsstrahlung and a secondary beam in the 1-10 keV range Sommer et al. (2024) .

The collision of an AQ̄N with a proton might lead to an annihilation releasing $\sim 2\,{\rm GeV}$ in the system (see Fig. 7). A fraction of this energy is promptly emitted as X-ray at the point of impact. A dominant fraction is deposited in the positron cloud and subsequently radiated away as a thermal Bremsstrahlung emission. A negligible fraction, which is ignored, is emitted in the form of axions, neutrinos and other subatomic particles. Fig. 8 summarises the structure and emission sources of an AQ̄N.

3.3.1 AQ̄N-baryon capture cross-section in dilute media

The AQ̄N temperature $T_{\rm A\bar{Q}N}$ is defined as the thermal temperature of the positron cloud. In the absence of AQ̄N-baryon collision:

- no energy is injected in the system and $T_{\rm A\bar{Q}N} = 0$;
- the positron gas in the AQ̄N core is fully degenerate;
- no radiation is emitted;
- the AQ̄N is electrically neutral: $Q = 0$.

In a dilute medium, when a baryon collides with an AQ̄N, the capture cross-section depends on the ionisation state of the gas.

- **Geometrical cross-section in a predomintaly neutral medium**

When ordinary matter collides with an AQ̄N, annihilation deposits energy into the AQ̄N core. A fraction of this energy is thermalised, increasing the core temperature and heating the surrounding positron cloud.

Two effects follow. First, the hotter positron cloud emits optically thin bremsstrahlung radiation. Second, a fraction of the least tightly bound positrons in the Boltzmann layer can escape the system. As a result, the AQ̄N acquires a net electric charge $Q < 0$, whose value depends on $T_{\rm A\bar{Q}N}$.

If the medium is predominantly neutral, the AQ̄Ns electric field has no effect on the capture rate of baryons and the effective capture cross-section is not significantly enhanced. As a result,

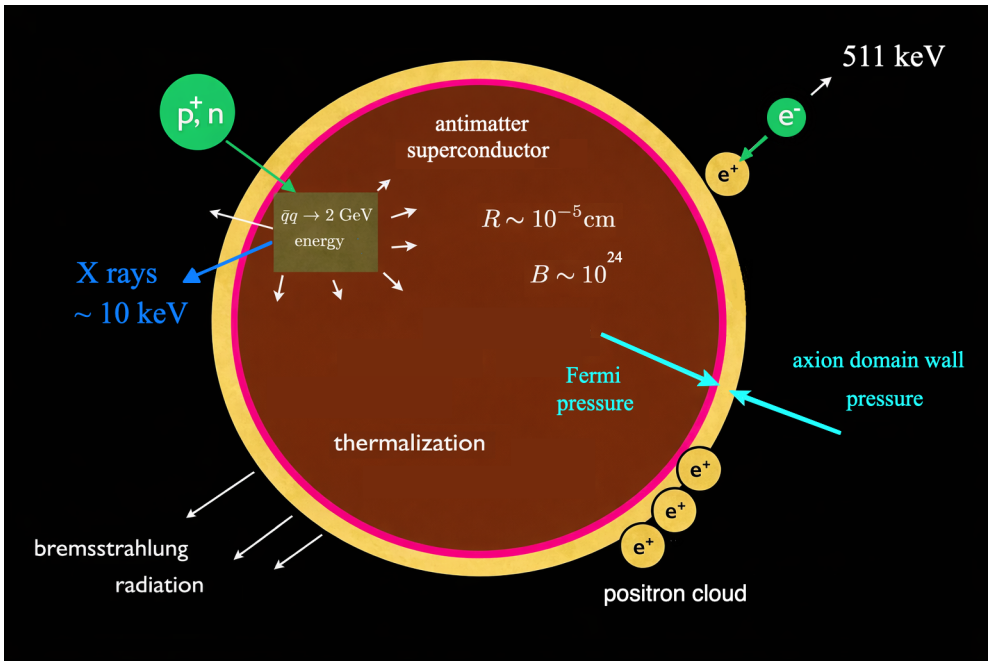


Figure 8: Summary of the structure and emission sources of an A$\overline{\text{Q}}$N. From Lawson and Zhitnitsky (2013b).

although the A$\overline{\text{Q}}$N heats and becomes mildly charged, its interaction rate remains controlled by the geometrical cross-section

$$\sigma_{\text{geo}} = \pi R^2_{\text{A}\overline{\text{Q}}\text{N}}. \tag{5}$$

- **Effective capture cross-section in an ionised medium**

If the medium is ionised, the charged A$\overline{\text{Q}}$N exerts a Coulomb force that attracts and captures additional baryons. These subsequently annihilate, depositing energy into the A$\overline{\text{Q}}$N core and heating the system further.

This enhanced heating increases the radiative output and drives the charge Q to more negative values. A thermal equilibrium is eventually established, determined by the balance between the cooling timescale, the collision rate, the effective impact parameter, and the annihilation timescale of captured baryons. Upon reaching thermal equilibrium, the effective cross-section of the charged A$\overline{\text{Q}}$N depends on several factors related to the astrophysical environment, such as the ionization level, the gas temperature and the density of the medium. We therefore define an effective cross-section:

$$\sigma_{\text{eff}} = \sigma_{\text{geo}} \left(\frac{R_{\text{eff}}}{R_{\text{A}\overline{\text{Q}}\text{N}}} \right)^2, \tag{6}$$

where R_{eff} is the effective radius of the effective capture volume.

3.3.2 A$\overline{\text{Q}}$N**s emission in a predominatly neutral, dilute medium**

In the derivation that follows, we consider an A$\overline{\text{Q}}$N evolving in a dilute medium such that its equilibrium temperature satisfies $T_{\text{A}\overline{\text{Q}}\text{N}} \lesssim 1\,\text{eV}$. At such temperatures, the interaction cross-section is

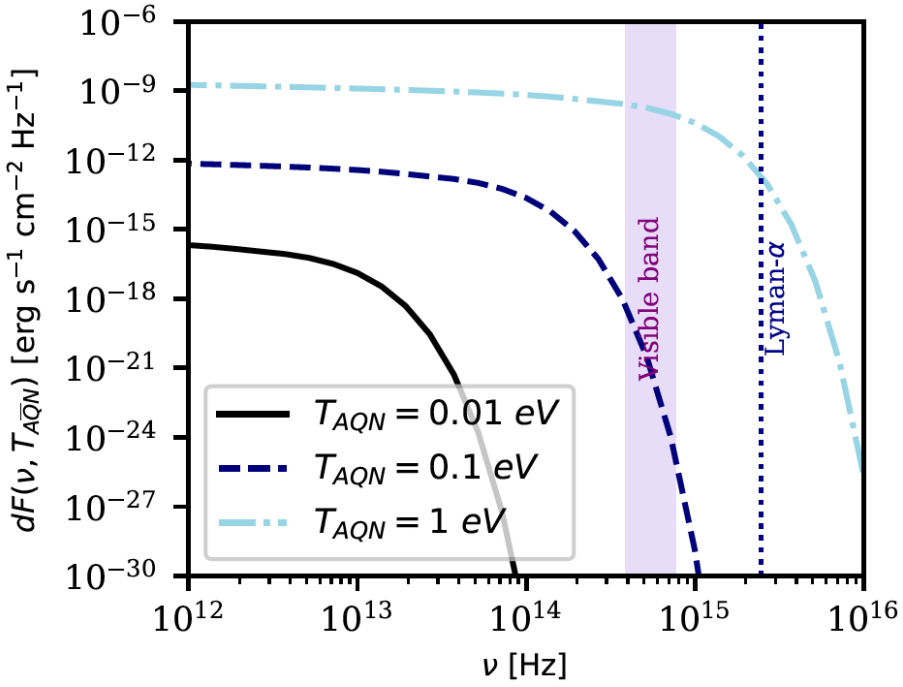


Figure 9: A$\overline{\text{Q}}$N thermal emission spectrum for various temperatures of the aggregates. The purple vertical band indicates the visible spectrum range and the Lyman-α line corresponds to 10.2 eV.

effectively equal to the geometrical cross-section, as long-range Coulomb effects associated with the A$\overline{\text{Q}}$N's electric charge can be neglected.[4]

At thermal equilibrium, the thermal emission spectrum (in erg s^{-1} cm^{-2} Hz^{-1}) of an A$\overline{\text{Q}}$N at temperature $T_{\text{A}\overline{\text{Q}}\text{N}}$ and frequency ν is given by:

$$dF(\nu, T_{\text{A}\overline{\text{Q}}\text{N}}) = \frac{8\pi}{45} \frac{T^3_{\text{A}\overline{\text{Q}}\text{N}}\, \alpha^{5/2}}{\pi} \left(\frac{T_{\text{A}\overline{\text{Q}}\text{N}}}{m_e}\right)^{1/4} \left(1 + \frac{2\pi\nu}{T_{\text{A}\overline{\text{Q}}\text{N}}}\right) h\left(\frac{2\pi\nu}{T_{\text{A}\overline{\text{Q}}\text{N}}}\right) \exp\left(-\frac{2\pi\nu}{T_{\text{A}\overline{\text{Q}}\text{N}}}\right) d\nu,$$

where α is the fine structure constant, m_e the electron mass and $h(x)$ is a slowly varying "Coulomb-log" type factor which results from the exact QED Bremsstrahlung calculation of the positron cloud. It is given by:

$$h(x) = \begin{cases} 17 - 12\ln\left(\frac{x}{2}\right), & x < 1, \\ 17 + 12\ln 2, & x \geq 1. \end{cases}$$

Fig. 9 shows the thermal emission spectrum $dF(\nu, T_{\text{A}\overline{\text{Q}}\text{N}})$ for several values of $T_{\text{A}\overline{\text{Q}}\text{N}}$. One notices a sharp emission drop around the visible band, which motives searches for a DM glow in the radio-visible range (see 3.7).

The total bolometric flux (in erg s^{-1} cm^{-2}) emitted by an A$\overline{\text{Q}}$N is obtained by integrating over frequency,

$$F_{\text{bol}}(T_{\text{A}\overline{\text{Q}}\text{N}}) = \int dF(\nu, T_{\text{A}\overline{\text{Q}}\text{N}}). \tag{7}$$

[4]Owing to its large mass, a charged AQN experiences negligible deflection in astrophysical magnetic fields. Its Larmor radius is typically of order tens of megaparsecs. This estimate remains valid even in extreme scenarios where the charge reaches $|Q| \sim 10^8 - 10^9\, e$. Consequently, AQNs cannot be detected through synchrotron radiation.

For simplicity, we now consider the collision with protons only (the generalisation to a more complex environment is straightforward). For each collision between an A$\overline{\text{Q}}$N and a proton, the total energy transferred as heat to the positron cloud is:

$$dE_{\rm ann} = (2\ \text{GeV})\, f\ (1-g),$$

where $f \sim 0.1$ is the quantum reflexion factor which accounts for the fact that only 10% of the colliding protons will be annihilated while the others will bounce back. The factor $(1-g)$ represents the fraction of the annihilation energy that is thermalised within the A$\overline{\text{Q}}$N, while the remaining fraction, g, is emitted as X-rays from the point of impact. $2\,\text{GeV} \simeq 2m_p$ is the energy available for annihilation, if successful.

Over a time interval $\mathrm{d}t$, the A$\overline{\text{Q}}$N will collide with a number of protons $\mathrm{d}N_p = \pi R^2_{\text{A}\overline{\text{Q}}\text{N}}\, n_b\, \Delta \mathrm{v}\, \mathrm{d}t$, where n_b is the number density of protons and Δv is the average relative speed between the A$\overline{\text{Q}}$N and the protons. The total power (in erg s^{-1}) injected into the A$\overline{\text{Q}}$N is therefore

$$\frac{\mathrm{d}E_{\rm ann}}{\mathrm{d}t} = (2\ \text{GeV})\, f\ (1-g)\, \pi R^2_{\text{A}\overline{\text{Q}}\text{N}}\, \Delta \mathrm{v}\, n_{\rm bar} \tag{8}$$

The equilibrium temperature $T_{\text{A}\overline{\text{Q}}\text{N}}$ is determined by equating Eq.(8) with Eq.(7):

$$\frac{\mathrm{d}E_{\rm ann}}{\mathrm{d}t} = 4\pi R^2_{\text{A}\overline{\text{Q}}\text{N}}\, F_{\rm bol}(T_{\text{A}\overline{\text{Q}}\text{N}}). \tag{9}$$

Consider a unit volume in which A$\overline{\text{Q}}$Ns are characterised by a number density $n_{\text{A}\overline{\text{Q}}\text{N}}$ and a temperature $T_{\text{A}\overline{\text{Q}}\text{N}}$. The resulting spectral emissivity, $d\varepsilon(\nu, T_{\text{A}\overline{\text{Q}}\text{N}})$, in units of erg s^{-1} Hz^{-1} cm^{-3}, is given by:

$$\mathrm{d}\epsilon(\nu, T_{\text{A}\overline{\text{Q}}\text{N}}) = 4\pi R^2_{\text{A}\overline{\text{Q}}\text{N}}\, \mathrm{d}F(\nu, T_{\text{A}\overline{\text{Q}}\text{N}})\, n_{\text{A}\overline{\text{Q}}\text{N}}$$

where $T_{\text{A}\overline{\text{Q}}\text{N}}$ is determined by the thermal equilibrium condition Eq.(9):

$$\boxed{T_{\text{A}\overline{\text{Q}}\text{N}} = \left[\frac{3\pi}{4}\,\frac{2\,\text{GeV}}{16\,\alpha^{5/2}}\, f\,(1-g)\, m_e^{1/4}\, \Delta \mathrm{v}\, n_b\right]^{4/17}} \tag{10}$$

Since the aggregate temperature depends on the local baryon density n_b, the emissivity scales as:

$$\mathrm{d}\epsilon(\nu, T_{\text{A}\overline{\text{Q}}\text{N}}) \propto n_{\text{A}\overline{\text{Q}}\text{N}}\, n_{\rm b}^{13/17} \tag{11}$$

Key takeaway. An emissivity scaling with both $n_{\text{A}\overline{\text{Q}}\text{N}}$ and n_b is unique to the QCD-AQN framework. Standard DM models do not predict emission that correlates with baryons. Decaying DM produces a signal proportional to n_X, and annihilating DM scales as n_X^2 : neither mechanism intrinsically follows the baryonic distribution.

3.3.3 A$\overline{\text{Q}}$N**s emission in an ionised dilute medium**

As discussed above, when $T_{\text{A}\overline{\text{Q}}\text{N}} > 0$, the A$\overline{\text{Q}}$N acquires a net electric charge, $Q < 0$. If $|Q|$ exceeds a certain threshold and the surrounding medium is ionised, Eq.(10) no longer applies. In this regime, the long-range Coulomb attraction must be taken into account. This enhances the effective interaction cross-section, increases the baryon capture rate, and consequently leads to a higher annihilation rate and a larger equilibrium temperature $T_{\text{A}\overline{\text{Q}}\text{N}}$. The equilibrium will still be reached, but it now explicitly depends on the gas temperature $T_{\rm gas}$. The reason is that the impact cross-section of the Coulomb interaction depends on the speed of the incoming baryon: for a given impact parameter, faster baryons will be less likely to be captured by the charged A$\overline{\text{Q}}$N than slower baryons. Therefore, **a higher** $T_{\rm gas}$ **will not heat an** A$\overline{\text{Q}}$N **as much as a lower**

$T_{\rm gas}$, everything else being equal. Taking this effect into account, the A$\overline{\rm Q}$N temperature is given by Majidi et al. (2024a):

$$\boxed{T_{\rm A\overline{Q}N} = \left[\frac{3\pi}{4}\,\frac{2\,{\rm GeV}}{16\,\alpha^{5/2}}\,f\,(1-g)\,m_e^{1/4}\,\Delta{\rm v}\,n_{\rm ion}\left(\frac{\sigma_{\rm eff}}{\sigma_{\rm geo}}\right)\right]^{4/17}}, \tag{12}$$

where n_b has been replaced by $n_{\rm ion}$, the number density of ions. This equation is similar to Eq.(10), but with an enhancement factor set by the ratio of the effective to geometrical cross-sections:

$$\frac{\sigma_{\rm eff}}{\sigma_{\rm geo}} = \left(\frac{R_{\rm eff}}{R_{\rm A\overline{Q}N}}\right)^2 = 8\,\alpha\,m_e^2\,R_{\rm A\overline{Q}N}^2\left(\frac{T_{\rm A\overline{Q}N}}{T_{\rm gas}}\right)^2\sqrt{\frac{T_{\rm A\overline{Q}N}}{m_e}}\,. \tag{13}$$

By definition, the ratio $\sigma_{\rm eff}/\sigma_{\rm geo}$ cannot be smaller than unity (with the exception of negatively charged ions in the medium, for which the Coulomb interaction would be repulsive). In practice, this means that whenever the gas temperature $T_{\rm gas}$ implies $\sigma_{\rm eff} < \sigma_{\rm geo}$, the geometrical cross-section must be adopted.

Eq.(12) and Eq.(13) are not valid in dense or semi-dense environments. In these regimes, ion capture becomes efficient: large numbers of ions accumulate around the A$\overline{\rm Q}$N, partially shielding its electric charge and consequently reducing $|Q|$.

Key takeaways. In a fully ionised medium, the emission properties of A$\overline{\rm Q}$Ns are determined by a **self-consistent feedback loop** involving charge build-up, baryon capture and annihilation, and cooling via thermal emission. The resulting equilibrium temperature $T_{\rm A\overline{Q}N}$ is given by Eq. (12). In a partially ionised medium, the temperature must be computed from a combination of Eqs. (10) and (12).

In the following three subsections, we use hydrodynamical simulations to evaluate the A$\overline{\rm Q}$N emission in two distinct environments, large-scale structures and the Milky Way, dilute enough for Eq.(10) and Eq.(12) to apply.

3.4 Observations in dilute environments

3.4.1 A$\overline{\rm Q}$Ns contribution to the sky monopole

Could the A$\overline{\rm Q}$N thermal emission contribute substantially to the sky monopole at any wavelength, potentially leading to an excess that would invalidate the QCD-AQN framework? Using the Magneticum simulation[5], Majidi et al. (2024b) constructed light cones and computed the cumulative A$\overline{\rm Q}$N emission from $z \sim 6$ to $z = 0$. The simulation outputs include the gas temperature and the velocity fields for both DM and baryons, but the ionisation fraction is not computed. However, given that by $z \sim 7$–8 the Universe is fully reionised, and large-scale hydrogen has not subsequently recombined, it is reasonable to assume a fully ionised medium.

Fig. 10 presents the sky-averaged thermal emission from A$\overline{\rm Q}$Ns, compared with the measured sky monopole. The sole free parameter of the framework, the mean A$\overline{\rm Q}$N mass, $\langle m_{\rm A\overline{Q}N}\rangle$, was set to 100 g. We see that the A$\overline{\rm Q}$N thermal component contributes a non-negligible fraction of the sky monopole only at very low frequencies, $\nu \lesssim 1$ GHz, where the ARCADE 2 excess was reported (Fixsen et al. (2011)). Across the remainder of the electromagnetic spectrum, the contribution remains subdominant. It should be noted that increasing $\langle m_{\rm A\overline{Q}N}\rangle$ would enhance the A$\overline{\rm Q}$N overall emissivity. Consequently, the observed sky intensity imposes an upper bound on $\langle m_{\rm A\overline{Q}N}\rangle$, as discussed in the following subsection.

[5]Magneticum denotes the *Magneticum Pathfinder* cosmological simulation suite, a set of large-volume hydrodynamical ΛCDM simulations including dark matter, baryons, star formation, black-hole feedback, and magnetic fields, commonly used to model galaxy and cluster formation and the baryonic content of haloes.

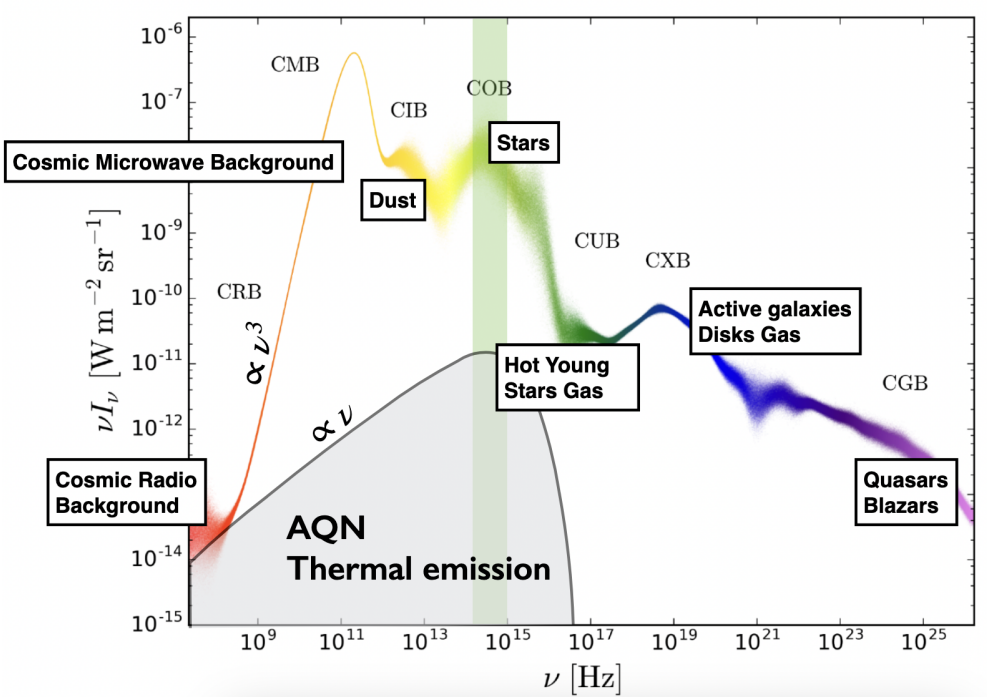


Figure 10: Comparison of the AQ̄N thermal emission calculated for $\langle m_{\mathrm{A\bar{Q}N}} \rangle = 100\,\mathrm{g}$ to the sky monopole calculated by Hill et al. (2018).

3.4.2 AQ̄Ns and South Pole Telescope observations

The sky monopole serves as a consistency check to ensure that any DM emission does not exceed current observational limits, but the anisotropies of the mass distribution provide a far more informative testing ground: Model predictions can be confronted with data through their dependence on redshift, physical scale, environment, and observing frequency.

The QCD-AQN framework predicts an emission signal that correlates with both dark matter and baryons, and can therefore be tested using cosmological surveys that map the sky at specific wavelengths. At present, the most sensitive high-resolution, wide-area maps suitable for this purpose are found in the radio and far-infrared bands, notably from the South Pole Telescope (SPT) Balkenhol et al. (2023), the Atacama Cosmology Telescope Madhavacheril et al. (2024) and Planck Planck Collaboration et al. (2020).

Using the same light-cone simulations as in (3.4.1), Majidi et al. (2024b) computed the AQ̄N fluctuation spectrum, C_ℓ. Fig. 11 compares the predicted angular power spectrum of millimetre-wave fluctuations from AQ̄Ns with measurements from SPT for $\langle m_{\mathrm{A\bar{Q}N}} \rangle = [10\,\mathrm{g}, 10^2\,\mathrm{g}, 10^3\,\mathrm{g}]$.

Above $\ell \sim 3000$, the signal measured by SPT is dominated by conventional extragalactic and galactic foregrounds, including dusty star-forming galaxies and the thermal and kinetic Sunyaev–Zel'dovich effects Reichardt et al. (2021). Any AQ̄N contribution must therefore act as a subdominant component. Consequently, Fig. 11 may be interpreted as placing an upper limit on the amplitude of AQ̄N-induced emission fluctuations, which translates into an upper bound on the mean AQ̄N mass:

$$\langle m_{\mathrm{A\bar{Q}N}} \rangle \lesssim 2 \times 10^2\ \mathrm{g}. \tag{14}$$

Provided that the AQ̄N mass remains below this upper bound, the predicted AQ̄N signal lies systematically below the power measured by SPT across the full multipole range considered. Moreover, the upper bound $\langle m_{\mathrm{A\bar{Q}N}} \rangle = 200\,\mathrm{g}$ does not lead to an overproduction of optical emission that would be inconsistent with the sky monopole. This is illustrated in Fig. 10, where the AQ̄N signal is shown for $\langle m_{\mathrm{A\bar{Q}N}} \rangle = 100\,\mathrm{g}$.

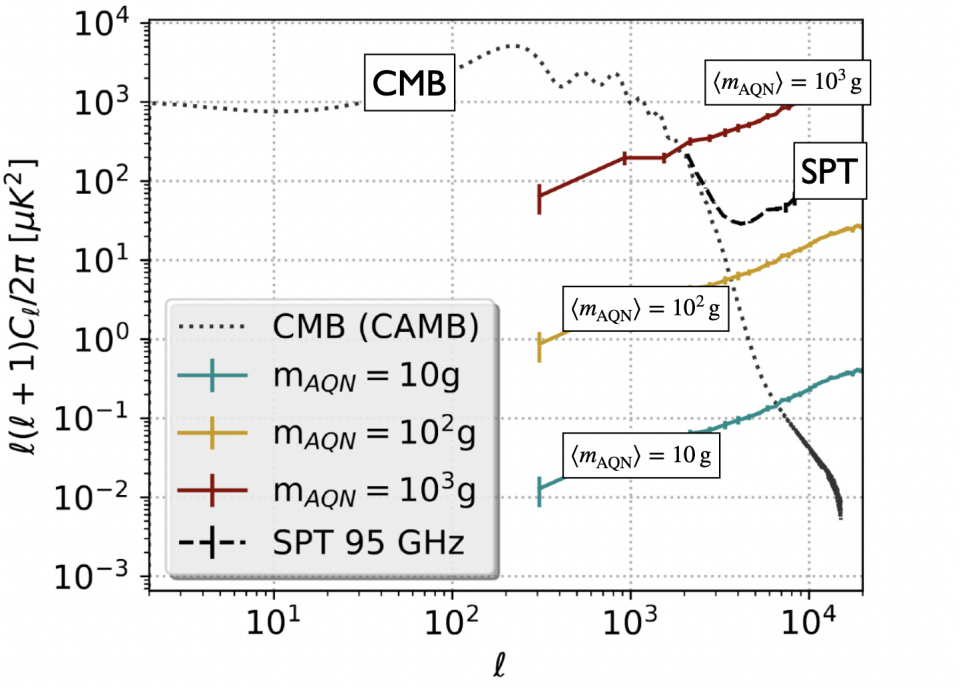


Figure 11: A$\overline{\text{Q}}$N emission fluctuations compared to the South Pole Telescope measurements for various values of the mean A$\overline{\text{Q}}$N mass Majidi et al. (2024b).

Key takeaway. The thermal emission associated with A$\overline{\text{Q}}$Ns does *not* significantly overproduce small-scale anisotropies and is fully compatible with current SPT measurements. It sets an upper limit on the mean A$\overline{\text{Q}}$N mass compatible with observations of the all-sky mean intensity.

3.4.3 A$\overline{\text{Q}}$Ns and Galactic UV background observations

The ultraviolet window offers a complementary probe of the QCD-AQN framework, since temperatures in the range $T_{\text{A}\overline{\text{Q}}\text{N}} \sim 1$–$10\,\text{eV}$ produce emission extending into the UV (see Fig.9). Observationally, the NUV-FUV sky ($\sim 2800 - 1300\,\text{Å}$) is largely dominated by low redshift sources $z \lesssim 0.3 - 0.8$, with a strong contribution from the Milky-Way and UV emitting stars.

Henry et al. (2015) analysed diffuse far-ultraviolet (FUV) maps obtained with GALEX (see Fig.12). A Galactic dust-scattered component was modelled using the FUV–FIR ($\sim 100, \mu$m) cross-correlation and subtracted from the GALEX maps. The remaining emission is nearly isotropic, with an intensity of $\sim$ 300–500 photon counts. Using deep GALEX and HST galaxy surveys and the Quasars/Active Galactic Nuclei UV luminosity function, they argue that the total extragalactic component intensity is $I_{\text{ext}} \sim 100 - 150$ photon counts. A substantial residual component, $I_{\text{excess}} \sim$ 200–300 photon counts, remains of unknown origin. It is characterised by a remarkable degree of uniformity and symmetry at high Galactic latitudes, shows no correlation with Galactic dust nor stellar UV sources and is present in both the northern and southern Galactic poles. To evaluate a dark matter origin for the excess, Henry et al. (2015) calculated the UV emission expected from WIMPs and PBHs, and found that the predicted intensity falls short of the observed signal by roughly ten orders of magnitude.

In the Solar System environment, FUV photons have a relatively short mean free path, $L \sim 0.5$–$1\,\text{kpc}$. The FUV band is therefore particularly well suited to testing the QCD-AQN framework within the $\sim \text{kpc}^3$ volume surrounding the Sun, where the distributions of DM and baryons are reasonably well constrained. Sekatchev et al. (2025) computed the FUV intensity produced by baryon–A$\overline{\text{Q}}$N annihilation within a region of radius $\sim 1\,\text{kpc}$ around the Sun. In order to obtain a realistic distri-

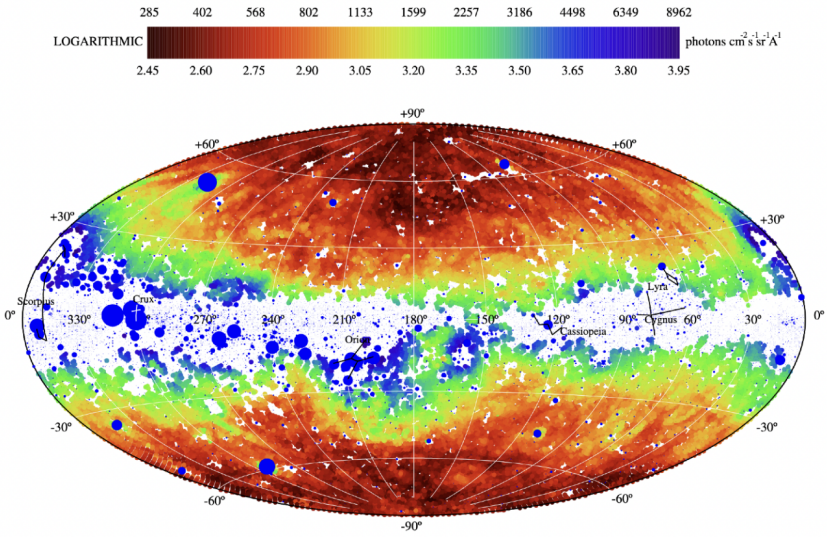


Figure 12: FUV galactic background map measured by GALEX (from Henry et al. (2015)). Notice the isotropic excess at the galactic poles.

bution of DM and baryons they used state-of-the-art FIRE-2 Latte simulations of individual Milky Way–like galaxies and they selected 281 sites whose DM density, baryon content, and ionisation fraction closely resemble those of the Solar System. The distribution of photon units counts for $\langle m_{A\overline{Q}N}\rangle = [10\,\mathrm{g}, 10^2\,\mathrm{g}, 5\times10^2\,\mathrm{g}]$ is shown on Fig.13. The authors demonstrated that the $A\overline{Q}N$ annihilation emissivity produces a FUV intensity similar to the excess observed by GALEX. Their results show that

$$\langle m_{A\overline{Q}N}\rangle \sim 10^1\text{–}10^3\ \mathrm{g} \tag{15}$$

produces both the amplitude and the band-averaged intensity of the signal measured by Henry et al. (2015). Although not constituting proof, the agreement between this mass range and those discussed in Sections 3.2.1 and 3.2.2 provides evidence for the internal consistency of the QCD-AQN framework.

Critics of the analysis by Henry et al. (2015) argued that, GALEX being a low-Earth orbit instrument, the reported UV excess could arise from, or be biased by, residual systematics in the zodiacal light subtraction. However, Murthy et al. (2025) extended and refined GALEX's UV measurements with the Alice ultraviolet spectrograph aboard the New Horizons spacecraft (2014–2023). Thirty-six spectra from independent lines-of-sights were taken at 5×10^9 km away from the Sun, near Pluton's orbit where the zodiacal light is negligible. The New Horizons measurements are in perfect agreement with GALEX, confirming the presence of a diffuse Galactic FUV component in excess of the predictions from standard dust-scattered light models. The detected signal exhibits only weak correlations with dust tracers and shows consistency across multiple independent sky directions.

Update (November 2026): New observational support for the AQN interpretation

Murthy et al. (2026) provide new support for the existence of the unexplained UV background previously detected by GALEX. Using archival GALEX observations of both Galactic poles, the authors carefully model the contribution from starlight scattered by interstellar dust and subtract known Galactic and extragalactic sources. They identify a remarkably uniform residual emission of 165 ± 18 photon units in the FUV (1530 Å) and 346 ± 34 photon units in the NUV (2360 Å). Crucially, both the amplitude and the spectral ratio of this unexplained emission are consistent with predictions from QCD-AQN, providing encouraging independent support for the AQN interpretation.

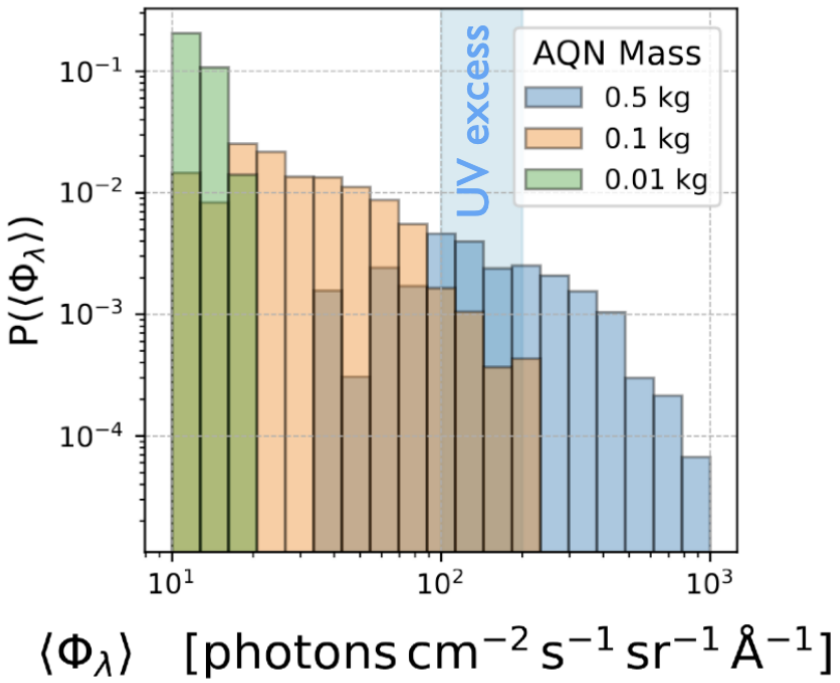


Figure 13: Probability distributions $P(\langle\Phi_\lambda\rangle)$ of the A$\overline{\text{Q}}$N FUV signal from voxels surrounding the candidate solar neighbourhood regions for three values of the A$\overline{\text{Q}}$N masse, with Δv modelled with a Maxwell–Boltzmann distribution Sekatchev et al. (2025).

3.4.4 A$\overline{\text{Q}}$Ns and CMB observations

Majidi et al. (2025) investigated whether energy injection from A$\overline{\text{Q}}$Ns into the primordial plasma prior to recombination could generate CMB anisotropies or spectral distortions at a level sufficient to challenge the viability of the QCD-AQN framework. They concluded that A$\overline{\text{Q}}$Ns do not produce any detectable signature in the TT, TE, or EE anisotropy power spectra and that μ- and y-type distortions remain below the sensitivity threshold of COBE/FIRAS.

A distinctive prediction of the QCD-AQN framework is that continuous annihilation results in μ-type distortion exceeding the y-type component by a factor of ~ 3. Such a μ-to-y ratio is not expected in other DM energy-injection scenarios. Detection of such distortions would require a next-generation CMB spectral distortion mission, such as the proposed PIXIE experiment. ESA's Voyage 2050 programme provides a long-term strategic framework within which such missions could potentially emerge.

3.5 A$\overline{\text{Q}}$Ns interactions with dense objects

Having examined some aspects of the thermal emission of A$\overline{\text{Q}}$Ns and the resulting diffuse glow produced through their interaction with ambient baryons in dilute media, it is now important to explore the encounters of A$\overline{\text{Q}}$Ns with dense astrophysical bodies (stars and planets), as it offers an independent avenue for testing the AQN hypothesis beyond cosmology.

3.5.1 Example 1: the Sun

While matter AQNs cross stars unaffected, $\overline{\text{AQ}}$Ns may imprint observable signatures in stellar plasmas. The most natural laboratory in which to search for such effects is our own Sun.

Following the initial 2017 paper by Zhitnitsky (2017), Raza et al. (2018) examined whether $\overline{\text{AQ}}$Ns could contribute to the heating of the solar corona. The solar corona emits a continuous EUV radiation that persists in quiet regions of the Sun and remains present even during the minima of the solar activity cycle. Maintaining the corona requires a sustained energy input of approximately

$$L_{\text{corona}} \sim 10^{27}\,\text{erg.s}^{-1}.$$

The solar corona is thought to reside near a self-organised criticality (SOC) state, in which even minor perturbations can initiate magnetic reconnection within pre-existing current sheets. However, the precise physical trigger responsible for the ubiquitous small-scale heating events is still under debate. While small-scale impulsive brightenings are routinely observed in the solar atmosphere, the even smaller nanoflares required to account for coronal heating are expected to lie below the resolution limits of current instruments.

Using shock-wave theory and without introducing additional free parameters, Raza et al. (2018) evaluate the energy deposition resulting from A$\overline{\text{Q}}$N interactions with the solar plasma. Collisions between $\overline{\text{AQ}}$Ns and solar baryons produce photons, leptons, and hadrons that rapidly thermalise in the tenuous coronal environment, generating localised heating events in the 10^{21}–10^{26} erg range, comparable to nanoflares.

$\overline{\text{AQ}}$Ns enter the solar atmosphere with a typical Galactic halo velocity of $v \simeq 220\,\text{km}\,\text{s}^{-1}$, which sets the impact parameter relevant for gravitational capture by the Sun. As they descend, the ambient plasma density increases, and the annihilation rate rises with local density:

- In very low-density regions, annihilation is inefficient.
- In very high-density regions (deeper layers), $\overline{\text{AQ}}$Ns rapidly lose kinetic energy and the annihilation rate increases.

By combining the solar density profile, the DM velocity, the annihilation cross-section, and the plasma response, Raza et al. (2018) found that the peak energy deposition occurs within the transition region between the chromosphere and the corona (a narrow layer where plasma temperature abruptly rises from $\sim 10^4\,\text{K}$ to $\sim 10^6\,\text{K}$).

The total power deposited onto the Sun depends on the DM flux and is largely independent of the detailed A$\overline{\text{Q}}$N mass distribution. Interestingly, inserting independently measured DM Galactic parameters yields an energy deposition rate of $\sim 10^{27}\,\text{erg}\,\text{s}^{-1}$, of the same order of magnitude as L_{corona}, without tuning solar inputs.

The annihilation of A$\overline{\text{Q}}$N could thus contribute substantially to the heating of the solar corona. The advantage of this mechanism is that it reproduces nanoflare-like statistics without invoking unresolved magnetic reconnection. It also provides a heating channel that operates even in magnetically quiet regions of the solar atmosphere.

Path Forward A first-principles MHD simulation demonstrating that A$\overline{\text{Q}}$N injection can initiate magnetic reconnection is still required to establish $\overline{\text{AQ}}$Ns as a viable nanoflare trigger mechanism.

The observed nanoflare energy distribution follows

$$P(E) \propto E^{-\alpha},$$

with $\alpha \sim 1.5$–2, consistent with SOC phenomenology. In such systems, the avalanche slope is largely insensitive to the microscopic origin of the trigger. Here, the critical observable is not the precise value of α, but instead the event rate and temporal statistics, which can be extracted from high-cadence EUV and X-ray nanoflare catalogues (for example, from SDO/AIA Pesnell et al. (2012)).

3.5.2 Example 2 : the Earth

The terrestrial environment provides the next natural setting in which to search for A$\overline{\text{Q}}$N signatures. Adopting a local DM density in the Solar System of $\rho_{\rm DM} \simeq 0.3\,{\rm GeV\,cm^{-3}}$, and assuming a mean mass $\langle m_{\rm A\overline{Q}N}\rangle \sim 10\,{\rm g}$, one can estimate the terrestrial encounter rate. Under these assumptions, approximately 4×10^7 A$\overline{\text{Q}}$Ns intersect the Earth's surface each year. This corresponds to an average flux of roughly $\sim$ 10 A$\overline{\text{Q}}$Ns per 3,000 km^2 per year, with characteristic velocities of order $v \sim 220\,{\rm km\,s^{-1}}$. An A$\overline{\text{Q}}$N traversing the Earth is heated through interactions with terrestrial matter Ge et al. (2022), emerges largely intact and exits the Earth as a hot A$\overline{\text{Q}}$N ($T_{\rm A\overline{Q}N} \sim 100-200\,{\rm keV}$), subsequently emitting X-rays in the $\sim 1-10\,{\rm keV}$ range over distances of up to $\sim 10\,R_\oplus$. At ground level, the associated radiation dose would be less hazardous than that of a typical medical CT scan.

Seasonal variations in the DM detection rate are a standard and important consistency check for any Earth-based detection strategy. Their study was motivated by the claim of Fraser et al. (2014) that XMM-Newton observations of the diffuse X-ray background in the 6 keV band exhibit a statistically significant annual modulation of $\sim$ 20%, which exceeds the typical modulation of $\sim 5-10\%$ expected by direct DM detection experiments.

Ge et al. (2022) investigated the seasonal modulation of near-Earth X-ray emission arising from the orbital motion of the Earth around the Sun, while the Solar System moves through the Galaxy (at $\sim 220\,{\rm km\,s^{-1}}$). They found that the X-rays most relevant to an orbiting observatory are produced near the "exit" point of an A$\overline{\text{Q}}$N trajectory after it has traversed the Earth. The resulting emission is therefore associated with A$\overline{\text{Q}}$N Earth-transit and depends on the changing orientation of the Earth relative to the incoming DM flow. Because this mechanism relies not only on the seasonal variations in the Earth's speed through the Galactic halo, but also on directional effects, the predicted annual modulation can be substantially larger than that expected in conventional particle DM models. Ge et al. (2022) estimated that the resulting seasonal variation could reach the $\sim$ 20–25% level, an amplitude broadly compatible with the modulation reported in the XMM-Newton analysis. They further argued that the radiation spectrum produced by A$\overline{\text{Q}}$N interactions during transit through the Earth can account for emission in the 6 keV band without the need for extreme fine-tuning, hence presented this signal as a generic consequence of A$\overline{\text{Q}}$N–matter interactions[6].

Lawson et al. (2019); Liang et al. (2020) examined the dynamical, thermal, and observational consequences of an A$\overline{\text{Q}}$N traversing the Earth. They showed that A$\overline{\text{Q}}$Ns can pass through the planet without undergoing catastrophic disruption, thereby demonstrating the effective transparency of the Earth to such composite objects. Their analysis indicates that no large-scale melting, shock formation, or structural damage is produced, explaining why A$\overline{\text{Q}}$Ns are not excluded by existing geological constraints. Ge et al. (2022) further argued that, under favourable conditions, current seismic networks could in principle be sensitive to the passage of A$\overline{\text{Q}}$Ns, offering a potential – albeit challenging – avenue for direct detection.

Key takeaways. The Earth should be continuously crossed by AQNs, producing X-ray with a large seasonal modulation, while remaining consistent with geological and observational constraints, making the terrestrial environment a viable — though challenging — detection channel.

3.5.3 Example 3: neutron-stars

Neutron stars (NSs) are compact stellar remnants with masses of approximately 1.2–2 $M_\odot$ and radii $R_{\rm NS} \sim$ 10–15 km. The magnetic field strength of an ordinary neutron star is typically

[6]No variations associated with the Earth's seasons are expected when measurements are conducted far from the Earth and with cameras that never point toward the planet. This constitutes a distinctive feature of the QCD-AQN framework, as the A$\overline{\text{Q}}$N's emission can transmit information about the Earth's seasonal cycle to distances as large as $\sim 10\,{\rm R_{Earth}}$.

$\mathcal{B} \simeq 10^{10}$–$10^{13}$ G, whereas magnetars host the strongest magnetic fields known in the Universe, reaching $\mathcal{B} \simeq 10^{14}$–$10^{15}$ G. Given the enormous energy stored in such fields, an important question is what impact infalling AQNs might have on these systems.

In the same manner as the Sun, a neutron star will gravitationally capture AQNs, but it will do it with a large impact parameter $b_{\rm cap}$:

$$\frac{b_{\rm cap}}{R_{\rm NS}} \simeq \frac{c}{v_\infty}\left(\frac{10^6\,{\rm cm}}{R_{\rm NS}}\right)^{1/2}\left(\frac{M_{\rm NS}}{2\,M_\odot}\right)^{1/2} \gg 1.$$

A number of AQNs comparable to the number accreted by the Sun will be captured and fall onto a single NS. This is a substantial flux of particles, particularly in view of the very small physical size of a neutron star.

Van Waerbeke and Zhitnitsky (2019) analyse the interaction of AQNs with neutron-star magnetospheres. Using simple dynamical arguments and elementary shock wave physics in plasma, they show that both matter and antimatter AQNs can considerably speed up the magnetic reconnection in a NS magnetosphere. The argument is based on the fact that AQNs will reach the speed of light, $v_{\rm AQN} \sim c$, larger than the speed of sound, leading to a Mach number of the order:

$$M \simeq 20\left(\frac{1\,{\rm MeV}}{k_B T}\right)^{1/2}\left(\frac{10^6\,{\rm cm}}{R_{\rm NS}}\right)^{1/2}\left(\frac{M_{\rm NS}}{2\,M_\odot}\right)^{1/2}.$$

Consequently, the matter flow can reach $v \sim c$ locally, leading to an Alfvén Mach number $M_A \sim 1$. This will considerably accelerate the magnetic reconnection and release vast amounts of energy. From this key point, Van Waerbeke and Zhitnitsky (2019) calculated the amount of energy released by reconnection events triggered by the shock wave generated by AQNs falling on a magnetar. They found that it is consistent with the coherent plasma radiation mechanism proposed by Kumar et al. (2017); Lu and Kumar (2018) that could be at the origin of Fast Radio Bursts (FRBs).

The appeal of this work lies in the absence of ad hoc parameter adjustment: the burst frequency, duration, and energy scale are set by independently motivated quantities (axion mass, DM density, magnetar magnetic field strength and magnetar abundance). Moreover, the prediction that FRBs should originate preferentially in strongly magnetised neutron stars preceded and is consistent with subsequent observational evidence linking FRBs to magnetars Bochenek et al. (2020). Zhitnitsky (2024) discussed other proposals that could link AQNs to NS.

3.5.4 Additional constrains on the mean $A\overline{Q}N$ mass

IceCube constrains

Considering the extremely low number density of $A\overline{Q}$Ns, direct detection is exceedingly unlikely. IceCube's non-detection of $A\overline{Q}N$-like events implies that $A\overline{Q}$Ns must be sufficiently massive for their flux through the detector to be extremely small Lawson et al. (2019). This places a lower bound on the $A\overline{Q}N$ mean mass:

$$\langle m_{A\overline{Q}N}\rangle \gtrsim 5\,{\rm g}, \tag{16}$$

For smaller masses, $A\overline{Q}$Ns would be too numerous and would deposit enough energy through annihilation, ionisation, and secondary particle production to generate detectable, highly penetrating tracks.

Geothermal constrains

The Earth's geothermal heat flow is well measured, which strongly constrains any dark-matter population that deposits energy while passing through or being captured by the Earth. As a result, geothermal data place robust limits on the mass, interaction cross-section, and flux of macroscopic DM candidates. According to Gorham (2012), macros can contribute no more than

$\sim$ a quarter of Earth's heat flow, impling that, for an AQN population making up the local DM density:

$$\langle m_{A\overline{Q}N} \rangle \gtrsim 4\,\mathrm{g}. \tag{17}$$

Antartic Impulsive Transient Antenna

The Antartic Impulsive Transient Antenna (ANITA) is a long-duration balloon experiment that flies above Antarctica to detect nanosecond-scale radio pulses from ultra-high-energy particle interactions in the Antarctic ice. During its 2014 flight, the *ANITA* experiment detected an $\sim 10^{18}$ eV upward-going, cosmic-ray–like radio event emerging at roughly 30° above the horizontal, implying a chord length through Earth of roughly 5,000–7,000 km Gorham et al. (2018). During its 2016 flight, the *ANITA* experiment reported a second upward-going cosmic-ray–like radio event with an energy of $\sim 1-4\times10^{18}$ eV, emerging at approximately 35° above the horizontal, corresponding to an even longer Earth-crossing distance ANITA Collaboration et al. (2020).

These observations present a striking challenge to conventional ultra-high-energy neutrino interpretations: At *ANITA* energies ($E_\nu \sim 10^{17}$–10^{19} eV), the neutrino–nucleon scattering cross section grows to $\sim 10^{-33}\,\mathrm{cm}^2$, so the Earth becomes effectively opaque to such neutrinos. Liang and Zhitnitsky (2022) interpreted the upward-going events as A$\overline{Q}$Ns exiting the surface. The heated aggregate and its ionisation trail can generate a coherent radio pulse that mimics an upward-going air shower. A key distinction is that, unlike a point-like neutrino, an A$\overline{Q}$N deposits energy continuously along a track, leading to characteristic polarisation, duration, and angular features.

A$\overline{Q}$N mass bound

A mean mass $\langle m_{A\overline{Q}N} \rangle \gtrsim$ 1-10 g is required for an A$\overline{Q}$N to survive propagation through a substantial chord of the Earth, and for the emerging shower to match *ANITA*'s observed energy scale. On the other hand, for $\langle m_{A\overline{Q}N} \rangle \gg 100\,\mathrm{g}$, the flux would be too small to explain two *ANITA* events within the exposure time, leading to an approximate mass window:

$$\text{1-10}\,\mathrm{g} \lesssim \langle m_{A\overline{Q}N} \rangle \lesssim 1000\,\mathrm{g} \tag{18}$$

This window is consistent with mass ranges that have been derived previously from independent considerations.

3.5.5 Synthesis of observational constraints

To summarise 3.4 and 3.5, Tables 4 and 5 compile the principal mass-range constraints and the consistency of A$\overline{Q}$N-induced energy injection across the relevant astrophysical and terrestrial environments.

Theory	$[m_{\min}, m_{\max}]$	**Ref.**
AQNs survival/Limited formation time	$[10^{-2}, 10^{4}]$g	4.6.1
Independent observations	**Mean mass** $\langle m_{A\overline{Q}N} \rangle$	
SPT small-scale anisotropies	$\langle m_{A\overline{Q}N} \rangle \lesssim 2\times10^{2}\,\mathrm{g}$	Eq.(14)
GALEX & ALICE UV background constraints	$1\,\mathrm{g} \lesssim \langle m_{A\overline{Q}N} \rangle \lesssim 10^{3}\,\mathrm{g}$	Eq.(15)
IceCube non-detection constraints	$5\,\mathrm{g} \lesssim \langle m_{A\overline{Q}N} \rangle$	Eq.(16)
Geothermal heat flow	$4\,\mathrm{g} \lesssim \langle m_{A\overline{Q}N} \rangle$	Eq.(17)
ANITA up-going events (rate + energetics)	$\sim$ 1–10^{3} g	Eq.(18)

Table 4: Summary of observational and theoretical constraints on the mean A$\overline{Q}$N mass.

Environments	$A\overline{Q}N$ energy injection	Ref.
Sky monopole (multi-wavelength)	Compatible with observed sky-averaged intensity	3.4.1
CMB	Compatible with anisotropies and spectral distortions	3.4.2
Solar corona heating	Compatible with nanoflare energetics	3.5.1
Magnetars (burst energetics)	Compatible with FRB rates and energetics	3.5.3
Seasonal variations of the diffuse X-ray background	Compatible with XMM-Newton observations	3.5.2

Table 5: Consistency of $A\overline{Q}N$-induced energy injection with selected astrophysical environments.

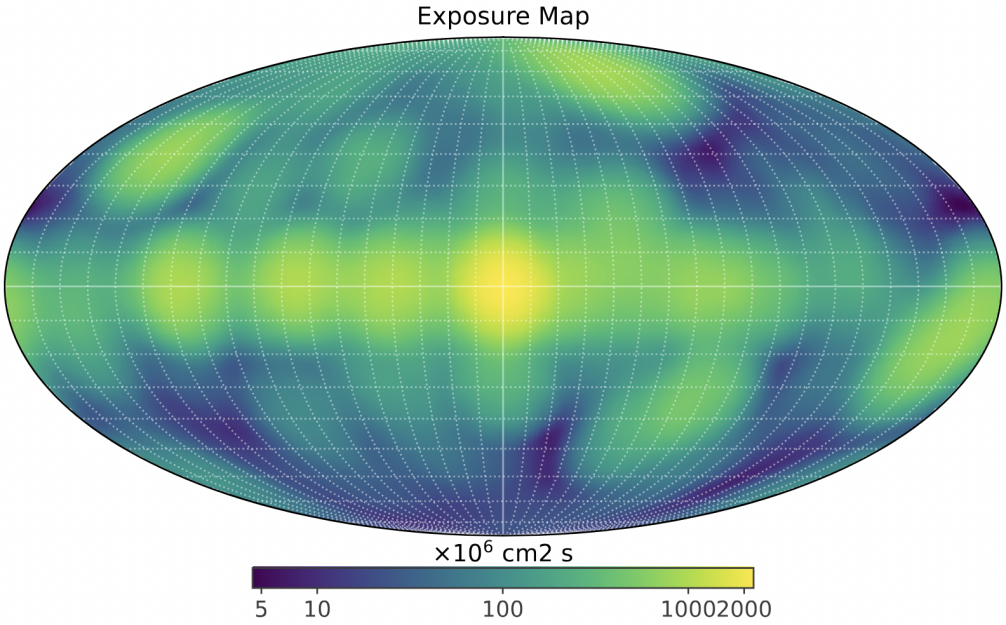


Figure 14: Exposure map for the 511 keV line observations with INTEGRAL/SPI over 20 years in Galactic coordinates. Image adapted from `www.aanda.org/articles/aa/pdf/2025/10/aa55895-25.pdf`.

3.6 Upcoming tests for the QCD-AQN framework

The QCD-AQN framework must be confronted with observations in any astrophysical environment where $A\overline{Q}N$s encounter a sufficiently high baryon density to trigger annihilation. We outline below the principal observational tests that will be pursued in the near future.

3.6.1 511 keV emission in the Galactic bulge

Observations, notably by INTEGRAL/SPI (Fig.14), reveal an intense and spatially extended emission from the Galactic bulge, corresponding to a positron injection rate of order $\dot{N}_{e^+} \sim 10^{43}\,\mathrm{s}^{-1}$. While several astrophysical sources are capable of producing positrons – including β^+-decaying radioactive isotopes synthesised in supernovae, pulsars, microquasars, and low-mass X-ray binaries – most of these populations trace the Galactic disc rather than the observed bulge.

As $A\overline{Q}N$s traverse the dense bulge environment, baryons from the interstellar medium annihilate on their surface, releasing energy that heats the surrounding positron cloud and leads to the emission of low-energy positrons. These positrons subsequently thermalise and annihilate in the interstellar medium, producing the observed 511 keV line. This scenario was suggested by Oaknin and Zhitnitsky (2005) in order to simultaneously explain the bulge-dominated mor-

phology of the emission and the relatively low injection energies implied by the narrow line width, while avoiding the overproduction of high-energy gamma rays. Another distinctive feature of the QCD-AQN framework is that the emitted signal is correlated with baryonic matter, as demonstrated by Eq. (11), in contrast to annihilating or decaying DM scenarios. It remains to be seen if the framework can predict a 511 keV intensity map – obtained from realistic Galactic DM and baryon density distributions – consistent with the observed spatial extent, symmetry, and surface-brightness profile of the bulge emission.

3.6.2 Cosmic dawn and 21-cm cosmology

The energy difference ΔE between the $1s$ hyperfine levels of neutral hydrogen defines the spin temperature T_S.[7]

$$\frac{n_1}{n_0} = \frac{g_1}{g_0} e^{-\frac{h\nu}{k_B T_S}} = 3e^{-\frac{\Delta E}{k_B T_S}}$$

where ΔE corresponds to $\lambda = 21\,\text{cm}$ (1420 MHz). The 21-cm signal is observed either in absorption or emission against the CMB and can only be observed when $T_S \neq T_{\text{CMB}}$. Throughout the history of the Universe:

- Between $1100 \gtrsim z \gtrsim 200$ the gas temperature remains equal to the CMB temperature because of Compton scattering between CMB photons and residual free electrons. This process keeps the baryon gas thermally coupled to the radiation even after recombination, hence $T_S = T_{\text{gas}} = T_{\text{CMB}}$.
- Between $200 \gtrsim z \gtrsim 40$, the gas cools faster than the CMB but collisional coupling maintains $T_S \simeq T_{\text{gas}} < T_{\text{CMB}}$, hence the 21cm is seen in absorption against the CMB.
- As the universe continues expanding, at $z \sim 30$–40 collisional coupling becomes less effective than CMB photons scattering and $T_S \simeq T_{\text{CMB}} > T_{\text{gas}}$: the 21cm signal disappears.
- Then the first stars form and inject UV and X-ray photons. The mechanism known as the Wouthuysen-Field effect (Wouthuysen 1952, Field 1958) redistributes electrons between the two hyperfine levels and results in $T_S \sim T_{\text{gas}}$: the 21-cm signal is seen in absorption again.
- At the beginning of the reionisation era ($z \sim 15$) the gas temperature rises well above T_{CMB} and the 21-cm signal is seen in emission again.

There has been no confirmed detection of the global 21-cm signal to date[8], although it remains an area of intensive research. The interaction between A$\overline{\text{Q}}$Ns and baryons provides several mechanisms by which the 21-cm signal could be modified, either enhancing absorption or driving emission. In particular, the injection of low-energy photons would contribute to the radio background in addition to the CMB, while higher-energy UV and X-ray photons could alter the thermal and ionisation history of the intergalactic medium. In this context, precision 21-cm cosmology may constitute a decisive empirical test of the QCD-AQN scenario.

3.6.3 ARCADE 2 and the cosmic radio background

As shown in Fig. 10, the A$\overline{\text{Q}}$N emission can make an appreciable contribution to the sky monopole only at low frequencies, specifically below 1GHz. One potential origin of such low-frequency emission is the cumulative low-energy radiation produced during the cosmic dark ages.

The ARCADE 2 excess refers to an unexpectedly bright, diffuse radio background detected at frequencies below approximately 10 GHz Fixsen et al. (2011). This signal is nearly isotropic,

[7] n_1 is the number density of neutral hydrogen atoms in the excited (triplet) hyperfine level of the 1s ground state, while n_0 is the number density of atoms in the lower-energy (singlet) hyperfine level.

[8] The EDGES collaboration reported the detection of an unexpectedly deep 21-cm absorption feature at redshift $z \sim 17$ Bowman et al. (2018). It is still debated.

significantly exceeds the contribution anticipated from known galactic and extragalactic radio sources, and follows a smooth power-law spectrum with a steep spectral index ($T \propto \nu^{-2.6}$).

Any potential connection between the ARCADE 2 excess and a cosmic radio background generated within the QCD-AQN framework (as suggested in Lawson and Zhitnitsky (2013a)) must, however, be treated with caution. A substantial radio background at high redshift would fundamentally alter the reference against which the 21-cm line is observed. Rather than hydrogen interacting solely with the CMB radiation bath, it would experience a brighter effective radio background, thereby enhancing the depth of the absorption signal without modifying the underlying spin physics Feng and Holder (2018). Note that this effect can be reversed by heat injection into the gas, for example through soft photons Cyr et al. (2024). The gas can also be heated by ionising photons. As discussed in Section 3.4.2, A$\overline{\text{Q}}$Ns also inject UV and X-ray photons. This additional energy input heats the gas and reduces the 21-cm absorption amplitude, potentially offsetting or even cancelling the enhanced absorption caused by an excess radio background.

If the A$\overline{\text{Q}}$N radio emission is indeed related to the ARCADE excess, it would necessarily also be linked non-trivially to the global 21-cm signal. Taken together, measurements of the radio background and the 21-cm line could provide a decisive test of the QCD-AQN framework.

Update (November 2026): Recent developments concerning the ARCADE 2 excess

McKay et al. (2026), using improved absolute calibration of the radio sky between 60 and 350 MHz, find that existing sky models underestimate the brightness. Their revised analysis increases the inferred excess at 150 MHz from 171 K to 201 ± 24 K, strengthening the case for an unidentified low-frequency radio component. Complementary results presented by Hernández-Monteagudo (2026), using QUIJOTE observations at 11 and 13 GHz cross-correlated with extragalactic surveys, suggest that radio emission tracing large-scale structure accounts for only 20–30% of the ARCADE 2 excess. The remaining component could therefore be Galactic or nearly isotropic and extragalactic. These findings motivate further investigation of diffuse radio emission predicted by the QCD-AQN framework, particularly at frequencies below 1 GHz.

3.6.4 Where and how to search for A$\overline{\text{Q}}$N signatures

The detectability of A$\overline{\text{Q}}$N-induced phenomena depends sensitively on the physical properties of the surrounding medium. Because A$\overline{\text{Q}}$Ns interact predominantly through annihilation with baryons, the strength and character of any observable signatures are controlled by the local baryon density and the ionisation fraction of the gas. In practice, this implies that potential signatures must be sought across a wide range of environments: large-scale structure and galaxy clusters, galactic haloes, stellar and planetary atmospheres, and the interstellar medium. A$\overline{\text{Q}}$Ns could also modify the thermal and ionisation history of the early Universe. As a continuous source of ionising photons, they may contribute during the epoch of reionisation. An additional radiation component of this type could delay the cooling of primordial gas into molecular hydrogen, thereby affecting the onset of early star formation and possibly the formation of the first black holes.

The breadth of these potential consequences might suggest that A$\overline{\text{Q}}$N signatures should be ubiquitous and therefore already detected. However, this intuition is misleading: the presence of many possible channels does not imply that each produces a large or easily identifiable signal. Not all astrophysical environments are conducive to producing detectable imprints. For instance, massive O and B stars possess radiative envelopes, and their outer atmospheres are dominated by strong, fast stellar winds. Any localised energy deposition from an A$\overline{\text{Q}}$N would be rapidly advected away, preventing the build-up of a sustained coronal signature, leaving no clear A$\overline{\text{Q}}$N-induced observational imprint. By contrast, low- and intermediate-mass stars with convective envelopes host magnetically confined coronae. In these systems, A$\overline{\text{Q}}$N energy injection could trigger magnetic reconnection events and contribute to coronal heating.

A comparatively more accessible environment is the Earth's atmosphere, where both ground-based detectors and balloon-borne experiments (e.g. Adams et al. (2015)) can be deployed. Although a single 100 g A$\overline{\text{Q}}$N carries an energy comparable to several megatons of TNT, even in this environment observational signatures are typically subtle. This is because a very large amount of energy would be deposited along an extended trajectory, in contrast to the case of point-like explosions. A$\overline{\text{Q}}$Ns may interact with terrestrial thunderstorms, which are characterised by strong, large-scale electric fields capable of accelerating charged particles toward the aggregates. This enhanced baryon flux onto the A$\overline{\text{Q}}$N surface would increase the annihilation rate and lead to rapid, localised energy release, potentially producing spallation-like particle cascades. Zhitnitsky and Maroudas (2025) argues that such interactions could generate bursts of relativistic particles, gamma rays, and radio emission, thereby offering a possible connection between A$\overline{\text{Q}}$Ns and transient high-energy atmospheric phenomena.

Liang et al. (2020) has demonstrated that the detection of a daily modulation in the flux of high-velocity axions could serve as a signature of A$\overline{\text{Q}}$Ns that have recently traversed the Earth. These axions are naturally generated through the interaction of the axion domain wall with terrestrial matter during transit. Searches for such daily modulations, induced by AQNs crossing the Earth, have already commenced Caspers et al. (2025); Kim et al. (2025).

Finally, searching for A$\overline{\text{Q}}$N signatures frequently demands substantial expertise, significant computational resources, and the analysis of large observational datasets. One example is detailed in Sommer et al. (2024), who develop an observational strategy to detect A$\overline{\text{Q}}$N signatures in nearby, well-characterised galaxy clusters such as Virgo and Fornax. They conclude that a multi-wavelength approach is essential. Any candidate A$\overline{\text{Q}}$N emission must be carefully separated from dominant astrophysical backgrounds, particularly the thermal bremsstrahlung from the intracluster medium in X-rays and the non-thermal synchrotron radiation from cosmic rays in radio. This requires robust component separation and consistent modelling across different frequency bands. Another example is the search for the so-called "dark glow", which we now discuss.

Key takeaway. The search for observational evidence of AQNs mainly focuses on diffuse sky background maps. Signals previously discarded as noise in past observations could contain valuable information, and may warrant renewed attention.

3.7 Prediction: the dark glow

Figure 10 demonstrates that the A$\overline{\text{Q}}$N signal can generate a diffuse uniform glow across the sky, potentially extending into the UV. One therefore expects that the A$\overline{\text{Q}}$N emission should display anisotropies over a broad range of frequencies, from the radio to the UV. Fig. 11 shows the anisotropy spectrum, C_ℓ, at $\nu = 95\,\text{GHz}$ for three different values of the mean A$\overline{\text{Q}}$N mass. The principal challenge is that the predicted signal, the so called dark glow, is extremely faint, and therefore these fluctuations cannot be detected individually.

The new space observatories Euclid and James Webb Space Telescope provide an exceptionally stable environment for ultra-faint photometry, enabling exploration of the extremely low surface-brightness Universe. Fig. 15 displays an image of the Perseus cluster obtained with the Euclid space telescope, with an inset showing a magnified region of the background sky where no discrete sources are detected. Thanks to the stability of space-based imaging, it may be possible to search for fluctuations in the sky background that lie below the nominal sky level itself.

Majidi et al. (2024b) demonstrated that extending the SPT anisotropy spectrum to optical wavelengths yields a signal that lies within the nominal detection threshold of Euclid Cuillandre et al. (2025). The grey region in Fig. 16 represents the expected A$\overline{\text{Q}}$N signal at $\ell = 3000$ as a function of frequency, for $\langle m_{\text{A}\overline{\text{Q}}\text{N}} \rangle$ in the range 10–100 g. The coloured rectangles denote the projected $1\,\sigma$ uncertainties achievable with SPT-3G, COSMOS-Web, and the Euclid Wide Survey. It

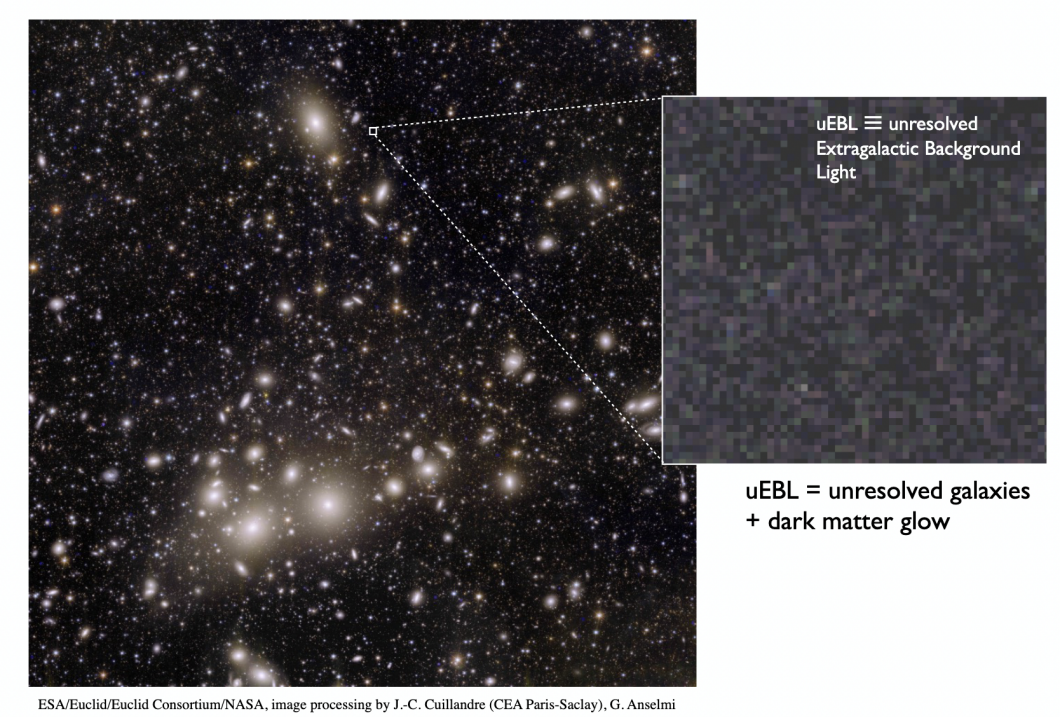


Figure 15: (Left) Euclid image of the Extragalatic Background Light (EBL). (Right) Zoom in on the unresolved EBL (uEBL), obtained after removing resolved sources. The uEBL consist of unresolved galaxies and the dark-matter glow.

can be seen that the predicted root-mean-square dark glow amplitude falls within the anticipated sensitivity of each of these instruments.

Components separation

Fig. 16 shows the potential for a statistical detection of the A$\overline{\text{Q}}$N glow, not an individual fluctuation detection. A statistical detection relies on components separation techniques and cross-correlations. The emission from unresolved galaxies originates at intermediate to high redshifts, typically $z \sim 1$–3, whereas the dark glow arises from energy injection by A$\overline{\text{Q}}$Ns throughout cosmic history and contributes to anisotropies and spectral distortions over a very broad redshift range ($z \gtrsim 5$).

From observations of the Extragalactic Background Light (EBL), one can remove the resolved sources in order to isolate the unresolved Extragalactic Background Light (uEBL), as illustrated in Fig. 15. The uEBL has never been used as a scientific observable in the optical/NIR; standard pipelines treat it as a nuisance and discard it, however it could be transformed it into a window for observational cosmology, reaching z $>$ 6 and enabling probes of the Universe's history up to the Epoch of Reionisation.

Contrary to unresolved galaxies, the intensity of the dark-glow signal increases with redshift (Majidi et al). Using the intensity fluctuations within the uEBL, the dark-glow signal can be distinguished from unresolved galaxy light by its distinctive dependence on redshift z, electromagnetic frequency ν, and harmonic wavenumber l. Detecting a significant dark glow at high-redshift would indicate that dark matter interacts with ordinary matter, a paradigm shift in itself that would strenghten the case for macroscopic DM. Futhermore, a (z, ν, ℓ) dependence of the observed signal that matches the predictions of the QCD-AQN model would constitute compelling evidence that AQNs are a leading dark-matter candidate.

Can the unresolved extragalactic background light become a new cosmological observ-

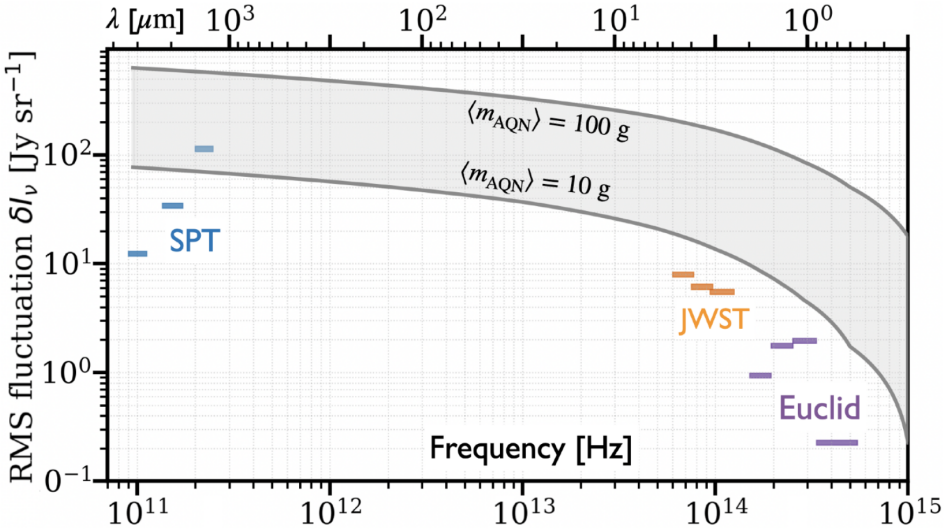


Figure 16: Simulated RMS of AQ̄N density fluctuations at $\ell = 3000$ for $\langle m_{\bar{\text{AQN}}} \rangle \in [10 - 100]$g, cumulative across all redshifts. The coloured rectangles indicate a 1 σ uncertainties for the Euclid Wide and JWST's COSMOS-Web surveys for $\langle m_{\bar{\text{AQN}}} \rangle = 10$ g, and the 1 σ uncertainties of the Cosmological Infrared Background component from SPT-SZ Reichardt et al. (2021).

able? (2026 update)

A recent study by Li et al. (2026) introduces a new method for estimating the redshift distribution of unresolved galaxies directly from multi-band maps of the cosmic optical background. The approach combines realistic cosmological simulations with machine learning, using conditional normalising flows to reconstruct the probability distribution of source redshifts without identifying individual galaxies. The analysis exploits the complementarity between Euclid and the Vera C. Rubin Observatory's LSST, whose combined observations provide ten photometric bands spanning optical and near-infrared wavelengths. Under idealised conditions, the method achieves sub-percent accuracy in the mean and standard deviation of flux-weighted redshift distributions. It also enables tomographic reconstruction, separating the unresolved background into contributions from different redshift intervals. Although discrepancies between simulations and real observations remain an important challenge, this represents a promising step towards using the unresolved extragalactic background light as a cosmological observable.

3.8 AQN detection on Earth (2026 update)

Proposed Network to Detect Axion Quark Nugget Dark Matter

Liang et al. (2021) propose a terrestrial network of synchronised detectors designed to identify signatures AQNs and reconstruct the direction and velocity of the incoming dark matter flux. As antimatter AQNs traverse the Earth's atmosphere and interior, annihilation with ordinary matter releases energy, producing electromagnetic radiation and relativistic axions through excitations of the surrounding axion domain wall.

The proposed strategy exploits correlations between signals recorded at spatially separated stations. Unlike conventional single-detector experiments, a synchronised network can distinguish transient AQN-induced events from uncorrelated instrumental and astrophysical backgrounds. Two complementary detection channels are investigated. For relativistic axions, the authors propose a network of stations separated by approximately 100 km, arranged in a trian-

gular configuration with additional detectors to reconstruct the incident direction. For X-rays, whose atmospheric attenuation length is much shorter, they favour compact arrays of detectors separated by tens of metres, organised into tetrahedral units.

4 AQNs in the early Universe

The QCD-AQN framework is rooted in Quantum Chromodynamics, the quantum field theory that describes the strong nuclear force. Formulated in the early 1970s Weinberg (1996), QCD is based on the non-Abelian gauge group $SU(3)_{\text{colour}}$. It describes quarks interacting through the exchange of massless gauge bosons called gluons. Asymptotic freedom Gross and Wilczek (1973); Politzer (1973) implies that quarks and gluons are never observed in isolation but are bound into hadrons. QCD is one of the most thoroughly experimentally tested components of the Standard Model of particle physics and is regarded as a firmly established and quantitatively verified theory of the strong interaction Particle Data Group et al. (2024).

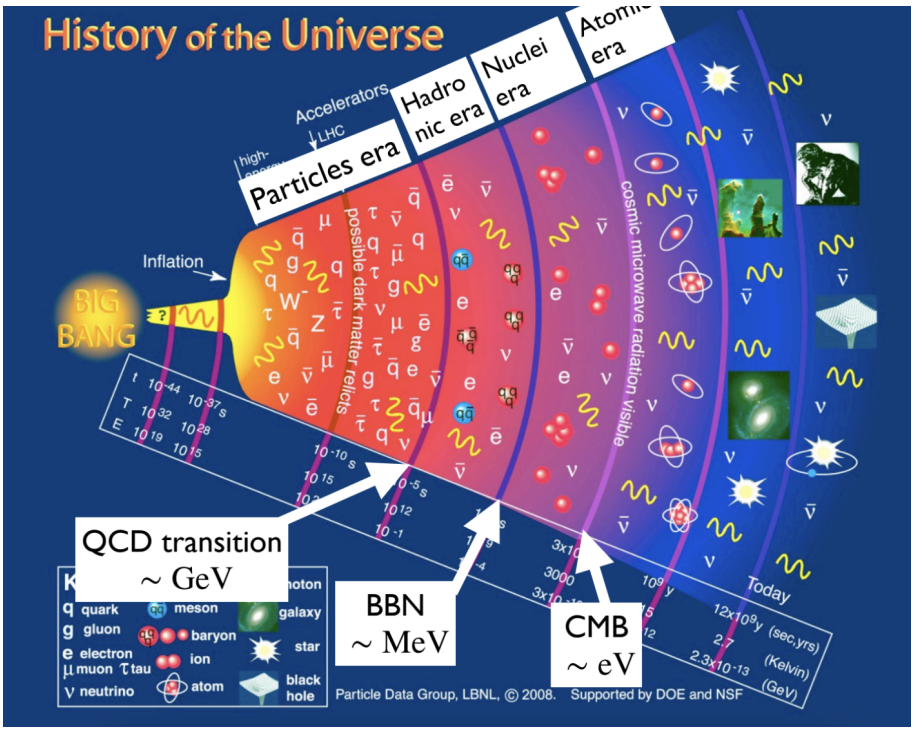


Figure 17: History of the Universe (from Particle Data Group, 2008)), annotated to highlight QCD transition, BBN and CMB.

4.1 AQN formation

The formation of AQNs, first hypothesised by Zhitnitsky in 2003 Zhitnitsky (2003), begins at the QCD transition in the early Universe (Fig. 17), at temperatures of order $T \sim 170$MeV ($t \sim 10^{-5}$ s), when quarks and gluons become confined into hadrons. Fig.18 illustrates several possible AQN formation pathways within the QCD phase diagram: either via the hadron gas phase or through the quark–gluon plasma, before completing their evolution in the colour-superconducting phase.

The formation of AQNs requires the presence of an axion field, which constitutes **the sole extension of the Standard Model of particle physics employed in the QCD-AQN framework.** This hypothesis is well motivated, as it is presently the only viable solution to the strong CP

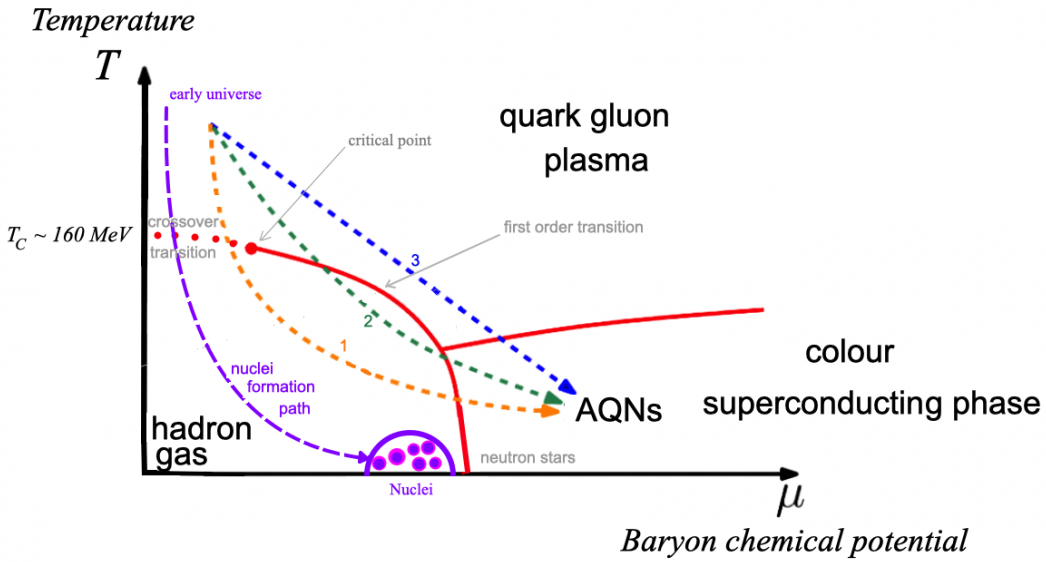


Figure 18: The QCD phase diagram and its three phases: quark-gluon plasma, hadron gas and colour superconductor. Possible formation pathways for AQNs are numbered 1,2,3. The nuclei formation pathway (dashed purple line) passes through the crossover transition and proceeds within the hadron gas phase. Adapted from Ge et al. (2018)

problem[9].

- **The strong CP problem**

The "strong CP problem" can be stated as follows: Why does QCD appear to conserve CP symmetry, even though the theory permits a term that would produce large CP violation? In the QCD Lagrangian, the CP-violating term can be written as :

$$\mathcal{L}_\theta = \theta \frac{g_s^2}{32\pi^2} G^a_{\mu\nu} \widetilde{G}^{\mu\nu}_a, \tag{19}$$

where $G^a_{\mu\nu}$ is the gluons field and g_s is the strong force coupling constant. θ is a free parameter which is strongly constraints by experiments, the strongest upper bound being $|\theta| \lesssim 10^{-10}$ from the absence of detection of a neutron electric dipole moment Abel et al. (2020). This constitutes the so-called strong CP problem: within the Standard Model, there is no symmetry that naturally enforces such an extraordinarily small value of θ.

- **The Peccei–Quinn mechanism**

The original Peccei–Quinn (PQ) proposal Peccei and Quinn (1977) correctly identified a dynamical solution to the strong CP problem by introducing a global symmetry $U(1)_{\mathrm{PQ}}$ with a new complexe scalar field ϕ:

$$\phi(x) \equiv (f_a + \rho(x))e^{i\alpha},$$

where α is a new global symmetry and $f_a = \langle\phi\rangle$ is the axion decay constant. The dynamical solution consists in assuming a spontaneous symmetry breaking at scale f_a and promote α, the phase of ϕ, to a dynamical field a/f_a. A new term appears in the Lagrangian:

[9]"CP" symmetry means the combined charge conjugation (C) and parity (P) symmetry.

$$\mathcal{L}_{aG\tilde{G}} = \frac{a(x)}{f_a} \frac{g_s^2}{32\pi^2} G^a_{\mu\nu} \widetilde{G}^{\mu\nu}_a.$$

The CP violating term in (Eq. 19) can now be expressed as an effective angle θ_{eff}:

$$\theta_{\text{eff}} \equiv \theta + \frac{a(x)}{f_a}.$$

In QCD, the axion mass m_a is given by:

$$m_a^2 = \frac{\chi_{\text{top}}(T)}{f_a^2},$$

where $\chi_{\text{top}}(T)$ is the QCD topological susceptibility[10]. In the limits of low $T \sim 0$ and high temperature $T \gg \Lambda_{\text{QCD}}$, the topological susceptibility can be calculated analytically:

$$\begin{cases} \chi_{\text{top}}(T \sim 0) \propto m_\pi^2 f_\pi^2, \\ \chi_{\text{top}}(T \gg \Lambda_{\text{QCD}}) \propto \Lambda_{\text{QCD}}^4 \left(\dfrac{\Lambda_{\text{QCD}}}{T}\right)^n, \qquad \text{with } n \sim 7\text{–}8, \end{cases} \tag{20}$$

where $\Lambda_{\text{QCD}} \sim 100 - 200\,\text{MeV}$, m_π is the pion mass and f_π is the pion decay constant[11]. As a result, the mass of the axion field varies greatly over cosmic time:

$$m_a(T \sim 0) \approx 5.7\,\mu\text{eV} \left(\frac{10^{12}\,\text{GeV}}{f_a}\right), \tag{21a}$$

$$m_a(T \gg \Lambda_{\text{QCD}}) \propto \frac{1}{f_a} \left(\frac{\Lambda_{\text{QCD}}}{T}\right)^{n/2} \xrightarrow[T\to\infty]{} 0. \tag{21b}$$

Originally, the Peccei–Quinn proposal identified the axion symmetry-breaking scale f_a with the electroweak scale, $f_a \sim 250\,\text{GeV}$. This led to a large axion mass $m_a \sim 100\,\text{keV}$, as shown by Eq.(21), and therefore strong couplings to Standard Model particles. It predicted observable effects in particle experiments and significant signatures in stellar cooling that were in strong conflict with collider constraints and astrophysical observations. Nevertheless, although the original PQ axion scale turned out to be phenomenologically excluded, the axion mechanism itself remains a viable solution to the strong CP problem Peccei (2008).

- **Axion dynamics and the onset of AQN formation**

DFSZ and KSVZ[12] showed that one can realise the PQ symmetry breaking differently, allowing the breaking scale f_a to be arbitrarily large. With such a large value, the axion field becomes *invisible*, and the cosmological impact of the axion field can be re-evaluated. After PQ breaking, the axion remains essentially massless, until, at $T \sim 1\,\text{GeV}$, non-perturbative QCD effects generate a potential $V(a)$ for the axion:

$$V(a) \sim \chi_{\text{top}}(T) \left(1 - \cos\left(\frac{a}{f_a} + \theta\right)\right), \tag{22}$$

[10]The QCD topological susceptibility measures how strongly the QCD vacuum responds to the CP-violating parameter θ; physically, it quantifies the strength of non-perturbative topological fluctuations that generate the axion potential and mass.

[11]The pion properties encode the structure of the QCD vacuum and sets the scale of the QCD topological susceptibility.

[12]Dine–Fischler–Srednicki–Zhitnitsky Dine et al. (1981); Zhitnitsky (1980) and Kim–Shifman–Vainshtein–Zakharov Kim (1979); Shifman et al. (1980).

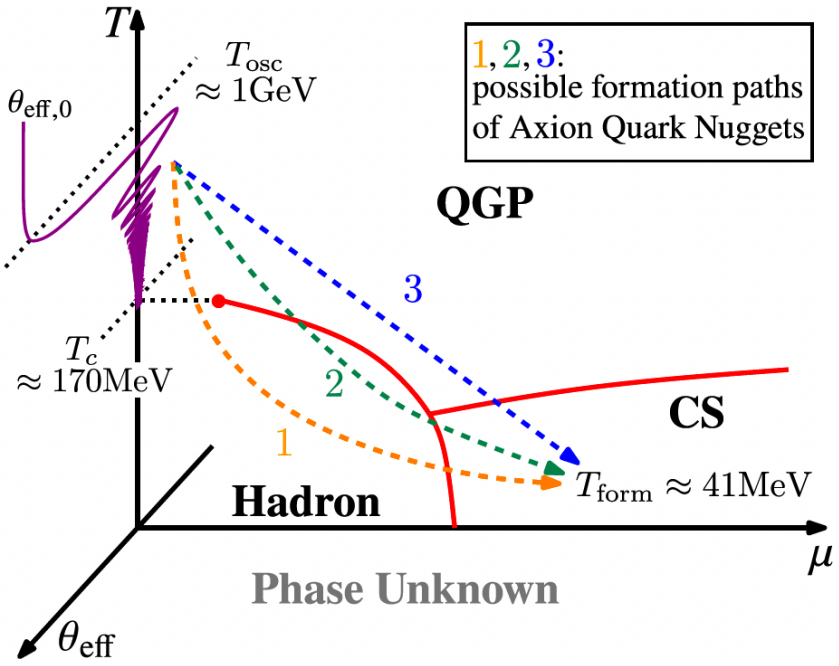


Figure 19: The oscillations of $\theta_{\rm eff}$ between $T \sim 1$ GeV and $T \sim 170$ MeV and three possible AQN formation pathways. The AQNs condensation starts aroung 200 MeV in the quark-gluon phase (QGP). The baryon number of the aggregates grows as they migrate through the diagram. The AQNs formation is complete ~ 41 MeV. From Ge et al. (2018)

where $\chi_{\rm top}(T)$ is given by Eq.(20). As a result, the axion field a begins to relax towards the minimum of $V(a)$, thereby cancelling the θ term and driving $\theta_{\rm eff} \to 0$, hence resolving the strong CP problem.

It is at this stage, $T \sim 1$ GeV, that the AQN formation begins. In the limit of small mass density perturbations, one finds that the homogeneous axion field a satisfies the equation of a harmonic oscillator damped by Hubble friction:

$$\ddot{a} + 3H\dot{a} + m_a^2(T)\, a = 0. \tag{23}$$

From Eq.(21), one can see that at $T \gg 1$ GeV, the axion mass is extremely small $m_a \sim 0$, hence the axion field is *frozen* because the Hubble friction term dominates. At $T \sim 1$ GeV, calculations show that $m_a \sim 3H$ and the field starts to oscillate globally. As the Universe continues expanding, the restoring force dominates over the Hubble damping: the field can now roll and oscillate about the minimum of the potential while $\theta_{\rm eff} \to 0$. At $T \sim 1$ GeV, the effective angle reaches $\theta_{\rm eff} \simeq 10^{-3} - 10^{-2}$.

Figure 19 illustrates the evolution and oscillatory behaviour of $\theta_{\rm eff}$ as the Universe cools. Note that the third axis defines a new region of the QCD phase diagram that remains entirely unknown.

- **The axion field configuration at the QCD epoch**

What is the spatial configuration of the axion field across the Universe at $T \sim 1$ GeV? The answer depends on whether the PQ symmetry breaking happens before or after inflation.

If the PQ symmetry breaks before inflation[13], then at $T \sim 1$ GeV, $\theta_{\rm eff} \simeq 10^{-3} - 10^{-2}$ assumes the same *frozen* value everywhere in the Universe. As the Universe expands and cools, topological regions with $\theta_{\rm eff} \to \theta_{\rm eff} + 2\pi$ are formed (see Eq.(22)). These regions assume the same vacuum expectation value $V(\theta_{\rm eff}) = V(\theta_{\rm eff} + 2\pi)$, but they are topologically distinct. $\mathrm{N_{DW}} = 1$ domain walls form and Vilenkin and Shellard (1994), Chang et al. (1998) showed that approximately 10% of them form closed configurations. Domain walls normally decay when intersected by strings, but for sufficiently small closed walls the probability of such an intersection is low, allowing them to survive. These small, closed domain walls can subsequently collapse and give rise to AQNs.

- **Axion-η' domain walls and dynamical quark trapping**

In 2003, Zhitnitsky (2003) proposed that the collapse of the above-mentioned closed domain walls can be halted if a sufficiently large number of quarks become trapped inside them. However, the axion field alone cannot confine quarks, and there is no strict prohibition preventing quarks from crossing the domain-wall boundaries. This raises the question of how quarks can remain trapped within the walls.

As shown in Liang and Zhitnitsky (2016) and Ge et al. (2017), axion domain walls are not purely axionic objects. It is a well-established property of QCD that the axion coupling to the gluonic operator $G\tilde{G}$ implies that any spatial variation of $\theta_{\rm eff}$ necessarily excites the η' meson[14]. It means that axion domain walls boundaries where $\theta_{\rm eff}$ jumps by 2π, also contain a layer of η' meson, implying that the walls acquires a nontrivial CP-odd structure through coupled axion–η' dynamics. At the onset of domain wall formation, equal numbers of quarks and antiquarks are present both inside and outside the wall, which they can cross freely. The axion–η' structure subsequently favours one species over the other. As a result, some domain walls acquire an excess of quarks, while others acquire an excess of antiquarks. At a later stage, the quarks (or antiquarks) confined within a closed domain wall become compressed into a dense colour-superconducting (CS) phase, whose bulk free energy can be lower than that of the surrounding vacuum. Fermi pressure and the CS pairing counteract the collapse. Once the CS phase forms, it becomes energetically costly for quarks to leave, and the system behaves as if the quarks are "trapped." The trapping is therefore dynamical and thermodynamic, not due to an impenetrable microscopic barrier.

During this dynamical phase, the oscillating axion background acts as a CP-odd bias, effectively behaving like a chemical potential for baryon number: $\Delta\mu_B \sim \dot{\theta}_{\rm eff}$. Integrated coherently over many oscillations during the collapse, this bias leads to a macroscopic baryon number accumulation inside the AQN. Once the configuration stabilizes, the baryon number is conserved, even as $\theta_{\rm eff} \to 0$.

- **Baryon-charge separation**

At $T \sim 1$ GeV, when the axion oscillations begin and acts as an effective baryonic chemical potential, $\Delta\mu_B \sim \dot{\theta}_{\rm eff}$, the sign of $\dot{\theta}_{\rm eff}$ is the same everywhere within a given CP-odd region. The collapse of different domain walls happens at different times and the collapse dynamics are stochastic. Hence, some bubbles will start collapsing when $\dot{\theta}_{\rm eff} > 0$ and some when $\dot{\theta}_{\rm eff} < 0$. Once the sign inside a bubble is set, each oscillation cycle will generate a very small $\Delta\mu_B$ enhacing

[13] Only this scenario is explored in this subsection, for the sake of simplicity. The second scenario will be explained in (4.7).

[14] This is the QCD response to the anomalous $U(1)_A$ symmetry

the baryon number $|B|$ of the bubble. The larger the $|B|$, the more energetically favourable it becomes for quarks (antiquarks) to remain confined within the AQN ($A\overline{Q}N$). This is a runaway selection effect: Once a sign is selected by the initial bias, it reinforces itself, and each bubble ultimately acquires a large $|B|$.[15]

- **Color superconductivity and the freeze-out of AQN formation**

When the AQN core enters a CS phase, quarks (antiquarks) near the Fermi surface form Cooper pairs and the excitation spectrum develops an energy gap:

$$\Delta_{CS} \sim \Lambda_{\rm QCD}.$$

Consequently, exciting higher-energy states becomes more difficult at temperature $T \ll \Delta_{CS}$.

Various studies indicate that $\Delta_{\rm CS} \sim 40-60\,$MeV Alford et al. (1999); Rajagopal and Wilczek (2001); Lugones and Horvath (2002); Rüster et al. (2005); Alford et al. (2008). Hence, when the cosmic temperature drops below $T \lesssim 40\,$MeV, creating or removing quark excitations requires an amount of energy greater than the thermal bath can supply. Quark excitation inside the AQN becomes rare, quark evaporation is suppressed and quark accretion becomes inefficient. As a result, baryon exchange across the AQN boundary becomes exponentially suppressed, and the baryon number freezes. This marks the end of the active phase of AQN formation. From that point onward, AQNs with baryon number in the range $|B| \sim 10^{22}$–10^{28} are remarkably stable Ge et al. (2019), enough to survive to the present epoch.

4.2 Matter-antimatter asymmetry

- **Why $\Omega_{\rm DM} \sim \Omega_b$**

The final asymmetry between matter and antimatter AQNs is of order unity because the axion field oscillates a very large number of times, $\sim 10^7$, during the epoch when closed domain walls form and baryon-charge separation occurs. If the initial CP violating parameter was exactly zero ($\theta_{\rm eff} = 0$) at $T \sim 1\,$GeV, equal numbers of AQNs and $A\overline{Q}$Ns would form and no visible baryons would remain. With the small nonzero CP violation at $T \sim 1\,$GeV, the oscillating axion background slightly favours one sign. Over many collapse events, a small statistical bias gradually builds up and ultimately becomes of order unity. This baryon-charge separation mechanism implies that the total baryon number of the Universe remains zero at all times:

$$B_{\rm universe} = B_{\rm visible} + B_{\rm AQN} + \bar{B}_{A\overline{Q}N} = 0 \tag{24}$$

The resulting effect is an order-unity asymmetry between the total baryon number stored in matter AQNs and antimatter $A\overline{Q}$Ns, which can be parametrised as

$$\bar{B}_{A\overline{Q}N} = c(T_{\rm form})\, B_{\rm AQN}, \qquad |c(T_{\rm form})| \sim \mathcal{O}(1). \tag{25}$$

Hence, assuming the asymmetry favours antimatter (i.e. $|B_{\rm AQN}| < |B_{A\overline{Q}N}|$), a population of free baryons will remain unbound. This naturally leads to $\Omega_{DM} \simeq \Omega_b$.

- **Masses of matter and antimatter AQNs**

[15] The asymmetry only affects a thin layer at the surface of the closed domain wall that bounds the AQN, which thickness is determined by the QCD physical scale ${\Lambda_{\rm QCD}}^{-1}$: The baryon-charge separation is essentially a surface effect rather than a volume effect.

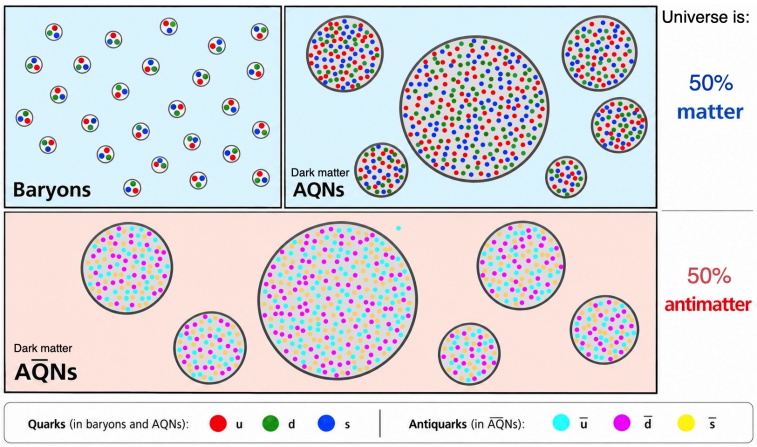


Figure 20: Visible matter, AQNs and antimatter A$\overline{\text{Q}}$Ns before BBN. The axion-induced CP violation at the QCD epoch biases quark versus antiquark capture during formation, sequestering more antibaryon number in antimatter AQNs and thereby producing the observed visible baryon excess.

Matter and antimatter AQNs originate from the same population of closed axion domain walls produced with random orientations of the axion field. The sign of the baryon number accumulated on a given wall is determined by the local value of $\dot{\theta}_{\rm eff}$ at the time of formation, but this does not affect the probability that a closed wall forms. As a result, the formation mechanism produces comparable numbers of matter and antimatter AQNs:

$$n_{\underline{\rm AQN}} \sim n_{\overline{\rm AQN}}.$$

The baryon number asymmetry manifests itself through an asymmetric mass distribution of aggregates, with antimatter A$\overline{\text{Q}}$Ns being, on average, more massive than matter A$\underline{\text{Q}}$Ns:

$$\langle m_{\underline{\rm AQN}} \rangle < \langle m_{\overline{\rm AQN}} \rangle$$

- **Mass densities ratio**

A precise determination of the ratio $\Omega_b : \Omega_{\rm AQN} : \Omega_{\overline{\rm AQN}}$ would require non-perturbative QCD calculations, which are currently beyond reach. For the purpose of a visual illustration, let us assume that all other DM components are subdominant (including conventional axion production) and that $\Omega_{\rm DM} \simeq 5\,\Omega_{\rm visible}$. Equation (24) then implies relative density fractions of approximately $1:6$ for visible matter, $2:6$ for matter AQNs, and $3:6$ for antimatter AQNs. This situation is illustrated in Fig. 20. The main purpose of this illustration is to emphasise that:

(ii) the number densities of the two populations are of the same order;

(i) the mean baryon number stored in antimatter A$\overline{\text{Q}}$Ns exceeds that stored in matter AQNs, hence A$\overline{\text{Q}}$N are represented with a larger radius..

4.3 AQNs remarkable stability

Ge et al. (2019) investigated the stability and survival of AQNs during the early stages of the Universe. At high temperatures, $T \gg 1\,$MeV, most collisions between protons and AQNs lead to elastic scattering : the resulting mass loss from annihilation processes remains negligible.

- **AQNs during BBN**

AQNs formation ends at $T_{\rm form} \sim 40\,\mathrm{MeV}$, far before the BBN energy scale $T_{\rm BBN} \sim 1\,\mathrm{MeV}$. By the time nucleosynthesis begins, AQNs are already macroscopic, tightly bound objects in a CS phase, with a binding energy per baryon of order $\Lambda_{\rm QCD} \sim 100\,\mathrm{MeV}$, far exceeding BBN thermal energies. Their interaction cross section per baryon is geometrically suppressed, preventing significant participation in nuclear reactions. They neither disrupt light-element abundances (except for heavy nuclei, see Section 4.5) nor inject sufficient energy to alter neutron-proton freeze-out or the standard BBN expansion history Zhitnitsky (2021).

One may ask how antiquark aggregates can survive in such a hot, relativistic plasma with a large particle number density, composed of electrons, positrons, and, most importantly, a dense population of free baryons at high temperature. Electron-positron pairs remain in thermal equilibrium down to temperatures of order $T \sim 20\,\mathrm{keV}$. It was shown in Flambaum and Zhitnitsky (2019) that the large positron number density inhibits the capture of baryons (protons and helium nuclei) by $\mathrm{A\overline{Q}N}$, thereby preventing rapid annihilation. The positrons remain sufficiently abundant for long enough to form an effective shielding layer around the aggregate.

- **AQNs between BBN and recombination**

AQNs remain stable throughout the period between BBN and the CMB epoch. During this interval, the plasma is both dense and fully ionised from the perspective of an AQN. Interactions between AQNs and such a medium are analysed in Majidi et al. (2025), while the more general conditions prevailing from the post-BBN era up to recombination are discussed in Ge et al. (2019).

In contrast to the BBN epoch, the Coulomb capture rate of ambient protons in a $T \sim$ eV–keV plasma is significantly enhanced. Because nuclei move more slowly than during BBN, the efficiency of Coulomb capture increases. The resulting large capture rate produces a screening layer around the AQNs, which prevents any runaway annihilation. For typical baryon numbers $|B| \sim 10^{22}$–10^{28}, the corresponding annihilation rate — and thus the associated mass loss — remains negligibly small.

- **Post recombination**

For the remainder of cosmic history, thermal and collisional processes in most astrophysical environments are far too weak to disrupt AQNs. Their enormous binding energy, combined with their extremely low number density, renders catastrophic collisions exceedingly unlikely. Only a minuscule fraction of antimatter aggregates lose a significant amount of energy through interactions with ambient baryons, while the probability of AQN–$\mathrm{A\overline{Q}N}$ collisions is entirely negligible.

After recombination the baryon number distribution of the AQNs will essentially be fixed until the present day, but it may develop localized anisotropy in regions of particularly high matter density such as stars or planets.

Key takeaway. Both matter and antimatter AQNs survive from the end of their formation at $T \sim 40\,\mathrm{MeV}$ through BBN, the CMB epoch, and the subsequent stages of structure formation, all the way to the present day, without experiencing any significant mass loss Ge et al. (2019).

4.4 Photon to baryon ratio, η

The baryon-to-photon ratio $\eta \equiv n_{\rm baryon}/n_{\rm photon}$ is measured independently by BBN Cooke et al. (2018) and the CMB Collaboration (2020). The respective constraints are:

$$\begin{aligned} \eta_{\rm BBN} &\simeq 6.0 \times 10^{-10} \\ \eta_{\rm CMB} &\simeq 6.1 \times 10^{-10}. \end{aligned}$$

The agreement between the two measurements constitutes a remarkable success of Big-Bang cosmology. It also places a strong constraint on any entropy injection (i.e. changes in the photon number) occurring between BBN and recombination, which cannot exceed $\delta n_\gamma/n_\gamma \sim 5\%$ at the 2σ level. This constraint is consistent with the QCD-AQN framework (see 4.3).

Within the standard Big-Bang picture, however, the origin of the observed value of η remains unexplained. Using the well-known cross-sections for baryon–antibaryon annihilation, the freeze-out temperature is estimated to be of order $T_{p\bar{p}} \sim 20\,\mathrm{MeV}$[16], yielding the prediction $\eta \sim 10^{-20}$, which fails both to reproduce the observed baryon asymmetry and to account for the absence of large quantities of antimatter in the Universe Kolb and Turner (1990). Hence, numerous scenarios have been proposed to account for the baryon asymmetry and the observed value of η. Many of these invoke physics beyond the Standard Model of particle physics, frequently associated with CP violation at the electroweak symmetry-breaking scale.

In the QCD–AQN framework, primordial photons arise from the same thermal processes that operate in the standard hot Big-Bang scenario. At temperatures well above the QCD scale, the Universe is filled with a dense, strongly interacting plasma in thermal equilibrium. Photons are continuously produced and absorbed through rapid pair annihilations, thereby maintaining a blackbody radiation field.

During the QCD epoch, when axion domain walls collapse, a large fraction of baryon– antibaryon pairs continue to annihilate. These annihilations predominantly produce pions, with neutral pions subsequently decaying into photons (e.g. $\pi^0 \to \gamma\gamma$). However, since this takes place at temperatures of order $T \sim 100$–$200\,\mathrm{MeV}$, the interaction rates are extremely high, and the injected electromagnetic energy thermalises very efficiently. The net effect is not a distortion of the photon spectrum, but rather a redistribution of energy between matter and radiation.

Baryon–antibaryon annihilation ceases when AQN formation ends at $T \sim T_{\mathrm{form}}$, as there are no longer free antibaryons available to annihilate Zhitnitsky (2003). The AQN core becomes sequestered from the surrounding plasma. Meanwhile, the baryons that were not sequestered into matter AQNs remain as free particles in a plasma devoid of antibaryons. The resulting baryon–to– photon ratio is then determined by a Boltzmann suppression factor,

$$\eta \sim e^{-m_p/T_{\mathrm{form}}}, \tag{26}$$

where T_{form} corresponds to the binding-energy scale of the colour superconducting phase inside the aggregate. For $\eta \simeq 6.0 \times 10^{-10}$, it yields

$$T_{\mathrm{form}} \approx 40\,\mathrm{MeV},$$

which is of the same order as the results quoted in 4.1.

Key takeaways. The QCD-AQN framework provides a physical motivation for $\eta \sim 10^{-10}$ without invoking fine-tuning or introducing new baryon-number–violating physics.

4.5 Primordial ^{7}Li abundance

There is a discrepancy between the primordial abundance of ^{7}Li predicted by standard BBN and that inferred from observations of old, metal-poor halo stars. Using the baryon density precisely determined from CMB measurements, standard BBN predicts a primordial abundance of $^7\mathrm{Li/H} \simeq (4\text{–}5) \times 10^{-10}$. In contrast, spectroscopic observations of warm Population II stars consistently find a significantly lower and nearly constant abundance, $^7\mathrm{Li/H} \simeq (1\text{–}2) \times 10^{-10}$. Meanwhile, the predicted abundances of other light elements, notably deuterium and ^{4}He, are in good agreement with observations. Proposed resolutions broadly fall into three categories: astrophysical solutions involving lithium depletion in stellar interiors, nuclear physics solutions

[16]This corresponds to the temperature when the $p-\bar{p}$ collision rate drops below the Hubble expansion rate

invoking unaccounted-for reaction channels during BBN, and new-physics solutions that modify early-Universe conditions, such as late-time energy injection or non-standard particle content. To date, none of these explanations has achieved broad consensus.

In the QCD–AQN framework, antimatter is sequestered into AQNs prior to BBN and does not participate in nuclear reactions during this epoch. AQNs are non-relativistic and extremely rare, and consequently make a negligible contribution to the radiation density. They do not affect the cosmic expansion rate or the effective number of relativistic species, $N_{\rm eff}$. Energy injection from AQNs during BBN is likewise negligible, leading to no significant photodissociation of light nuclei.

Under these conditions, BBN might proceed with a free baryon-to-photon ratio that is lower than the value inferred at later times from the CMB. This selective reduction primarily impacts the synthesis of lithium. Flambaum and Zhitnitsky (2019) showed that the relative depletion of nuclei – quantified by the number of trapped and captured ions of atomic number Z – can be expressed as

$$\frac{\delta n_Z}{n_Z} \simeq \frac{4\pi R_{\rm cap}^3}{3}\, n_{\rm AQN}\, \exp\!\left[\frac{(Z-1)\,\alpha\, Q(r)}{r\,T}\right], \tag{27}$$

where $(4\pi R_{\rm cap}^3/3)\, n_{\rm AQN}$ represents the effective geometrical capture volume associated with the presence of AQNs. For deuterium and helium, this expression yields $\delta n/n \ll 1$, indicating that their primordial abundances remain essentially unchanged, in agreement with observational constraints. In contrast, for lithium ($Z = 3$) one finds $\delta n/n \sim 1$, implying a significant depletion. The depletation is amplified by the fact that most primordial ^{7}Li is initially synthesised in the form of ^{7}Be, for which the depletion factor is even larger.

Key takeway. The QCD-AQN framework may offer a plausible explanation for the ^{7}Li discrepancy.

4.6 AQN mass distribution

The AQN formation process yields a distribution of masses which cannot be precisely computed from first-principles QCD, for several reasons.

(i) AQNs formation is a highly non-linear, out-of-equilibrium process involving axion domain wall formation, collapse, and baryon number accretion in an expanding cosmological background. QCD at finite temperature and finite baryon chemical potential in this regime is intrinsically non-perturbative and cannot be solved analytically.

(ii) The relevant scales span many orders of magnitude: microscopic QCD dynamics ($\Lambda_{\rm QCD}^{-1}$) must be coupled to the axion scale m_a^{-1} and the macroscopic horizon-scale correlations set by the axion field. This multi-scale problem is beyond current lattice QCD capabilities.

(iii) The final AQN mass depends on stochastic properties of the axion domain wall network (correlation length, percolation, collapse time), which are determined by cosmological initial conditions rather than by QCD microphysics.

In other words, QCD fixes the characteristic density and stability properties of the AQNs but it does not allow a prediction of the AQN mass distribution. From a theoretical standpoint, only an order-of-magnitude estimate can be obtained.

4.6.1 AQN mass range at formation freeze-out

Since the mass density of the AQN core is comparable to nuclear density[17], the AQN mass function is directly determined by the AQN size distribution, i.e. the baryon number distribution.

[17]The mass density of quark matter in the CS phase slightly exceeds nuclear density, $\rho_{\rm CS} \simeq (2\text{–}5)\rho_{\rm nucl}$ Alford et al. (2008).

- **Characteristic baryon number and radius**

The size of an AQN is set by the initial size of the collapsing $N_{DW} = 1$ domain walls from which it originates which, in turn, is set by the defect correlation length $\xi_{\rm DW}$, which scales inversely with the axion mass, $\xi_{\rm DW} \sim m_a^{-1}$ Vachaspati and Vilenkin (1984). The evolution of $\xi_{\rm DW}(T) \sim m_a^{-1}(T)$ from $T_{\rm osc} \sim 1\,$GeV to $T_c \sim 170\,$MeV was computed in Ge et al. (2019) on the basis of detailed modelling rather than purely analytical arguments. For $m_a \sim 10^{-4}\,$eV, the correlation length of DW is $\xi_{\rm DW} \sim 0.1{-}1\,$cm, which is much smaller than the horizon size at QCD transition ($\sim 10\,$km) but much larger than the QCD physical scale, $\Lambda_{\rm QCD}^{-1}$ ~fm.

As we saw in Section 4.1, the formation of AQNs follows a sequence of damped oscillations of axion domain walls. Each collapsing domain-wall bubble undergoes radial oscillations whose amplitude gradually decreases due to friction. This friction arises from several thermal and dynamical processes related to the QCD scale : proton–antiproton annihilation within the core, thermal exchange with the surrounding QG plasma, pressure differences between the interior and exterior, and repeated "refill" events in which baryons leave and re-enter the system. As the oscillation proceeds, the chemical potential μ of the AQN core builds up with a definite sign $B > 0$ or $B < 0$. This growing chemical potential causes the equilibrium radius to shrink until the oscillation damps around a final radius $R_{\rm form}$ (see Fig. 21).

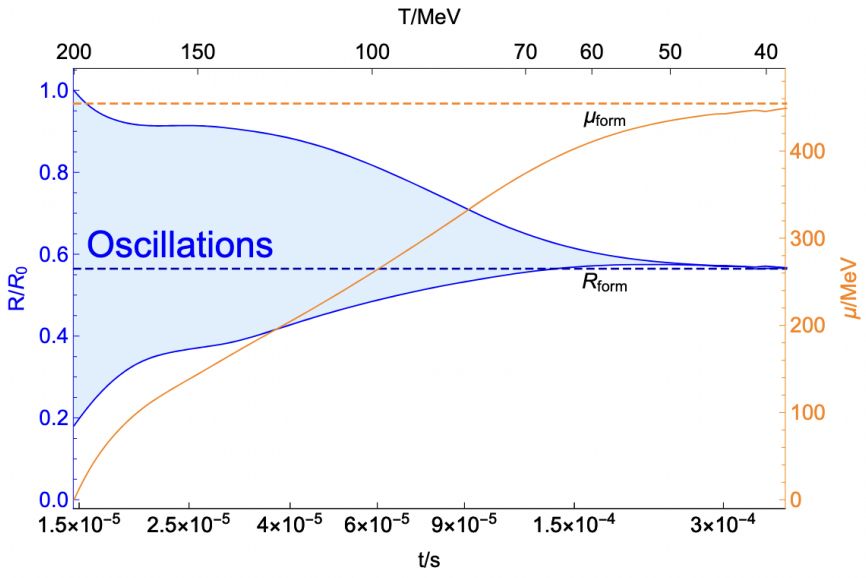


Figure 21: Evolution of the AQN radius, expressed as a fraction of the inital radius R_0, between 200 MeV and 40 Mev. Matter AQNs and antimatter AQNs complete their formation at $\sim$ 40 MeV. The solid orange line represents the lower envelope of the μ oscillation. It reaches $\mu_{\rm form} \sim 450\,$MeV, consistent with formation of a CS phaseGe et al. (2019); Zhitnitsky (2021).

The characteristic AQN mass is set by the number of oscillation cycles occurring as the temperature decreases from $T \sim 170\,$MeV to $T \sim 40\,$MeV , which is of order $\sim 10^7$. When the AQN formation ends at $t \sim 10^{-4}\,$s ($T \sim 40\,$MeV), the typical baryon number is determined by:

$$|B| \sim 4\pi\xi_{\rm DW}^2 \times \Lambda_{\rm QCD}^{-1} \times \rho_{\rm nucl} \times m_p^{-1} \sim 10^{24} \tag{28}$$

where $4\pi\xi_{\rm DW}^2$ is the surface area of the axion domain wall, ($\Lambda_{\rm QCD}^{-1} \times \rho_{\rm nucl}$) the surface mass density of the region in which baryon-charge separation occurs[18], and m_p the proton mass.

[18]This estimate is based on the "thin-wall" approximation which was used in AQN formation papers. The wall can

Eq. (28) yields $|B| \sim 10^{24}$, which corresponds to a typical CS core of size $R_{\rm AQN} \sim 10^{-5}$ cm and a mass of the order of gram.

- **Mass lower bound**

The theoretical lower bound arises from AQN cosmological survival. During their formation, AQNs must withstand thermal evaporation, annihilation with ambient baryons, and diffusion across the axion domain wall before baryon exchange freezes out at $T_{\rm form} \sim 40$ MeV. If the baryon number is too small, surface effects dominate over bulk binding, leading to efficient evaporation and eventual destruction. Some AQNs do not have time to grow, either because they started their formation not very long before $T \sim T_{\rm form}$ or because they started to grow in a small domain wall, or both. As a consequence, they cannot reach the nominal value $\mu \sim 450$ MeV as shown on Fig. 21, and do not survive. Detailed analysis based on the axion domain wall size distribution and the AQN formation growth by Zhitnitsky (2006) indicate a minimum baryon number of order $|B|_{\rm min} \sim 10^{22} - 10^{23}$, corresponding to a mass $m_{\rm min} \sim 10^{-2} - 10^{-1}$ g.

- **Mass upper bound**

The theoretical upper bound arises from the fact that the domain walls size distribution is exponentially supressed at large scale and that the formation time for AQNs is limited. Together, these two limitations lead to an upper bound $|B|_{\rm max} \sim 10^{28}$ Zhitnitsky (2006).

Hence $|B| \sim 10^{22}$–10^{28}, with the precise distribution depending on the axion mass m_a and the details of the collapse process. Converting to mass through $m \simeq m_p B$, this corresponds to a formation mass range of approximately

$$m_{AQN} \sim 10^{-2}\text{–}10^{4}\,{\rm g} \tag{29}$$

4.6.2 A mass distribution constrained by observations

The mass distribution of AQNs is driven by the combination of the following constraints:
(i) The axion domain wall size, R, follows a Gaussian distribution $\propto \exp(-(R/\xi_{\rm DW})^2)$
(ii) AQN formation is active during the period $T \simeq [200 - 40]$ MeV.
Taken together, these two considerations lead to a power law AQN mass distribution:

$$f(m_{\rm AQN}) \propto m_{\rm AQN}^{-\alpha}, \tag{30}$$

which is bounded by the theoretical $[m_{\rm min}, m_{\rm max}] \simeq [10^{-2}, 10^{4}]$g limits given above.

A$\overline{\rm Q}$Ns mass constraints from observations have been discussed in Section 3. They are generally given in terms of the mean A$\overline{\rm Q}$Ns mass, $\langle m_{\rm A\overline{Q}Ns}\rangle$:

$$\langle m_{\rm A\overline{Q}Ns}\rangle = \int_{m_{\rm min}}^{m_{\rm max}} {\rm d}m_{\rm A\overline{Q}Ns}\, m_{\rm A\overline{Q}Ns}\, f(m_{\rm A\overline{Q}Ns}),$$

These observational constraints were summarised in (3.5.5): they are within the $[10^{-2}, 10^{4}]$g theoretical limits.

The value of α cannot be predicted from first principles, but it can be confronted to observations. To calculate the amount of energy injected in the Solar corona, Raza et al. (2018) assumed the power law given by Eq.(30) with a mass range $m_{\rm A\overline{Q}N} \in [10^{-2}, 10^{4}]$ g, which corresponds to a characteristic value $|B| \sim 10^{25}$. The mean A$\overline{\rm Q}$N mass depends on the full distribution, while the annihilation events rate is controlled by the number density of A$\overline{\rm Q}$Ns. By comparison with the

be much thicker, but in that case the baryon are also diluted such that Eq.(28) still holds.

Observation	Common overinterpretation	What is actually constrained
Bullet Cluster	Proof of collisionless particle DM	Low self-interaction cross section per unit mass (σ/m) at large scales; microscopic nature not specified
CMB acoustic peaks	Requires non-baryonic particle DM	Cold, pressureless component before recombination; negligible photon coupling
Large-scale structures	Confirms cold particle DM	Collisionless gravitational clustering
Direct-detection null results	Strong constraints on particle DM	Specific scattering cross sections; does not exclude macroscopic DM

Table 6: Observations often interpreted as evidence for elementary particle dark matter. The final column lists the actual physical quantities constrained.

observed statistics of nanoflares in the corona, the authors show that the data are consistent with an A$\overline{\text{Q}}$N mass function with $\alpha \sim 2$, for which the energy contribution per logarithmic interval of mass is approximately constant. For a typical A$\overline{\text{Q}}$N window $10^{23} \lesssim |B| \lesssim 10^{28}$, the broadly viable region is approximately

$$1 \lesssim \alpha \lesssim 2.5.$$

This analysis does not provide a strong constraint on either the slope α or the mean A$\overline{\text{Q}}$N mass, because all A$\overline{\text{Q}}$Ns are expected to annihilate once they reach an altitude of about $\sim 2000\,\text{km}$ above the photosphere, independently of the assumed slope of the mass distribution. The allowed parameter space is therefore characterised by a wide mass interval, with a typical average mass of order ~ 10 grams, but with significant uncertainty in the precise form of the distribution. This uncertainty mainly reflects the fact that the formation and growth of AQNs take place during the QCD epoch, in a strongly coupled and non-perturbative regime, where the microphysical evolution of closed domain walls and the accumulation of baryon number cannot presently be calculated from first principles.

4.7 Two inflation scenarios

The spatial structure of the domain walls responsible for AQN formation depends on whether Pecci-Quinn symmetry breaking occurs before or after inflation, leading to a different domain-wall topology.

- **Pre-inflation scenario**

Here, since the axion field across the observable Universe is homogenised by inflation, the matter–antimatter asymmetry arises naturally from AQN formation through baryon-charge separation. All free baryons ($B = 1$) are leftover baryons from AQN formation. Therefore $\Omega_{\text{DM}} \sim \Omega_b$ with **no need for baryogenesis.**

- **Post-inflation scenario**

Here the sign of θ_i is random in each causal horizon volume. At PQ symmetry breaking, the Universe is composed of large domains where $\theta_i > 0$ or $\theta_i < 0$. Hence, adopting the formation scenario described in (4.1), the Universe is a mosaic of regions dominated by AQNs with leftover antibaryons, and regions dominated by A$\overline{\text{Q}}$Ns with leftover baryons. In each of these regions, baryon number conservation implies that

$$B_{\text{universe}} = B_{\text{visible}} + B_{\text{AQN}} + \bar{B}_{\text{A}\overline{\text{Q}}\text{N}} = 0.$$

The relation $\Omega_{\rm DM} \sim \Omega_b$ applies both locally within each domain, and globally. There, a conventional baryogenesis may be required.

4.8 Broadening the dark-matter paradigm

Over the past four decades, DM as an elementary particle has emerged as the prevailing paradigm for a combination of theoretical, phenomenological, and experimental reasons. Extensions of the Standard Model of particle physics – such as supersymmetry or hidden-sector frameworks – predict new stable particles, making it economical to associate one of them with DM. The so-called "WIMP miracle" further reinforced this idea: a weak-scale particle with typical electroweak interactions yields the observed relic abundance through thermal freeze-out. In parallel, cold, collisionless particle DM provides an excellent fit to large-scale structure formation and the CMB acoustic peaks. Moreover, particle DM candidates opened the possibility of laboratory detection through direct searches, indirect signals, or collider production.

Over time, the search for elementary particle DM generated considerable sociological momentum, occasionally leading to inherent overinterpretations of some observational evidence. Selected examples are summarised in Table 6. But today broadening the DM paradigm is not a matter of debating astronomical observations: The fundamental question is whether an alternative DM framework can offer an appeal comparable to that of elementary particle candidates. As an illustration, Table 7 contrasts the QCD–AQN framework with the WIMP paradigm.

After several decades of sustained experimental efforts to detect WIMPs without definitive success, the time may be ripe to encourage a more diversified theoretical landscape. As shown in Table 2, one compelling direction is axion physics, the topic of our next section.

5 The QCD axion

The QCD axion[19] and the QCD-AQN framework both originate from the same well-motivated extension of the Standard Model: the Peccei–Quinn solution to the strong CP problem. Yet they represent distinct dark matter candidates.

Axions are ultralight bosons. Their interactions are extremely weak but non-zero, allowing them to evade laboratory detection, while astrophysical and cosmological observations already place strong constraints on the allowed mass range. The axion remains experimentally testable.

In contrast, AQNs are rare macroscopic composite objects. Their interactions with ordinary matter are infrequent but not negligible, occurring primarily through baryon annihilation at their surface, allowing them to evade conventional particle DM searches while remaining astrophysically testable.

Axions are formed during the PQ symmetry breaking ($T \sim f_a \sim 10^9$-10^{12} GeV) while AQNs are formed during the QCD transition (170 MeV $\gtrsim T \gtrsim$ 40 MeV) (see 4.1). The misalignment mechanism is central to both the axion-field dynamics and the baryon-charge separation in the AQN framework (Fig. 22). The key difference is that AQN formation additionally requires the coupling of domain walls with η' mesons.

Both DM candidates behave as cold, collisionless DM without requiring fine-tuned annihilation cross-sections. They cluster gravitationally, do not disrupt BBN, leave the CMB moslty unaffected, and reproduce the observed large-scale structure.

Axions couple to photons, nucleons, and electrons in well-defined ways set by QCD. The coupling to photons is given by

$$\mathcal{L}_{a\gamma\gamma} = -\frac{1}{4}\, g_{a\gamma\gamma}\, a\, F_{\mu\nu} \tilde{F}^{\mu\nu},$$

[19] In this lecture, *axion* refers to the QCD axion, with the DFSZ and KSVZ models serving as the two primary benchmarks. For a review of QCD axions and their cosmological implications, see Marsh (2016).

Aspect	WIMPs (Weakly Interacting Massive Particles)	QCD–AQN Framework
Prior theoretical motivation	Arises in many extensions of the Standard Model (e.g. SUSY, hidden sectors); historically supported by the "WIMP miracle."	Arises as a testable extension of the Standard Model rooted in QCD and axion domain-wall dynamics; no dark sector
Explanatory scope	Explains cosmological DM abundance and structure formation; does not naturally account for the observed coincidence $\Omega_{\rm DM} \sim \Omega_b$ without additional assumptions.	$\Omega_{\rm DM} \sim \Omega_b$ through shared QCD-scale; baryon-to-photon ratio η; possible lithium-7 tension; no baryogenesis if PQ occurs after inflation
Observational evidence	Strong evidence for cold, collisionless DM; but no direct detection.	Behave as cold and effectively collisionless DM. Consistent with cosmological constraints; multiple faint signatures across environments .
Free parameters	At least two parameters (m and σ), often more depending on the specific model.	Dominated by a single macroscopic parameter, $\langle m_{\rm AQN}\rangle$.
Characteristics	Elementary particle; microscopic, weak-scale interactions; small interaction cross section and large number density; mass typically 1 GeV–100 TeV depending on model.	Macroscopic composite objects; gram-scale masses from QCD formation; very small number density; observationally, mean mass $\sim$ 5–200 g .
Stability across cosmic history	Stability is imposed by symmetry (e.g. R-parity, Kaluza–Klein parity).	Stabilised by QCD pressure and axion domain-wall dynamics; macroscopic binding ensures survival from the QCD transition to the present epoch.
Direct detection experiments	LUX-ZEPLIN (LZ), XENONnT, PandaX, SuperCDMS, EDELWEISS, DarkSide, and DEAP-3600. No confirmed direct detection.	No dedicated experiments;
Indirect detection facilities	Fermi Gamma-ray Space Telescope, H.E.S.S., MAGIC, VERITAS, IceCube, ANTARES, AMS-02, and DAMPE	Possible Dark Glow detection with Euclid + JWST + SPT.
Collider searches	Large Hardron Collider: ATLAS and CMS	Not applicable

Table 7: Comparison between the WIMP paradigm and the QCD–AQN framework.

where the axion-photon coupling is

$$g_{a\gamma\gamma} \simeq \frac{\alpha}{2\pi f_a}\,.$$

Since $f_a \sim 10^9$–10^{12} GeV, the axion–photon coupling is extremely suppressed, which yields an axion lifetime

$$\tau_a \gtrsim 10^{25}\,\mathrm{s}$$

much larger than the age of the Universe. Axions and AQNs share a remarkable stability on cosmological timescales.

5.1 QCD axion mass range

The axion mass $m_a \simeq 5.7\,\mu\mathrm{eV}\,(10^{12}\,\mathrm{GeV}/f_a)$ leads to a present day axion relic density parameter Ω_a:

$$\Omega_a h^2 \simeq (0.12)\,\theta_i^2 \left(\frac{f_a}{10^{12}\,\mathrm{GeV}}\right)^{7/6}, \tag{31}$$

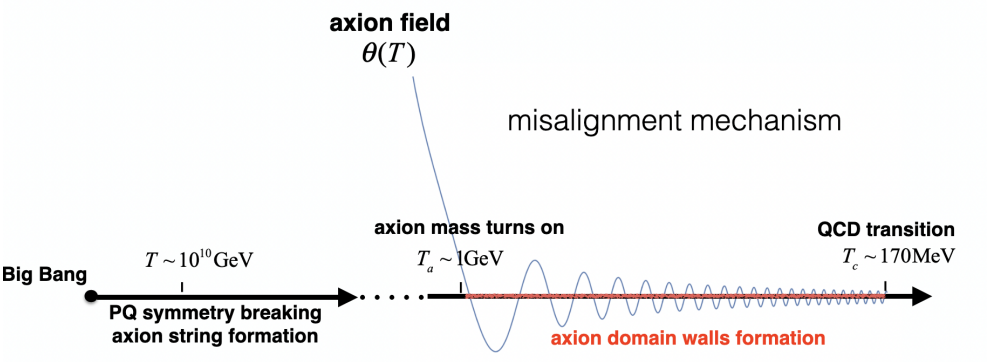


Figure 22: Timeline of axion formation from the Big Bang to the QCD transition.

Source: https://indico.cern.ch/event/707123/contributions/3143173/attachments/1729576/2794761/1_IPA_presentation_Shuailiang_Ge.pdf

where θ_i is the initial misalignment angle. Since $\Omega_{\rm DM}h^2 \simeq 0.12$ today Planck Collaboration et al. (2020), one finds that if the axion is the sole DM component, it saturates dark matter at $m_a \simeq 5.7\,\mu$eV, hence lower masses are excluded for cosmological reasons.

On the other hand, stellar energy-loss arguments, derived from observations of red giants, horizontal-branch stars, white dwarfs, neutron stars and supernova 1987A, impose an upper bound on the axion mass, $m_a \lesssim 10^{-3}\,$eV, depending on the assumed axion couplings. These considerations restinct the broad theoretical window to a mass window spanning

$$m_a \sim 10^{-6}\text{–}10^{-3}\,\text{eV},$$

which still leaves a wide region of parameter space in which AQNs and axions can coexist. The idea that both DM candidates contribute concurrently to the dark matter budget will be discussed in Section 5.5.

5.2 Other types of axions

The QCD axion is sometimes confused with axion-like particles (ALPs) or ultra-light axions (ULAs). To clarify:

- Axion-like particles: ALPs are pseudo-scalar bosons for which the mass m_a and decay constant f_a are not related by the QCD dynamics. They arise generically from the breaking of global symmetries but do not necessarily possess a QCD anomaly and therefore need not couple to the gluon field. ALP cannot solve the strong CP problem. They typically interact very weakly with photons, fermions, or gluons, with couplings suppressed by a large energy scale, and may span a vast mass range, from sub-10^{-22} eV to the eV scale and beyond.

- Ultra-light axions: ULAs are pseudo-scalar fields with extremely small masses, typically $m_a \sim 10^{-22}\,$eV . They are a subset of ALPs with a specific importance in cosmology because of its possible connection with dark energy Hui et al. (2017). ULAs formation via the misalignment mechanism can yield the observed relic abundance for suitable decay constants f_a. Their de Broglie wavelength can be of order kiloparsecs, so that DM behaves as a coherent classical field rather than as individual particles. In this regime, quantum pressure arising from the field gradients counteracts gravitational collapse below a characteristic Jeans scale, thereby suppressing small-scale structure formation.

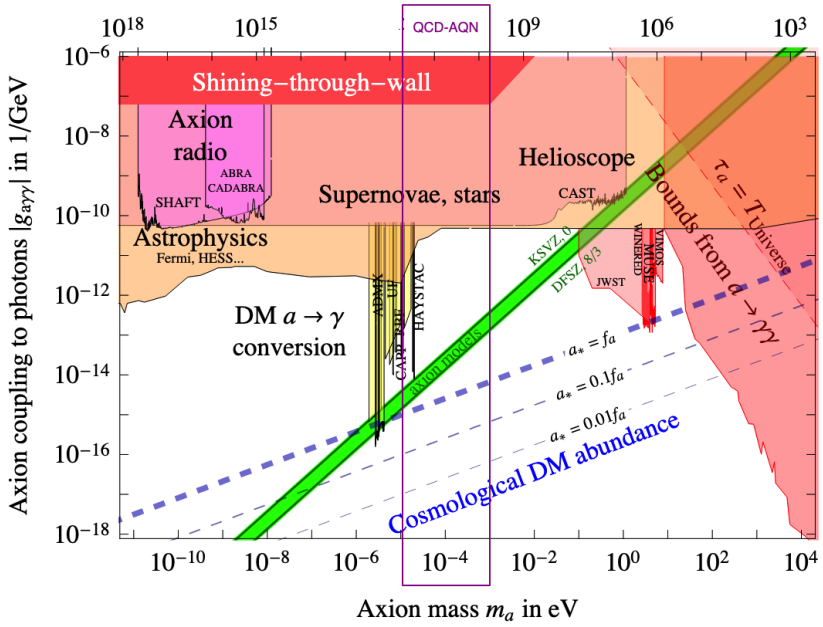


Figure 23: Parameter space for the experimental axion search. Shown are: the range favoured by axion models (green band); the initial axion vacuum expectation value a_* that reproduces the observed DM abundance (blue dashed lines); the exclusion bounds from non-observation of axion decays (coloured regions). The search window compatible with the QCD-AQN framework is the purple rectangle. Adapted from Cirelli et al. (2024)

5.3 Current and upcoming experiments

A broad and rapidly expanding experimental programme is currently underway to search for the QCD axion. The most mature and sensitive searches are haloscope experiments, which aim to detect axions constituting the local Galactic DM halo through their conversion into microwave photons in a resonant cavity permeated by a strong magnetic field. The Axion Dark Matter eXperiment (ADMX) has already reached sensitivity sufficient to probe QCD axions in the mass range $m_a \sim 2-4\,\mu$eV. Next-generation haloscopes, including HAYSTAC, CAPP, ORGAN, and QUAX, are extending coverage to both higher and lower masses using improved cryogenic amplifiers, quantum-limited readout techniques, and novel resonator designs. Looking further ahead, large-scale projects such as MADMAX, based on dielectric haloscopes, aim to explore the higher-mass regime ($m_a \sim 40$–$400\,\mu$eV).

Complementary approaches target axions produced in astrophysical or laboratory environments. Helioscope experiments search for axions emitted by the Sun via their conversion into X-rays in strong laboratory magnetic fields. The CERN Axion Solar Telescope (CAST) has provided leading constraints on axion–photon couplings, while the next-generation International Axion Observatory (IAXO) is expected to improve sensitivity by more than an order of magnitude, probing deeply into the QCD axion parameter space. Laboratory-based "light-shining-through-a-wall" experiments, such as ALPS II, provide purely terrestrial tests of axion–photon conversion, independent of cosmological assumptions.

Axions can also be probed through their couplings to nuclear spins and electrons. Experiments such as CASPEr exploit nuclear magnetic resonance techniques to search for axion-induced oscillating electric dipole moments Jackson Kimball et al. (2017), while QUAX and related setups target axion–electron couplings using magnetic resonance in solid-state systems.

So far, most axion detection efforts have focused on the $m_a \sim 10^{-6} - 10^{-5}$ eV window (see Fig. 23).

5.4 The importance of inflation in axion cosmology

The cosmological implications of the QCD axion depend on whether Peccei–Quinn symmetry breaking occurred before or after cosmic inflation. The epoch of the breaking remains unknown, as it depends on the PQ energy scale, which is not determined by the theory and is not yet constrained by observations. The two scenarios must hence be explored; they correspond to distinct cosmological histories for the axion field and lead to different phenomenological predictions. In particular, we will focus on two aspects: the allowed axion mass range and the upper bound on the inflationary energy scale, H_I.

5.4.1 Axion mass and inflation

The key parameter controlling the axion abundance is the initial misalignment angle:

$$\theta_i = a_i/f_a$$

If PQ symmetry breaks before inflation, θ_i is homogeneous across the observable Universe, whereas if PQ symmetry breaks after inflation, it varies randomly between causally disconnected regions.

- **If PQ symmetry breaks before inflation**

In this case, the subsequent exponential expansion stretches a single causal region to encompass the entire observable Universe. As a result, the axion field takes a single, perfectly homogeneous value across our entire cosmological horizon. The relic axion abundance, Ω_a, then depends on this unique θ_i and on f_a.

In this pre-inflation scenario, cosmological observations impose strong constraints. During inflation, quantum fluctuations of any light scalar field are generated with an amplitude proportional to the inflationary Hubble scale, H_I. If the axion exists during inflation, these fluctuations produce spatial variations in the axion field that translate into fluctuations in the DM density. Such perturbations correspond to isocurvature modes, which are distinct from the adiabatic perturbations observed in the CMB. Observations show that the primordial perturbations are almost entirely adiabatic, placing tight limits on any isocurvature component.

Here the axion mass is only weakly theoretically constrained and may lie within the broad theoretical window set by the decay-constant range

$$10^{-10}\,\mathrm{eV} \lesssim m_a \lesssim 10^{-2}\,\mathrm{eV}.$$

with the caveat that the actual viable region depends on θ_i and H_I, as illustrated in Fig. 24.

- **If PQ symmetry breaks after inflation**

A different cosmological history arises in the post-inflation scenario. In this case, inflation does not homogenise the axion field across the observable Universe. Instead, θ_i takes different values in different causal regions. The axion field therefore becomes a spatially varying quantity whose initial value is effectively random from one horizon volume to another. When the PQ symmetry breaks, the network of global axion strings that forms eventually decays, producing additional axions that contributes to Ω_a, potentially overclosing the Universe if the axion is too light.

Early simulations suggested a narrow mass range around $m_a \sim 10^{-5}$–$10^{-4}\,\mathrm{eV}$. However, significant progress in large-scale simulations has shown that the predicted mass range depends sensitively on the axion radiation spectrum emitted by the string network and on the dynamics

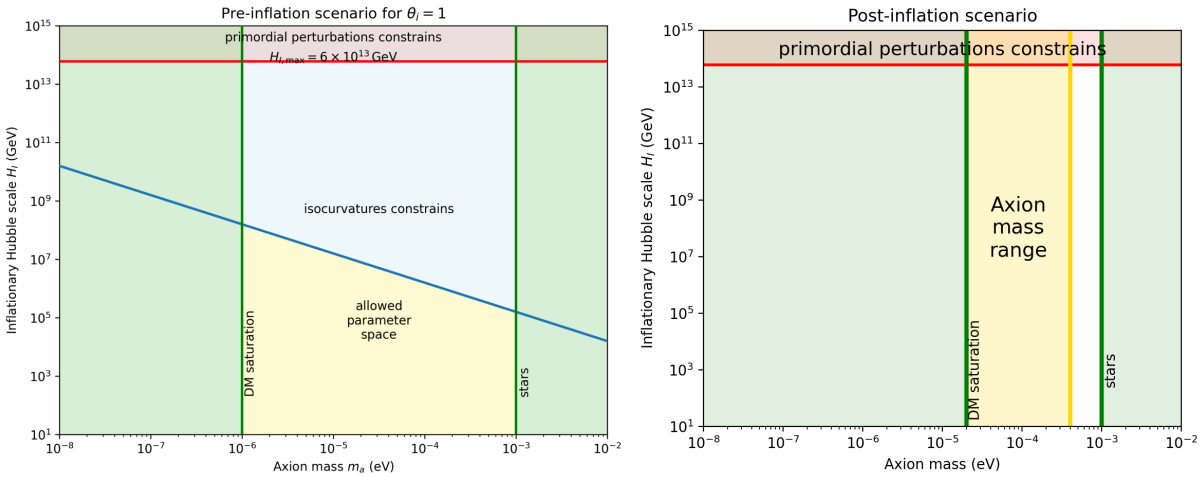


Figure 24: Inflationary Hubble scale H_I vs axion mass m_a for the pre- and post-inflation scenarios. The allowed parameter space is highlighted in yellow. Left: pre-inflation scenario (for $\theta_i = 1$, $\Omega_{\rm DM} = \Omega_a$), showing constraints on H_I from isocurvatures observations, DM saturation and stellar energy loss arguments. Right: post-inflation scenario with its narrow axion mass range.

of the final string collapse. Large lattice simulations performed by Saikawa et al. (2024) emphasised previously underestimated systematic effects, including sensitivity to initial conditions and discretisation artefacts. Their analysis favours a comparatively high axion mass range

$$m_a \simeq 95\text{–}450\ \mu\text{eV}.$$

Recent work has clarified that the dominant uncertainty in the post-inflation prediction is not the zero-temperature equation (Eq.21a) but rather the real-time dynamics of cosmic strings during the QCD transition. Taking current numerical uncertainties into account, the axion mass lies in the approximate range

$$m_a \sim 25\text{–}400\ \mu\text{eV}.$$

Several key characteristics of the two scenarios are contrasted in Table 8.

5.4.2 Inflationary Hubble scale upper bound

The current observational upper bound on H_I is derived from limits on the tensor-to-scalar ratio of primordial perturbations, r, measured in the CMB. Current data constrain this ratio to $r < 0.032$ at 95% confidence Tristram et al. (2022), which translates into:

$$H_I \simeq (10^{14}\,\text{GeV})\sqrt{\frac{r}{0.01}} \lesssim 6 \times 10^{13}\,\text{GeV} \tag{32}$$

- **In the pre-inflation scenario**

  H_I must also be sufficiently small to prevent excessive axion isocurvature fluctuations $\delta a \sim \frac{H_I}{2\pi}$. In this case, CMB observations lead to a much tighter upper bound on H_I:

$$H_I \lesssim (1.6 \times 10^7\,\text{GeV})\,\theta_i \left(\frac{10\,\mu\text{eV}}{m_a}\right)\frac{\Omega_{\rm DM}}{\Omega_a}. \tag{33}$$

  Assuming $\Omega_{\rm DM} = \Omega_a$, this does not lead to an observational conflict with (Eq. 32) (see Fig. 24).

  Several inflation models are considered theoretically unattractive if H_I is forced to be very low, as this typically requires a more finely tuned inflaton potential and can complicate

Aspect	PQ breaking **before inflation**	PQ breaking **after inflation**
Theoretical f_a parameter space	Large: $10^9 \lesssim f_a \lesssim 10^{12}$ GeV (model dependent)	Small: $10^{11} \lesssim f_a \lesssim 10^{12}$ GeV
θ_i	$-\pi \leq \theta_i \leq \pi$	Random variable with $\langle \theta_i^2 \rangle = \frac{\pi^2}{3}$.
Axion mass for DM saturation	$m_a \sim 10^{-6}$ eV	$m_a = 25.2 \pm 11.0$ eV; $m_a \simeq$ 95–450 μeV Saikawa et al. (2024)

Table 8: Comparison of pre- and post-inflation scenarios aspects Buschmann et al. (2020).

the reheating process after inflation. It also strongly suppresses primordial tensor modes, eliminating the possibility of detecting inflationary gravitational waves (and B-modes in the CMB). For these reasons, some model builders favour an axion mass in the μeV range.

A growing body of literature discusses mechanisms capable of relaxing the isocurvature constraint, e.g. Beltrán et al. (2007); Graham and Racco (2025). The effective axion decay constant during inflation, $f_a^{\rm eff}$, may be substantially larger than the QCD epoch value f_a, such that at the end of the inflationary era, f_a could reach lower values consistent with a high m_a, without generating significant isocurvature fluctuations. The main conclusion is that a relatively large present-day m_a does not preclude the detection of primordial B-modes and remains compatible with a high H_I. However, for such a large axion mass, Ω_a cannot account for the entirety of $\Omega_{\rm DM}$ (Eq.31). Nothing in principle prevents the ratio $\Omega_a/\Omega_{\rm DM}$ from evolving at early times. This is consistent with the AQN formation scenario, as we shall see in (5.5), where AQNs can co-exist with QCD axions.

- **In the post-inflation scenario**

  The axion field does not exist as a physical degree of freedom during inflation, and therefore inflationary fluctuations do not generate axion isocurvature perturbations. The CMB constraints on isocurvature modes do not apply.

Appart from the upper bounds described above, the inflationary Hubble scale H_I remains unconstrained observationally, and current data do not require inflation to occur at a high energy scale.

5.5 Dark matter as a two-component system

Some critics of the QCD axion argue that the model has become overly focused on the narrow mass range around $m_a \sim 10^{-6}$ eV. This region has been the target of several experiments, yet no confirmed detection has emerged. The same authors claim that the parameter space has been repeatedly probed without success and that the continued emphasis on this range reflects theoretical bias. Exploring much broader mass ranges often implies that axions would constitute only a fraction of the dark matter rather than its entirety, which departs from the conventional approach of constructing DM models that account for the full DM abundance.

The QCD-AQN framework provides a strong motivation for exploring the region $m_a \gtrsim \mu$eV, regardless of the time when PQ breaking occurs. The formation of AQNs is accompanied by the generation of a residual population of free QCD axions:

$$\Omega_{\rm DM} = \Omega_{\rm a} + \Omega_{\rm A\underline{Q}N} + \Omega_{\rm A\overline{Q}N}$$

where both AQN components are generated at the QCD epoch, while the axion mass turns on at ~ 1 GeV and spans a wide interval:

$$10^{-5} \lesssim m_a \lesssim 10^{-3}\,\text{eV},$$

compatible with cosmology and AQN formation.

Ge et al. (2018) perform quantitative calculations of the relative abundances of axions, AQNs, and left over baryons. They show that AQNs would constitute the dominant component of dark matter[20]:

$$\Omega_{\underline{\mathrm{AQN}}} + \Omega_{\overline{\mathrm{AQN}}} \gg \Omega_a .$$

Interestingly, they find that isocurvature perturbations are significantly suppressed even for large values of m_a, which enlarges the allowed parameter space for the inflationary Hubble scale and strengthens the motivation for experimental axion searches across the QCD-AQN window shown in Fig. 23.

In Sections 4 and 5 we examined the ability of QCD to account for dark matter within a theoretically well-motivated framework that does not require extensions of the Standard Model beyond the QCD axion. The purpose of our final section is to illustrate that QCD may offer a conceptually simple, theoretically grounded, and explanatory framework for dark energy.

6 Conclusion

The QCD-AQN framework offers a phenomenologically rich approach to dark matter rooted in QCD dynamics and the Peccei–Quinn mechanism. It links the origin of dark matter to the matter–antimatter asymmetry without introducing an entirely new particle sector beyond the axion, a particle currently being sought by state-of-the-art experiments. It proposes a shift from dark matter as weakly interacting particles to macroscopic, strongly bound aggregates whose interactions with baryonic matter generate observable electromagnetic signatures.

The explanatory scope of QCD-AQN is particularly compelling. It naturally accounts for the observed relation $\Omega_{\mathrm{DM}} \simeq 5\,\Omega_b$ by linking the dark matter abundance directly to baryonic physics at the QCD epoch: dark matter and visible baryons originate from the same QCD-driven dynamics, which also sets the baryon-to-photon ratio $\eta \sim 10^{-10}$. The apparent matter–antimatter asymmetry is reinterpreted as a baryon-charge separation. Furthermore, QCD-AQN may offer new avenues for alleviating the ^{7}Li discrepancy. Several puzzles of early-Universe cosmology are seen as interconnected consequences of QCD-scale physics.

A distinctive feature of the QCD-AQN framework is its multi-channel predictivity: the same macroscopic parameter governing the AQN mass distribution simultaneously affects diffuse Galactic emission and spectral distortions of the CMB, as well as characteristics signature in dense objects, including the Sun and the Earth. Rather than being tuned independently for each phenomenon, these observables emerge from a unified physical mechanism.

The framework is governed by a single free parameter – the mean mass of the AQN mass distribution – which is currently constrained by independent astrophysical considerations to lie in the range $\sim$ 1–100 g. These bounds emerge consistently across multiple, otherwise unrelated observations, with the independently inferred mass windows showing a remarkable degree of agreement with theoretical constrains.

If the upcoming observational tests (511 keV bulge emission, 21 cm emission, cosmic radio background) are successfully passed, or if the predicted dark glow is detected, confidence in the QCD-AQN framework will grow. It would open a new and rich line of investigation, connecting a wide range of well-established areas of physics. Rather than requiring exotic extensions of the Standard Model, QCD-AQN suggests that new phenomena may emerge from known physics operating in unusual regimes. This perspective invites a collective effort to search for observational signatures across many environments. In this sense, the exploration of the QCD-AQN framework may develop into a playful yet rigorous field of research, where discarded sky backgrounds, diffuse emissions, and unexplained excesses become valuable laboratories for testing fundamental

[20] Unless $\Omega_{\mathrm{DM}} \simeq \Omega_a$

physics. Whether AQNs, together with a population of QCD axions, ultimately make up all of the dark matter remains uncertain; nevertheless, the framework provides a compelling illustration of how QCD physics can leave observable imprints in cosmology, possibly extending beyond dark matter to the domain of dark energy.

Acknowledgements

These lecture notes were prepared for Les Houches 2025 Summer School. I am thankful to the organizers for the invitation and for creating such a stimulating scientific environment. I am particularly grateful to Benoîte Pfeiffer for her significant contribution to the writing of this lecture. Her careful reading, insightful comments, and constructive suggestions substantially improved both the clarity and the structure of the material. Her engagement with the subject and thoughtful discussions were invaluable in refining several key arguments and strengthening the overall presentation. I would like to thank Eric Zhitnitsky and Xunyu Liang for our lively and constructive discussions about the AQNs framework since 2017. Students in our AQN group at UBC have contributed significantly to several results presented in this lecture, in particular Shuailiang Ge, Fereshteh Majidi, Egor Peshkov, Nayyer Raza, Ben Scully, Michael Sekatchev, Md Shahriar Rahim Siddiqui, Saloni Soni; it is a pleasure to thank them for their commitment and hard work. Finally, I would like to thank Karim Benabed, Robert Branderberger, Jean-Charles Cuillandre, Bryce Cyr, Cail Daley, Klaus Dolag, Hendrik Hildebrant, Ryley Hill, Gary Hinshaw, Adrian Liu, Jayant Murthy, Douglas Scott, Joe Silk, and Julian Sommer for insightful discussions on specific aspects of this work, which proved particularly helpful when exploring new directions and new tests of the AQN framework. This work was supported by the Natural Sciences and Engineering Research Council of Canada.

References

J. Aalbers, D. S. Akerib, C. W. Akerlof, A. K. Al Musalhi, F. Alder, A. Alqahtani, S. K. Alsum, C. S. Amarasinghe, A. Ames, T. J. Anderson, N. Angelides, H. M. Araújo, J. E. Armstrong, M. Arthurs, S. Azadi, A. J. Bailey, A. Baker, J. Balajthy, S. Balashov, J. Bang, J. W. Bargemann, M. J. Barry, J. Barthel, D. Bauer, A. Baxter, K. Beattie, J. Belle, P. Beltrame, J. Bensinger, T. Benson, E. P. Bernard, A. Bhatti, A. Biekert, T. P. Biesiadzinski, H. J. Birch, B. Birrittella, G. M. Blockinger, K. E. Boast, B. Boxer, R. Bramante, C. A. J. Brew, P. Brás, J. H. Buckley, V. V. Bugaev, S. Burdin, J. K. Busenitz, M. Buuck, R. Cabrita, C. Carels, D. L. Carlsmith, B. Carlson, M. C. Carmona-Benitez, M. Cascella, C. Chan, A. Chawla, H. Chen, J. J. Cherwinka, N. I. Chott, A. Cole, J. Coleman, M. V. Converse, A. Cottle, G. Cox, W. W. Craddock, O. Creaner, D. Curran, A. Currie, J. E. Cutter, C. E. Dahl, A. David, J. Davis, T. J. R. Davison, J. Delgaudio, S. Dey, L. de Viveiros, A. Dobi, J. E. Y. Dobson, E. Druszkiewicz, A. Dushkin, T. K. Edberg, W. R. Edwards, M. M. Elnimr, W. T. Emmet, S. R. Eriksen, C. H. Faham, A. Fan, S. Fayer, N. M. Fearon, S. Fiorucci, H. Flaecher, P. Ford, V. B. Francis, E. D. Fraser, T. Fruth, R. J. Gaitskell, N. J. Gantos, D. Garcia, A. Geffre, V. M. Gehman, J. Genovesi, C. Ghag, R. Gibbons, E. Gibson, M. G. D. Gilchriese, S. Gokhale, B. Gomber, J. Green, A. Greenall, S. Greenwood, M. G. D. van der Grinten, C. B. Gwilliam, C. R. Hall, S. Hans, K. Hanzel, A. Harrison, E. Hartigan-O'Connor, S. J. Haselschwardt, M. A. Hernandez, S. A. Hertel, G. Heuermann, C. Hjemfelt, M. D. Hoff, E. Holtom, J. Y.-K. Hor, M. Horn, D. Q. Huang, D. Hunt, C. M. Ignarra, R. G. Jacobsen, O. Jahangir, R. S. James, S. N. Jeffery, W. Ji, J. Johnson, A. C. Kaboth, A. C. Kamaha, K. Kamdin, V. Kasey, K. Kazkaz, J. Keefner, D. Khaitan, M. Khaleeq, A. Khazov, I. Khurana, Y. D. Kim, C. D. Kocher, D. Kodroff, L. Korley, E. V. Korolkova, J. Kras, H. Kraus, S. Kravitz, H. J. Krebs, L. Kreczko, B. Krikler, V. A. Kudryavtsev, S. Kyre, B. Landerud, E. A. Leason, C. Lee, J. Lee, D. S.

Leonard, R. Leonard, K. T. Lesko, C. Levy, J. Li, F.-T. Liao, J. Liao, J. Lin, A. Lindote, R. Linehan, W. H. Lippincott, R. Liu, X. Liu, Y. Liu, C. Loniewski, M. I. Lopes, E. Lopez Asamar, B. López Paredes, W. Lorenzon, D. Lucero, S. Luitz, J. M. Lyle, P. A. Majewski, J. Makkinje, D. C. Malling, A. Manalaysay, L. Manenti, R. L. Mannino, N. Marangou, M. F. Marzioni, C. Maupin, M. E. McCarthy, C. T. McConnell, D. N. McKinsey, J. McLaughlin, Y. Meng, J. Migneault, E. H. Miller, and E. Mizrachi. First Dark Matter Search Results from the LUX-ZEPLIN (LZ) Experiment. *PRL*, 131(4):041002, July 2023. doi:10.1103/PhysRevLett.131.041002.

C. Abel, S. Afach, N. J. Ayres, C. A. Baker, G. Ban, G. Bison, K. Bodek, V. Bondar, M. Burghoff, E. Chanel, Z. Chowdhuri, P.-J. Chiu, B. Clement, C. B. Crawford, M. Daum, S. Emmenegger, L. Ferraris-Bouchez, M. Fertl, P. Flaux, B. Franke, A. Fratangelo, P. Geltenbort, K. Green, W. C. Griffith, M. van der Grinten, Z. D. Grujić, P. G. Harris, L. Hayen, W. Heil, R. Henneck, V. Hélaine, N. Hild, Z. Hodge, M. Horras, P. Iaydjiev, S. N. Ivanov, M. Kasprzak, Y. Kermaidic, K. Kirch, A. Knecht, P. Knowles, H.-C. Koch, P. A. Koss, S. Komposch, A. Kozela, A. Kraft, J. Krempel, M. Kuźniak, B. Lauss, T. Lefort, Y. Lemière, A. Leredde, P. Mohanmurthy, A. Mtchedlishvili, M. Musgrave, O. Naviliat-Cuncic, D. Pais, F. M. Piegsa, E. Pierre, G. Pignol, C. Plonka-Spehr, P. N. Prashanth, G. Quéméner, M. Rawlik, D. Rebreyend, I. Rienäcker, D. Ries, S. Roccia, G. Rogel, D. Rozpedzik, A. Schnabel, P. Schmidt-Wellenburg, N. Severijns, D. Shiers, R. Tavakoli Dinani, J. A. Thorne, R. Virot, J. Voigt, A. Weis, E. Wursten, G. Wyszynski, J. Zejma, J. Zenner, and G. Zsigmond. Measurement of the Permanent Electric Dipole Moment of the Neutron. *PRL*, 124(8):081803, February 2020. doi:10.1103/PhysRevLett.124.081803.

J. H. Adams, S. Ahmad, J.-N. Albert, D. Allard, L. Anchordoqui, V. Andreev, A. Anzalone, Y. Arai, K. Asano, M. Ave Pernas, P. Baragatti, P. Barrillon, T. Batsch, J. Bayer, R. Bechini, T. Belenguer, R. Bellotti, K. Belov, A. A. Berlind, M. Bertaina, P. L. Biermann, S. Biktemerova, C. Blaksley, N. Blanc, J. Błęcki, S. Blin-Bondil, J. Blümer, P. Bobik, M. Bogomilov, M. Bonamente, M. S. Briggs, S. Briz, A. Bruno, F. Cafagna, D. Campana, J.-N. Capdevielle, R. Caruso, M. Casolino, C. Cassardo, G. Castellini, C. Catalano, O. Catalano, A. Cellino, M. Chikawa, M. J. Christl, D. Cline, V. Connaughton, L. Conti, G. Cordero, H. J. Crawford, R. Cremonini, S. Csorna, S. Dagoret-Campagne, A. J. de Castro, C. De Donato, C. de la Taille, C. De Santis, L. del Peral, A. Dell'Oro, N. De Simone, M. Di Martino, G. Distratis, F. Dulucq, M. Dupieux, A. Ebersoldt, T. Ebisuzaki, R. Engel, S. Falk, K. Fang, F. Fenu, I. Fernández-Gómez, S. Ferrarese, D. Finco, M. Flamini, C. Fornaro, A. Franceschi, J. Fujimoto, M. Fukushima, P. Galeotti, G. Garipov, J. Geary, G. Gelmini, G. Giraudo, M. Gonchar, C. González Alvarado, P. Gorodetzky, F. Guarino, A. Guzmán, Y. Hachisu, B. Harlov, A. Haungs, J. Hernández Carretero, K. Higashide, D. Ikeda, H. Ikeda, N. Inoue, S. Inoue, A. Insolia, F. Isgrò, Y. Itow, E. Joven, E. G. Judd, A. Jung, F. Kajino, T. Kajino, I. Kaneko, Y. Karadzhov, J. Karczmarczyk, M. Karus, K. Katahira, K. Kawai, Y. Kawasaki, B. Keilhauer, B. A. Khrenov, Jeong-Sook Kim, Soon-Wook Kim, Sug-Whan Kim, M. Kleifges, P. A. Klimov, D. Kolev, I. Kreykenbohm, K. Kudela, Y. Kurihara, A. Kusenko, E. Kuznetsov, M. Lacombe, C. Lachaud, J. Lee, J. Licandro, H. Lim, F. López, M. C. Maccarone, K. Mannheim, D. Maravilla, L. Marcelli, A. Marini, O. Martinez, G. Masciantonio, K. Mase, R. Matev, G. Medina-Tanco, T. Mernik, H. Miyamoto, Y. Miyazaki, Y. Mizumoto, G. Modestino, A. Monaco, D. Monnier-Ragaigne, J. A. Morales de los Ríos, C. Moretto, V. S. Morozenko, B. Mot, T. Murakami, M. Nagano, M. Nagata, S. Nagataki, T. Nakamura, T. Napolitano, D. Naumov, R. Nava, A. Neronov, K. Nomoto, T. Nonaka, T. Ogawa, S. Ogio, H. Ohmori, A. V. Olinto, P. Orleański, G. Osteria, M. I. Panasyuk, E. Parizot, I. H. Park, H. W. Park, B. Pastircak, T. Patzak, T. Paul, C. Pennypacker, S. Perez Cano, T. Peter, P. Picozza, T. Pierog, L. W. Piotrowski, S. Piraino, Z. Plebaniak, A. Pollini, P. Prat, G. Prévôt, H. Prieto, M. Putis, P. Reardon, M. Reyes, M. Ricci, I. Rodríguez, M. D. Rodríguez Frías, F. Ronga, M. Roth, H. Rothkaehl, G. Roudil, I. Rusinov, and M. Rybczyński. The JEM-EUSO mission: An introduction. *Experimental Astronomy*, 40(1): 3–17, November 2015. doi:10.1007/s10686-015-9482-x.

Mark Alford, Krishna Rajagopal, and Frank Wilczek. Color-flavor locking and chiral symmetry breaking in high density QCD. *Nuclear Physics B*, 537(1):443–458, January 1999. doi:10.1016/S0550-3213(98)00668-3.

Mark G. Alford, Andreas Schmitt, Krishna Rajagopal, and Thomas Schäfer. Color superconductivity in dense quark matter. *Reviews of Modern Physics*, 80(4):1455–1515, October 2008. doi:10.1103/RevModPhys.80.1455.

ANITA Collaboration, P. W. Gorham, A. Ludwig, C. Deaconu, P. Cao, P. Allison, O. Banerjee, L. Batten, D. Bhattacharya, J. J. Beatty, K. Belov, W. R. Binns, V. Bugaev, C. H. Chen, P. Chen, Y. Chen, J. M. Clem, L. Cremonesi, B. Dailey, P. F. Dowkontt, B. D. Fox, J. W. H. Gordon, C. Hast, B. Hill, S. Y. Hsu, J. J. Huang, K. Hughes, R. Hupe, M. H. Israel, T. C. Liu, L. Macchiarulo, S. Matsuno, K. McBride, C. Miki, J. Nam, C. J. Naudet, R. J. Nichol, A. Novikov, E. Oberla, M. Olmedo, R. Prechelt, S. Prohira, B. F. Rauch, J. M. Roberts, A. Romero-Wolf, B. Rotter, J. W. Russell, D. Saltzberg, D. Seckel, H. Schoorlemmer, J. Shiao, S. Stafford, J. Stockham, M. Stockham, B. Strutt, M. S. Sutherland, G. S. Varner, A. G. Vieregg, S. H. Wang, and S. A. Wissel. Unusual Near-horizon Cosmic-ray-like Events Observed by ANITA-IV. *arXiv e-prints*, art. arXiv:2008.05690, August 2020. doi:10.48550/arXiv.2008.05690.

Howard Baer. TASI 2008 lectures on Collider Signals II: E_T̂missing signatures and the dark matter connection. *arXiv e-prints*, art. arXiv:0901.4732, January 2009. doi:10.48550/arXiv.0901.4732.

L. Balkenhol, D. Dutcher, A. Spurio Mancini, A. Doussot, K. Benabed, S. Galli, P. A. R. Ade, A. J. Anderson, B. Ansarinejad, M. Archipley, A. N. Bender, B. A. Benson, F. Bianchini, L. E. Bleem, F. R. Bouchet, L. Bryant, E. Camphuis, J. E. Carlstrom, T. W. Cecil, C. L. Chang, P. Chaubal, P. M. Chichura, T.-L. Chou, A. Coerver, T. M. Crawford, A. Cukierman, C. Daley, T. de Haan, K. R. Dibert, M. A. Dobbs, W. Everett, C. Feng, K. R. Ferguson, A. Foster, A. E. Gambrel, R. W. Gardner, N. Goeckner-Wald, R. Gualtieri, F. Guidi, S. Guns, N. W. Halverson, E. Hivon, G. P. Holder, W. L. Holzapfel, J. C. Hood, N. Huang, L. Knox, M. Korman, C.-L. Kuo, A. T. Lee, A. E. Lowitz, C. Lu, M. Millea, J. Montgomery, Y. Nakato, T. Natoli, G. I. Noble, V. Novosad, Y. Omori, S. Padin, Z. Pan, P. Paschos, K. Prabhu, W. Quan, M. Rahimi, A. Rahlin, C. L. Reichardt, M. Rouble, J. E. Ruhl, E. Schiappucci, G. Smecher, J. A. Sobrin, A. A. Stark, J. Stephen, A. Suzuki, C. Tandoi, K. L. Thompson, B. Thorne, C. Tucker, C. Umilta, J. D. Vieira, G. Wang, N. Whitehorn, W. L. K. Wu, V. Yefremenko, M. R. Young, J. A. Zebrowski, and SPT-3G Collaboration. Measurement of the CMB temperature power spectrum and constraints on cosmology from the SPT-3G 2018 TT, TE, and EE dataset. *PRD*, 108(2):023510, July 2023. doi:10.1103/PhysRevD.108.023510.

María Beltrán, Juan García-Bellido, and Julien Lesgourgues. Isocurvature bounds on axions revisited. *PRD*, 75(10):103507, May 2007. doi:10.1103/PhysRevD.75.103507.

Gianfranco Bertone and Tim M. P. Tait. A new era in the search for dark matter. *Nature*, 562 (7725):51–56, October 2018. doi:10.1038/s41586-018-0542-z.

C. D. Bochenek, V. Ravi, K. V. Belov, G. Hallinan, J. Kocz, S. R. Kulkarni, and D. L. McKenna. A fast radio burst associated with a Galactic magnetar. *Nature*, 587(7832):59–62, November 2020. doi:10.1038/s41586-020-2872-x.

Kimberly K. Boddy and Vera Gluscevic. First cosmological constraint on the effective theory of dark matter-proton interactions. *PRD*, 98(8):083510, October 2018. doi:10.1103/PhysRevD.98.083510.

Kimberly K. Boddy, Vera Gluscevic, Vivian Poulin, Ely D. Kovetz, Marc Kamionkowski, and Rennan Barkana. Critical assessment of CMB limits on dark matter-baryon scatter-

ing: New treatment of the relative bulk velocity. *PRD*, 98(12):123506, December 2018. doi:10.1103/PhysRevD.98.123506.

Judd D. Bowman, Alan E. E. Rogers, Raul A. Monsalve, Thomas J. Mozdzen, and Nivedita Mahesh. An absorption profile centred at 78 megahertz in the sky-averaged spectrum. *Nature*, 555(7694):67–70, March 2018. doi:10.1038/nature25792.

Malte Buschmann, Joshua W. Foster, and Benjamin R. Safdi. Early-Universe Simulations of the Cosmological Axion. *PRL*, 124(16):161103, April 2020. doi:10.1103/PhysRevLett.124.161103.

F. Caspers, C. M. Adair, K. Altenmüller, V. Anastassopoulos, S. Arguedas Cuendis, J. Baier, K. Barth, A. Belov, D. Bozicevic, H. Bräuninger, G. Cantatore, J. F. Castel, S. A. Çetin, W. Chung, H. Choi, J. Choi, T. Dafni, M. Davenport, A. Dermenev, K. Desch, B. Döbrich, H. Fischer, W. Funk, J. Galan, A. Gardikiotis, S. Gninenko, J. Golm, M. D. Hasinoff, D. H. H. Hoffmann, D. Díez Ibáñez, I. G. Irastorza, K. Jakovčić, J. Kaminski, M. Karuza, C. Krieger, Ç. Kutlu, B. Lakić, J. M. Laurent, J. Lee, S. Lee, G. Luzón, C. Margalejo, M. Maroudas, L. Miceli, H. Mirallas, L. Obis, A. Özbey, K. Özbozduman, M. J. Pivovaroff, M. Rosu, J. Ruz, E. Ruiz-Chóliz, S. Schmidt, Y. K. Semertzidis, S. K. Solanki, L. Stewart, I. Tsagris, T. Vafeiadis, J. K. Vogel, M. Vretenar, S. Youn, A. Zhitnitsky, and K. Zioutas. Daily modulations and broadband strategy in axion searches: An application with the CAST-CAPP detector. *PRD*, 111(8):082009, April 2025. doi:10.1103/PhysRevD.111.082009.

S. Chang, C. Hagmann, and P. Sikivie. Studies of the motion and decay of axion walls bounded by strings. *PRD*, 59(2):023505, December 1998. doi:10.1103/PhysRevD.59.023505.

Marco Cirelli, Alessandro Strumia, and Jure Zupan. Dark Matter. *arXiv e-prints*, art. arXiv:2406.01705, June 2024. doi:10.48550/arXiv.2406.01705.

Planck Collaboration. Planck 2018 results. vi. cosmological parameters. *Astron. Astrophys.*, 641: A6, 2020. doi:10.1051/0004-6361/201833910.

Ryan J. Cooke, Max Pettini, and Charles C. Steidel. One percent determination of the primordial deuterium abundance. *Astrophys. J.*, 855:102, 2018. doi:10.3847/1538-4357/aaab53.

J.-C. Cuillandre, M. Bolzonella, A. Boselli, F. R. Marleau, M. Mondelin, J. G. Sorce, C. Stone, F. Buitrago, Michele Cantiello, K. George, N. A. Hatch, L. Quilley, F. Mannucci, T. Saifollahi, R. Sánchez-Janssen, F. Tarsitano, C. Tortora, X. Xu, H. Bouy, S. Gwyn, M. Kluge, A. Lançon, R. Laureijs, M. Schirmer, Abdurro'uf, P. Awad, M. Baes, F. Bournaud, D. Carollo, S. Codis, C. J. Conselice, V. De Lapparent, P.-A. Duc, A. Ferré-Mateu, W. Gillard, J. B. Golden-Marx, P. Jablonka, R. Habas, L. K. Hunt, S. Mei, M.-A. Miville-Deschênes, M. Montes, A. Nersesian, R. F. Peletier, M. Poulain, R. Scaramella, M. Scialpi, E. Sola, J. Stephan, L. Ulivi, M. Urbano, R. Zöller, N. Aghanim, B. Altieri, A. Amara, S. Andreon, N. Auricchio, M. Baldi, A. Balestra, S. Bardelli, R. Bender, A. Biviano, C. Bodendorf, D. Bonino, E. Branchini, M. Brescia, J. Brinchmann, S. Camera, V. Capobianco, C. Carbone, J. Carretero, S. Casas, F. J. Castander, M. Castellano, G. Castignani, S. Cavuoti, A. Cimatti, G. Congedo, L. Conversi, Y. Copin, F. Courbin, H. M. Courtois, M. Cropper, A. Da Silva, H. Degaudenzi, G. De Lucia, A. M. Di Giorgio, J. Dinis, M. Douspis, F. Dubath, C. A. J. Duncan, X. Dupac, S. Dusini, M. Farina, S. Farrens, S. Ferriol, S. Fotopoulou, M. Frailis, E. Franceschi, S. Galeotta, B. Gillis, C. Giocoli, P. Gómez-Alvarez, A. Grazian, F. Grupp, L. Guzzo, S. V. H. Haugan, J. Hoar, H. Hoekstra, W. Holmes, I. Hook, F. Hormuth, A. Hornstrup, P. Hudelot, K. Jahnke, M. Jhabvala, E. Keihänen, S. Kermiche, A. Kiessling, M. Kilbinger, T. Kitching, R. Kohley, B. Kubik, K. Kuijken, M. Kümmel, M. Kunz, H. Kurki-Suonio, O. Lahav, D. Le Mignant, S. Ligori, P. B. Lilje, V. Lindholm, I. Lloro, D. Maino,

E. Maiorano, O. Mansutti, O. Marggraf, K. Markovic, N. Martinet, F. Marulli, R. Massey, S. Maurogordato, H. J. McCracken, E. Medinaceli, M. Melchior, Y. Mellier, M. Meneghetti, E. Merlin, G. Meylan, J. J. Mohr, A. Mora, M. Moresco, L. Moscardini, R. Nakajima, R. C. Nichol, S.-M. Niemi, C. Padilla, S. Paltani, F. Pasian, K. Pedersen, W. J. Percival, V. Pettorino, S. Pires, G. Polenta, M. Poncet, L. A. Popa, L. Pozzetti, F. Raison, A. Renzi, J. Rhodes, G. Riccio, E. Romelli, M. Roncarelli, R. Saglia, D. Sapone, P. Schneider, T. Schrabback, A. Secroun, G. Seidel, S. Serrano, P. Simon, C. Sirignano, G. Sirri, J. Skottfelt, L. Stanco, P. Tallada-Crespí, A. N. Taylor, H. I. Teplitz, I. Tereno, R. Toledo-Moreo, I. Tutusaus, E. A. Valentijn, L. Valenziano, T. Vassallo, G. Verdoes Kleijn, Y. Wang, J. Weller, E. Zucca, C. Burigana, and V. Scottez. Euclid: Early Release Observations – Overview of the Perseus cluster and analysis of its luminosity and stellar mass functions. *Astronomy & Astrophysics*, 697:A11, May 2025. doi:10.1051/0004-6361/202450808.

Richard H. Cyburt, Brian D. Fields, Keith A. Olive, and Tsung-Han Yeh. Big bang nucleosynthesis: Present status. *Reviews of Modern Physics*, 88(1):015004, January 2016. doi:10.1103/RevModPhys.88.015004.

Bryce Cyr, Sandeep Kumar Acharya, and Jens Chluba. Soft photon heating: a semi-analytic framework and applications to 21-cm cosmology. *MNRAS*, 534(1):738–757, October 2024. doi:10.1093/mnras/stae2113.

Xinyu Dai, Joel N. Bregman, Christopher S. Kochanek, and Elena Rasia. On the Baryon Fractions in Clusters and Groups of Galaxies. *ApJ* , 719(1):119–125, August 2010. doi:10.1088/0004-637X/719/1/119.

Eleonora Di Valentino, Jackson Levi Said, Adam Riess, Agnieszka Pollo, Vivian Poulin, Adrià Gómez-Valent, Amanda Weltman, Antonella Palmese, Caroline D. Huang, Carsten van de Bruck, Chandra Shekhar Saraf, Cheng-Yu Kuo, Cora Uhlemann, Daniela Grandón, Dante Paz, Dominique Eckert, Elsa M. Teixeira, Emmanuel N. Saridakis, Eoin Ó. Colgáin, Florian Beutler, Florian Niedermann, Francesco Bajardi, Gabriela Barenboim, Giulia Gubitosi, Ilaria Musella, Indranil Banik, Istvan Szapudi, Jack Singal, Jaume Haro Cases, Jens Chluba, Jesús Torrado, Jurgen Mifsud, Karsten Jedamzik, Khaled Said, Konstantinos Dialektopoulos, Laura Herold, Leandros Perivolaropoulos, Lei Zu, Lluís Galbany, Louise Breuval, Luca Visinelli, Luis A. Escamilla, Luis A. Anchordoqui, M. M. Sheikh-Jabbari, Margherita Lembo, Maria Giovanna Dainotti, Maria Vincenzi, Marika Asgari, Martina Gerbino, Matteo Forconi, Michele Cantiello, Michele Moresco, Micol Benetti, Nils Schöneberg, Özgür Akarsu, Rafael C. Nunes, Reginald Christian Bernardo, Ricardo Chávez, Richard I. Anderson, Richard Watkins, Salvatore Capozziello, Siyang Li, Sunny Vagnozzi, Supriya Pan, Tommaso Treu, Vid Irsic, Will Handley, William Giarè, Yukei Murakami, Abdolali Banihashemi, Adèle Poudou, Alan Heavens, Alan Kogut, Alba Domi, Aleksander Łukasz Lenart, Alessandro Melchiorri, Alessandro Vadalà, Alexandra Amon, Alexander Bonilla Rivera, Alexander Reeves, Alexander Zhuk, Alfio Bonanno, Ali Övgün, Alice Pisani, Alireza Talebian, Amare Abebe, Amin Aboubrahim, Ana Luisa González Morán, András Kovács, Andreas Lymperis, Andreas Papatriantafyllou, Andrew R. Liddle, Andronikos Paliathanasis, Andrzej Borowiec, Anil Kumar Yadav, Anita Yadav, Anjan Ananda Sen, Anjitha John William, Anne Christine Davis, Anowar J. Shajib, Anthony Walters, Anto Idicherian Lonappan, Anton Chudaykin, Antonio Capodagli, Antonio da Silva, Antonio De Felice, Antonio Racioppi, Araceli Soler Oficial, Ariadna Montiel, Arianna Favale, Armando Bernui, Arrianne Crystal Velasco, Asta Heinesen, Athanasios Bakopoulos, Athanasios Chatzistavrakidis, Bahman Khanpour, Bangalore S. Sathyaprakash, Bartek Zgirski, Benjamin L'Huillier, Benoit Famaey, Bhuvnesh Jain, Bing Zhang, Biswajit Karmakar, Branko Dragovich, Brooks Thomas, Carlos Correa, Carlos G. Boiza, Catarina Marques, Celia Escamilla-Rivera, Charalampos Tzerefos, Chi Zhang, Chiara De Leo, Christian Pfeifer, Christine Lee, Christo

Venter, Cláudio Gomes, Clecio Roque De bom, Cristian Moreno-Pulido, Damianos Iosifidis, Dan Grin, Daniel Blixt, Dan Scolnic, Daniele Oriti, Daria Dobrycheva, Dario Bettoni, David Benisty, David Fernández-Arenas, David L. Wiltshire, David Sanchez Cid, David Tamayo, David Valls-Gabaud, Davide Pedrotti, Deng Wang, Denitsa Staicova, Despoina Totolou, Diego Rubiera-Garcia, Dinko Milaković, Dominic W. Pesce, Dominique Sluse, Duško Borka, Ebrahim Yusofi, Elena Giusarma, Elena Terlevich, Elena Tomasetti, Elias C. Vagenas, Elisa Fazzari, Elisa G. M. Ferreira, Elvis Barakovic, Emanuela Dimastrogiovanni, Emil Brinch Holm, Emil Mottola, Emre Özülker, Enrico Specogna, Enzo Brocato, Erik Jensko, Erika Antonette Enriquez, Esha Bhatia, Fabio Bresolin, Felipe Avila, Filippo Bouchè, Flavio Bombacigno, Fotios K. Anagnostopoulos, Francesco Pace, Francesco Sorrenti, Francisco S. N. Lobo, Frédéric Courbin, Frode K. Hansen, Greg Sloan, Gabriel Farrugia, Gabriel Lynch, Gabriela Garcia-Arroyo, Gabriella Raimondo, Gaetano Lambiase, Gagandeep S. Anand, Gaspard Poulot, Genly Leon, Gerasimos Kouniatalis, Germano Nardini, Géza Csörnyei, and Giacomo Galloni. The CosmoVerse White Paper: Addressing observational tensions in cosmology with systematics and fundamental physics. *Physics of the Dark Universe*, 49:101965, September 2025. doi:10.1016/j.dark.2025.101965.

M. Dine, W. Fischler, and M. Srednicki. A simple solution to the strong CP problem with a harmless axion. *Physics Letters B*, 104:199–202, August 1981. doi:10.1016/0370-2693(81)90590-6.

Cora Dvorkin, Kfir Blum, and Marc Kamionkowski. Constraining dark matter-baryon scattering with linear cosmology. *PRD*, 89(2):023519, January 2014. doi:10.1103/PhysRevD.89.023519.

Chang Feng and Gilbert Holder. Enhanced Global Signal of Neutral Hydrogen Due to Excess Radiation at Cosmic Dawn. *ApJL* , 858(2):L17, May 2018. doi:10.3847/2041-8213/aac0fe.

E. Fermi. Eine statistische Methode zur Bestimmung einiger Eigenschaften des Atoms und ihre Anwendung auf die Theorie des periodischen Systems der Elemente. *Zeitschrift fur Physik*, 48 (1-2):73–79, January 1928. doi:10.1007/BF01351576.

Brian D. Fields, Keith A. Olive, Tsung-Han Yeh, and Charles Young. Big-bang nucleosynthesis after planck. *Journal of Cosmology and Astroparticle Physics*, 2020(03):010–010, March 2020. ISSN 1475-7516. doi:10.1088/1475-7516/2020/03/010. URL http://dx.doi.org/10.1088/1475-7516/2020/03/010.

D. J. Fixsen, A. Kogut, S. Levin, M. Limon, P. Lubin, P. Mirel, M. Seiffert, J. Singal, E. Wollack, T. Villela, and C. A. Wuensche. ARCADE 2 Measurement of the Absolute Sky Brightness at 3-90 GHz. *ApJ* , 734(1):5, June 2011. doi:10.1088/0004-637X/734/1/5.

Victor V. Flambaum and Ariel R. Zhitnitsky. Primordial lithium puzzle and the axion quark nugget dark matter model. *PRD*, 99(2):023517, January 2019. doi:10.1103/PhysRevD.99.023517.

Michael Mcneil Forbes, Kyle Lawson, and Ariel R. Zhitnitsky. Electrosphere of macroscopic "quark nuclei": A source for diffuse MeV emissions from dark matter. *PRD*, 82(8):083510, October 2010. doi:10.1103/PhysRevD.82.083510.

G. W. Fraser, A. M. Read, S. Sembay, J. A. Carter, and E. Schyns. Potential solar axion signatures in X-ray observations with the XMM–Newton observatory. *Mon. Not. Roy. Astron. Soc.*, 445(2): 2146–2168, 2014. doi:10.1093/mnras/stu1865.

Shuailiang Ge, Xunyu Liang, and Ariel Zhitnitsky. Cosmological C P -odd axion field as the coherent Berry's phase of the Universe. *PRD*, 96(6):063514, September 2017. doi:10.1103/PhysRevD.96.063514.

Shuailiang Ge, Xunyu Liang, and Ariel Zhitnitsky. Cosmological axion and a quark nugget dark matter model. *PRD*, 97(4):043008, February 2018. doi:10.1103/PhysRevD.97.043008.

Shuailiang Ge, Kyle Lawson, and Ariel Zhitnitsky. Axion quark nugget dark matter model: Size distribution and survival pattern. *PRD*, 99(11):116017, June 2019. doi:10.1103/PhysRevD.99.116017.

Shuailiang Ge, Hikari Rachmat, Md Shahriar Rahim Siddiqui, Ludovic Van Waerbeke, and Ariel Zhitnitsky. X-ray annual modulation observed by XMM-Newton and Axion Quark Nugget dark matter. *Physics of the Dark Universe*, 36:101031, June 2022. doi:10.1016/j.dark.2022.101031.

Vera Gluscevic and Kimberly K. Boddy. Constraints on Scattering of keV-TeV Dark Matter with Protons in the Early Universe. *PRL*, 121(8):081301, August 2018. doi:10.1103/PhysRevLett.121.081301.

P. W. Gorham, B. Rotter, P. Allison, O. Banerjee, L. Batten, J. J. Beatty, K. Bechtol, K. Belov, D. Z. Besson, W. R. Binns, V. Bugaev, P. Cao, C. C. Chen, C. H. Chen, P. Chen, J. M. Clem, A. Connolly, L. Cremonesi, B. Dailey, C. Deaconu, P. F. Dowkontt, B. D. Fox, J. W. H. Gordon, C. Hast, B. Hill, K. Hughes, J. J. Huang, R. Hupe, M. H. Israel, A. Javaid, J. Lam, K. M. Liewer, S. Y. Lin, T. C. Liu, A. Ludwig, L. Macchiarulo, S. Matsuno, C. Miki, K. Mulrey, J. Nam, C. J. Naudet, R. J. Nichol, A. Novikov, E. Oberla, M. Olmedo, R. Prechelt, S. Prohira, B. F. Rauch, J. M. Roberts, A. Romero-Wolf, J. W. Russell, D. Saltzberg, D. Seckel, H. Schoorlemmer, J. Shiao, S. Stafford, J. Stockham, M. Stockham, B. Strutt, G. S. Varner, A. G. Vieregg, S. H. Wang, and S. A. Wissel. Observation of an Unusual Upward-Going Cosmic-Ray-like Event in the Third Flight of ANITA. *PRL*, 121(16):161102, October 2018. doi:10.1103/PhysRevLett.121.161102.

Peter W. Gorham. Antiquark nuggets as dark matter: New constraints and detection prospects. *PRD*, 86(12):123005, December 2012. doi:10.1103/PhysRevD.86.123005.

Peter W. Graham and Davide Racco. Revisiting isocurvature bounds on the minimal QCD axion. *Journal of High Energy Physics*, 2025(12):28, December 2025. doi:10.1007/JHEP12(2025)028.

David J. Gross and Frank Wilczek. Ultraviolet Behavior of Non-Abelian Gauge Theories. *PRL*, 30 (26):1343–1346, June 1973. doi:10.1103/PhysRevLett.30.1343.

Richard Conn Henry, Jayant Murthy, James Overduin, and Joshua Tyler. The Mystery of the Cosmic Diffuse Ultraviolet Background Radiation. *ApJ* , 798(1):14, January 2015. doi:10.1088/0004-637X/798/1/14.

C. Hernández-Monteagudo. Constraining the arcade-2 excess with quijote and wmap data. Presentation at the 23rd Meeting MULTIDARK, Tenerife, Spain, 2026. URL https://indico.cern.ch/event/1665270/contributions/7138066/. Conference presentation, 19 June 2026.

Ryley Hill, Kiyoshi W. Masui, and Douglas Scott. The Spectrum of the Universe. *Applied Spectroscopy*, 72(5):663–688, May 2018. doi:10.1177/0003702818767133.

Lam Hui, Jeremiah P. Ostriker, Scott Tremaine, and Edward Witten. Ultralight scalars as cosmological dark matter. *PRD*, 95(4):043541, February 2017. doi:10.1103/PhysRevD.95.043541.

D. F. Jackson Kimball et al. Overview of the Cosmic Axion Spin Precession Experiment (CASPEr). 2017.

David M. Jacobs, Glenn D. Starkman, and Bryan W. Lynn. Macro dark matter. *MNRAS*, 450(4): 3418–3430, July 2015. doi:10.1093/mnras/stv774.

Frithjof Karsch. Lattice QCD at High Temperature and Density. In W. Plessas and L. Mathelitsch, editors, *Lectures on Quark Matter*, volume 583, page 209. 2002. doi:10.48550/arXiv.hep-lat/0106019.

J. E. Kim. Weak-interaction singlet and strong CP invariance. *Physical Review Letters*, 43:103–107, July 1979. doi:10.1103/PhysRevLett.43.103.

Jinsu Kim, Danho Ahn, Soohyung Lee, Saebyeok Ahn, Woohyun Chung, Ohjoon Kwon, Andrei Matlashov, Sergey V. Uchaikin, Boris I. Ivanov, Ki Woong Lee, Arjan Ferdinand van Loo, Yasunobu Nakamura, Seongtae Park, HeeSu Byun, Seonjeong Oh, Dojun Youm, and Yannis K. Semertzidis. First dedicated search for axion-quark-nugget dark matter. *PRD*, 112(12):L121305, December 2025. doi:10.1103/742y-g3fd.

Edward W. Kolb and Michael S. Turner. *The Early Universe*, volume 69 of *Frontiers in Physics*. Addison-Wesley, Redwood City, CA, 1990.

Pawan Kumar, Wenbin Lu, and Mukul Bhattacharya. Fast radio burst source properties and curvature radiation model. *MNRAS*, 468(3):2726–2739, July 2017. doi:10.1093/mnras/stx665.

Kyle Lawson and Ariel R. Zhitnitsky. Isotropic radio background from quark nugget dark matter. *Physics Letters B*, 724(1-3):17–21, July 2013a. doi:10.1016/j.physletb.2013.05.070.

Kyle Lawson and Ariel R. Zhitnitsky. Quark (Anti) Nugget Dark Matter. *arXiv e-prints*, art. arXiv:1305.6318, May 2013b. doi:10.48550/arXiv.1305.6318.

Kyle Lawson, Xunyu Liang, Alexander Mead, Md Shahriar Rahim Siddiqui, Ludovic Van Waerbeke, and Ariel Zhitnitsky. Gravitationally trapped axions on the Earth. *PRD*, 100(4):043531, August 2019. doi:10.1103/PhysRevD.100.043531.

Shun-Sheng Li, Hendrik Hildebrandt, and Ludovic Van Waerbeke. Probabilistic redshift estimation of unresolved galaxies from multi-band background light maps. *arXiv e-prints*, art. arXiv:2607.14525, July 2026. doi:10.48550/arXiv.2607.14525.

Xunyu Liang and Ariel Zhitnitsky. Axion field and the quark nugget's formation at the QCD phase transition. *PRD*, 94(8):083502, October 2016. doi:10.1103/PhysRevD.94.083502.

Xunyu Liang and Ariel Zhitnitsky. ANITA anomalous events and axion quark nuggets. *PRD*, 106 (6):063022, September 2022. doi:10.1103/PhysRevD.106.063022.

Xunyu Liang, Alexander Mead, Md Shahriar Rahim Siddiqui, Ludovic Van Waerbeke, and Ariel Zhitnitsky. Axion quark nugget dark matter: Time modulations and amplifications. *PRD*, 101 (4):043512, February 2020. doi:10.1103/PhysRevD.101.043512.

Xunyu Liang, Egor Peshkov, Ludovic Van Waerbeke, and Ariel Zhitnitsky. Proposed network to detect axion quark nugget dark matter. *PRD*, 103(9):096001, May 2021. doi:10.1103/PhysRevD.103.096001.

Tongyan Lin. TASI lectures on dark matter models and direct detection. *arXiv e-prints*, art. arXiv:1904.07915, April 2019. doi:10.48550/arXiv.1904.07915.

Wenbin Lu and Pawan Kumar. On the radiation mechanism of repeating fast radio bursts. *MNRAS*, 477(2):2470–2493, June 2018. doi:10.1093/mnras/sty716.

G. Lugones and J. E. Horvath. Color-flavor locked strange matter. *PRD*, 66(7):074017, October 2002. doi:10.1103/PhysRevD.66.074017.

G. Lugones and J. E. Horvath. Primordial nuggets survival and QCD pairing. *PRD*, 69(6):063509, March 2004. doi:10.1103/PhysRevD.69.063509.

Mathew S. Madhavacheril, Frank J. Qu, Blake D. Sherwin, Niall MacCrann, Yaqiong Li, Irene Abril-Cabezas, Peter A. R. Ade, Simone Aiola, Tommy Alford, Mandana Amiri, Stefania Amodeo, Rui An, Zachary Atkins, Jason E. Austermann, Nicholas Battaglia, Elia Stefano Battistelli, James A. Beall, Rachel Bean, Benjamin Beringue, Tanay Bhandarkar, Emily Biermann, Boris Bolliet, J. Richard Bond, Hongbo Cai, Erminia Calabrese, Victoria Calafut, Valentina Capalbo, Felipe Carrero, Anthony Challinor, Grace E. Chesmore, Hsiao-mei Cho, Steve K. Choi, Susan E. Clark, Rodrigo Córdova Rosado, Nicholas F. Cothard, Kevin Coughlin, William Coulton, Kevin T. Crowley, Roohi Dalal, Omar Darwish, Mark J. Devlin, Simon Dicker, Peter Doze, Cody J. Duell, Shannon M. Duff, Adriaan J. Duivenvoorden, Jo Dunkley, Rolando Dünner, Valentina Fanfani, Max Fankhanel, Gerrit Farren, Simone Ferraro, Rodrigo Freundt, Brittany Fuzia, Patricio A. Gallardo, Xavier Garrido, Jahmour Givans, Vera Gluscevic, Joseph E. Golec, Yilun Guan, Kirsten R. Hall, Mark Halpern, Dongwon Han, Ian Harrison, Matthew Hasselfield, Erin Healy, Shawn Henderson, Brandon Hensley, Carlos Hervías-Caimapo, J. Colin Hill, Gene C. Hilton, Matt Hilton, Adam D. Hincks, Renée Hložek, Shuay-Pwu Patty Ho, Zachary B. Huber, Johannes Hubmayr, Kevin M. Huffenberger, John P. Hughes, Kent Irwin, Giovanni Isopi, Hidde T. Jense, Ben Keller, Joshua Kim, Kenda Knowles, Brian J. Koopman, Arthur Kosowsky, Darby Kramer, Aleksandra Kusiak, Adrien La Posta, Alex Lague, Victoria Lakey, Eunseong Lee, Zack Li, Michele Limon, Martine Lokken, Thibaut Louis, Marius Lungu, Amanda MacInnis, Diego Maldonado, Felipe Maldonado, Maya Mallaby-Kay, Gabriela A. Marques, Jeff McMahon, Yogesh Mehta, Felipe Menanteau, Kavilan Moodley, Thomas W. Morris, Tony Mroczkowski, Sigurd Naess, Toshiya Namikawa, Federico Nati, Laura Newburgh, Andrina Nicola, Michael D. Niemack, Michael R. Nolta, John Orlowski-Scherer, Lyman A. Page, Shivam Pandey, Bruce Partridge, Heather Prince, Roberto Puddu, Federico Radiconi, Naomi Robertson, Felipe Rojas, Tai Sakuma, Maria Salatino, Emmanuel Schaan, Benjamin L. Schmitt, Neelima Sehgal, Shabbir Shaikh, Carlos Sierra, Jon Sievers, Cristóbal Sifón, Sara Simon, Rita Sonka, David N. Spergel, Suzanne T. Staggs, Emilie Storer, Eric R. Switzer, Niklas Tampier, Robert Thornton, Hy Trac, Jesse Treu, Carole Tucker, Joel Ullom, Leila R. Vale, Alexander Van Engelen, Jeff Van Lanen, Joshiwa van Marrewijk, Cristian Vargas, Eve M. Vavagiakis, Kasey Wagoner, Yuhan Wang, Lukas Wenzl, Edward J. Wollack, Zhilei Xu, Fernando Zago, and Kaiwen Zheng. The Atacama Cosmology Telescope: DR6 Gravitational Lensing Map and Cosmological Parameters. *ApJ* , 962(2):113, February 2024. doi:10.3847/1538-4357/acff5f.

Jes Madsen, Henning Heiselberg, and Karsten Riisager. Does strange matter evaporate in the early Universe\? *PRD*, 34(10):2947–2955, November 1986. doi:10.1103/PhysRevD.34.2947.

Fereshteh Majidi, Xunyu Liang, Ludovic Van Waerbeke, Ariel Zhitnitsky, Michael Sekatchev, Julian S. Sommer, Klaus Dolag, and Tiago Castro. The glow of axion quark nugget dark matter. Part I. Large scale structures. *JCAP*, 2024(9):045, September 2024a. doi:10.1088/1475-7516/2024/09/045.

Fereshteh Majidi, Xunyu Liang, Ludovic Van Waerbeke, Ariel Zhitnitsky, Michael Sekatchev, Julian S. Sommer, Klaus Dolag, and Tiago Castro. The Glow of Axion Quark Nugget Dark Matter: (I) Large Scale Structures. *JCAP, in press*, art. arXiv:2406.12122, June 2024b. doi:10.48550/arXiv.2406.12122.

Fereshteh Majidi, Xunyu Liang, Michael Sekatchev, Ludovic Van Waerbeke, and Ariel Zhitnitsky. The Glow of Axion Quark Nugget Dark Matter: (IV) CMB Spectral and Anisotropy Signatures. *arXiv e-prints*, art. arXiv:2512.05401, December 2025. doi:10.48550/arXiv.2512.05401.

David J. E. Marsh. Axion cosmology. *Physics Reports*, 643:1–79, July 2016. doi:10.1016/j.physrep.2016.06.005.

Luke McKay, Ravi Subrahmanyan, Aaron P. Chippendale, Pietro Bolli, Georgios Kyriakou, Alex Dunning, and Ronald Ekers. Precise measurement of the absolute sky brightness at 60-350 MHz. *Nature Astronomy*, 10(9):1398–1410, September 2026. doi:10.1038/s41550-026-02888-5.

Jayant Murthy, J. Michael Shull, Marc Postman, Joel Wm. Parker, Seth Redfield, Nathaniel Cunningham, G. Randall Gladstone, Jon P. Pineau, Pontus Brandt, Anne J. Verbiscer, Kelsi N. Singer, Harold A. Weaver, Richard C. Henry, and S. Alan Stern. Excess Ultraviolet Emission at High Galactic Latitudes: A New Horizons View. *Astronomical Journal*, 169(2):103, February 2025. doi:10.3847/1538-3881/ada4a4.

Jayant Murthy, James Overduin, Raj Manas, Amit Pathak, Snehanshu Saha, and Richard C. Henry. The Cosmic Ultraviolet Background at the Galactic Poles. *arXiv e-prints*, art. arXiv:2608.22231, August 2026. doi:10.48550/arXiv.2608.22231.

Ethan O. Nadler et al. Constraints on warm dark matter from milky way satellite galaxies. *Phys. Rev. Lett.*, 126:091101, 2021. doi:10.1103/PhysRevLett.126.091101.

David H. Oaknin and Ariel R. Zhitnitsky. 511 keV Photons from Color Superconducting Dark Matter. *PRL*, 94(10):101301, March 2005. doi:10.1103/PhysRevLett.94.101301.

Nathalie Palanque-Delabrouille et al. Constraints on warm dark matter from sdss lyman-alpha forest data. *JCAP*, 04:038, 2020. doi:10.1088/1475-7516/2020/04/038.

Particle Data Group, R. L. Workman, et al. Review of particle physics. *Progress of Theoretical and Experimental Physics*, 2024:083C01, 2024. doi:10.1093/ptep/ptae083.

R. D. Peccei and H. R. Quinn. Constraints imposed by CP conservation in the presence of pseudoparticles. *PRD*, 16:1791–1797, September 1977. doi:10.1103/PhysRevD.16.1791.

Roberto D. Peccei. The Strong CP Problem and Axions. In Markus Kuster, Georg Raffelt, and Berta Beltrán, editors, *Axions*, volume 741, page 3. 2008. doi:10.1007/978-3-540-73518-2_1.

W. Dean Pesnell, B. J. Thompson, and P. C. Chamberlin. The Solar Dynamics Observatory (SDO). *Sol. Phys.*, 275(1-2):3–15, January 2012. doi:10.1007/s11207-011-9841-3.

Cyril Pitrou, Alain Coc, Jean-Philippe Uzan, and Elisabeth Vangioni. Precision big bang nucleosynthesis with improved helium-4 predictions. *Physics Reports*, 754:1–66, September 2018. ISSN 0370-1573. doi:10.1016/j.physrep.2018.04.005. URL http://dx.doi.org/10.1016/j.physrep.2018.04.005.

Planck Collaboration, N. Aghanim, Y. Akrami, M. Ashdown, J. Aumont, C. Baccigalupi, M. Ballardini, A. J. Banday, R. B. Barreiro, N. Bartolo, S. Basak, R. Battye, K. Benabed, J. P. Bernard, M. Bersanelli, P. Bielewicz, J. J. Bock, J. R. Bond, J. Borrill, F. R. Bouchet, F. Boulanger, M. Bucher, C. Burigana, R. C. Butler, E. Calabrese, J. F. Cardoso, J. Carron, A. Challinor, H. C. Chiang, J. Chluba, L. P. L. Colombo, C. Combet, D. Contreras, B. P. Crill, F. Cuttaia, P. de Bernardis, G. de Zotti, J. Delabrouille, J. M. Delouis, E. Di Valentino, J. M. Diego, O. Doré, M. Douspis, A. Ducout, X. Dupac, S. Dusini, G. Efstathiou, F. Elsner, T. A. Enßlin, H. K. Eriksen, Y. Fantaye, M. Farhang, J. Fergusson, R. Fernandez-Cobos, F. Finelli, F. Forastieri, M. Frailis, A. A. Fraisse, E. Franceschi, A. Frolov, S. Galeotta, S. Galli, K. Ganga, R. T. Génova-Santos, M. Gerbino, T. Ghosh, J. González-Nuevo, K. M. Górski, S. Gratton, A. Gruppuso, J. E. Gudmundsson, J. Hamann, W. Handley, F. K. Hansen, D. Herranz, S. R. Hildebrandt, E. Hivon, Z. Huang, A. H. Jaffe, W. C. Jones, A. Karakci, E. Keihänen, R. Keskitalo, K. Kiiveri, J. Kim, T. S. Kisner, L. Knox, N. Krachmalnicoff, M. Kunz, H. Kurki-Suonio, G. Lagache, J. M. Lamarre, A. Lasenby, M. Lattanzi, C. R. Lawrence, M. Le Jeune, P. Lemos, J. Lesgourgues, F. Levrier,

A. Lewis, M. Liguori, P. B. Lilje, M. Lilley, V. Lindholm, M. López-Caniego, P. M. Lubin, Y. Z. Ma, J. F. Macías-Pérez, G. Maggio, D. Maino, N. Mandolesi, A. Mangilli, A. Marcos-Caballero, M. Maris, P. G. Martin, M. Martinelli, E. Martínez-González, S. Matarrese, N. Mauri, J. D. McEwen, P. R. Meinhold, A. Melchiorri, A. Mennella, M. Migliaccio, M. Millea, S. Mitra, M. A. Miville-Deschênes, D. Molinari, L. Montier, G. Morgante, A. Moss, P. Natoli, H. U. Nørgaard-Nielsen, L. Pagano, D. Paoletti, B. Partridge, G. Patanchon, H. V. Peiris, F. Perrotta, V. Pettorino, F. Piacentini, L. Polastri, G. Polenta, J. L. Puget, J. P. Rachen, M. Reinecke, M. Remazeilles, A. Renzi, G. Rocha, C. Rosset, G. Roudier, J. A. Rubiño-Martín, B. Ruiz-Granados, L. Salvati, M. Sandri, M. Savelainen, D. Scott, E. P. S. Shellard, C. Sirignano, G. Sirri, L. D. Spencer, R. Sunyaev, A. S. Suur-Uski, J. A. Tauber, D. Tavagnacco, M. Tenti, L. Toffolatti, M. Tomasi, T. Trombetti, L. Valenziano, J. Valiviita, B. Van Tent, L. Vibert, P. Vielva, F. Villa, N. Vittorio, B. D. Wandelt, I. K. Wehus, M. White, S. D. M. White, A. Zacchei, and A. Zonca. Planck 2018 results. VI. Cosmological parameters. *Astronomy & Astrophysics*, 641:A6, September 2020. doi:10.1051/0004-6361/201833910.

H. David Politzer. Reliable perturbative results for strong interactions? *Phys. Rev. Lett.*, 30:1346–1349, Jun 1973. doi:10.1103/PhysRevLett.30.1346. URL https://link.aps.org/doi/10.1103/PhysRevLett.30.1346.

Andrew Pontzen and Fabio Governato. How supernova feedback turns dark matter cusps into cores. *MNRAS*, 421(4):3464–3471, April 2012. doi:10.1111/j.1365-2966.2012.20571.x.

Krishna Rajagopal and Frank Wilczek. The Condensed Matter Physics of QCD. In M. Shifman, editor, *At the Frontier of Particle Physics: Handbook of QCD (in 3 Vols). Edited by SHIFMAN M. Published by World Scientific Publishing Co. Pte. Ltd*, pages 2061–2151. 2001. doi:10.1142/9789812810458_0043.

Nayyer Raza, Ludovic Van Waerbeke, and Ariel Zhitnitsky. Solar corona heating by axion quark nugget dark matter. *PRD*, 98(10):103527, November 2018. doi:10.1103/PhysRevD.98.103527.

C. L. Reichardt, S. Patil, P. A. R. Ade, A. J. Anderson, J. E. Austermann, J. S. Avva, E. Baxter, J. A. Beall, A. N. Bender, B. A. Benson, F. Bianchini, L. E. Bleem, J. E. Carlstrom, C. L. Chang, P. Chaubal, H. C. Chiang, T. L. Chou, R. Citron, C. Corbett Moran, T. M. Crawford, A. T. Crites, T. de Haan, M. A. Dobbs, W. Everett, J. Gallicchio, E. M. George, A. Gilbert, N. Gupta, N. W. Halverson, N. Harrington, J. W. Henning, G. C. Hilton, G. P. Holder, W. L. Holzapfel, J. D. Hrubes, N. Huang, J. Hubmayr, K. D. Irwin, L. Knox, A. T. Lee, D. Li, A. Lowitz, D. Luong-Van, J. J. McMahon, J. Mehl, S. S. Meyer, M. Millea, L. M. Mocanu, J. J. Mohr, J. Montgomery, A. Nadolski, T. Natoli, J. P. Nibarger, G. Noble, V. Novosad, Y. Omori, S. Padin, C. Pryke, J. E. Ruhl, B. R. Saliwanchik, J. T. Sayre, K. K. Schaffer, E. Shirokoff, C. Sievers, G. Smecher, H. G. Spieler, Z. Staniszewski, A. A. Stark, C. Tucker, K. Vanderlinde, T. Veach, J. D. Vieira, G. Wang, N. Whitehorn, R. Williamson, W. L. K. Wu, and V. Yefremenko. An Improved Measurement of the Secondary Cosmic Microwave Background Anisotropies from the SPT-SZ + SPTpol Surveys. *ApJ* , 908(2):199, February 2021. doi:10.3847/1538-4357/abd407.

V. C. Rubin, W. K. Ford, Jr., and N. Thonnard. Rotational properties of 21 SC galaxies with a large range of luminosities and radii, from NGC 4605 (R=4kpc) to UGC 2885 (R=122kpc). *ApJ* , 238:471–487, June 1980. doi:10.1086/158003.

Vera C. Rubin and W. Kent Ford, Jr. Rotation of the Andromeda Nebula from a Spectroscopic Survey of Emission Regions. *ApJ* , 159:379, February 1970. doi:10.1086/150317.

Stefan B. Rüster, Verena Werth, Michael Buballa, Igor A. Shovkovy, and Dirk H. Rischke. Phase diagram of neutral quark matter: Self-consistent treatment of quark masses. *PRD*, 72(3): 034004, August 2005. doi:10.1103/PhysRevD.72.034004.

Ken'ichi Saikawa, Javier Redondo, Alejandro Vaquero, and Mathieu Kaltschmidt. Spectrum of global string networks and the axion dark matter mass. *JCAP*, 2024(10):043, October 2024. doi:10.1088/1475-7516/2024/10/043.

Michael Sekatchev, Xunyu Liang, Fereshteh Majidi, Ben Scully, Ludovic Van Waerbeke, and Ariel Zhitnitsky. The Glow of Axion Quark Nugget Dark Matter: (III) The Mysteries of the Milky Way UV Background. *arXiv e-prints*, art. arXiv:2504.15382, April 2025. doi:10.48550/arXiv.2504.15382.

M. A. Shifman, A. I. Vainshtein, and V. I. Zakharov. Can confinement ensure natural CP invariance of strong interactions? *Nuclear Physics B*, 166:493–506, April 1980. doi:10.1016/0550-3213(80)90209-6.

Julian S. Sommer, Klaus Dolag, Ludwig M. Böss, Ildar Khabibullin, Xunyu Liang, Ludovic Van Waerbeke, Ariel Zhitnitsky, Fereshteh Majidi, Jenny G. Sorce, Benjamin Seidel, and Elena Hernández-Martínez. The glow of axion quark nugget dark matter: II. Galaxy clusters. *Astronomy & Astrophysics*, 691:A38, November 2024. doi:10.1051/0004-6361/202451316.

David N. Spergel and Paul J. Steinhardt. Observational Evidence for Self-Interacting Cold Dark Matter. *PRL*, 84(17):3760–3763, April 2000. doi:10.1103/PhysRevLett.84.3760.

Julia Stadler and Céline Bœhm. Constraints on γ-CDM interactions matching the Planck data precision. *JCAP*, 2018(10):009, October 2018. doi:10.1088/1475-7516/2018/10/009.

Max Tegmark and Matias Zaldarriaga. Separating the early universe from the late universe: Cosmological parameter estimation beyond the black box. *PRD*, 66(10):103508, November 2002. doi:10.1103/PhysRevD.66.103508.

L. H. Thomas. The calculation of atomic fields. *Proceedings of the Cambridge Philosophical Society*, 23(5):542, January 1927. doi:10.1017/S0305004100011683.

M. Tristram, A. J. Banday, K. M. Górski, R. Keskitalo, C. R. Lawrence, K. J. Andersen, R. B. Barreiro, J. Borrill, L. P. L. Colombo, H. K. Eriksen, R. Fernandez-Cobos, T. S. Kisner, E. Martínez-González, B. Partridge, D. Scott, T. L. Svalheim, and I. K. Wehus. Improved limits on the tensor-to-scalar ratio using BICEP and Planck data. *PRD*, 105(8):083524, April 2022. doi:10.1103/PhysRevD.105.083524.

Sean Tulin and Hai-Bo Yu. Dark matter self-interactions and small scale structure. *Physics Reports*, 730:1–57, February 2018. doi:10.1016/j.physrep.2017.11.004.

Tammay Vachaspati and Alexander Vilenkin. Formation and evolution of cosmic strings. *Phys. Rev. D*, 30:2036–2045, Nov 1984. doi:10.1103/PhysRevD.30.2036. URL https://link.aps.org/doi/10.1103/PhysRevD.30.2036.

Ludovic Van Waerbeke and Ariel Zhitnitsky. Fast radio bursts and the axion quark nugget dark matter model. *PRD*, 99(4):043535, February 2019. doi:10.1103/PhysRevD.99.043535.

A. Vilenkin and E. P. S. Shellard. *Cosmic Strings and Other Topological Defects*. Cambridge University Press, Cambridge, 1994. ISBN 9780521654760.

Steven Weinberg. *The Quantum Theory of Fields, Volume 2: Modern Applications*. Cambridge University Press, Cambridge, 1996. ISBN 978-0521550025.

Ryan J. Wilkinson, Julien Lesgourgues, and C. {é. }line Bœhm. Using the CMB angular power spectrum to study Dark Matter-photon interactions. *JCAP*, 2014(4):026, April 2014. doi:10.1088/1475-7516/2014/04/026.

Edward Witten. Cosmic separation of phases. *Phys. Rev. D*, 30:272–285, Jul 1984. doi:10.1103/PhysRevD.30.272. URL https://link.aps.org/doi/10.1103/PhysRevD.30.272.

A. R. Zhitnitsky. On Possible Suppression of the Axion Hadron Interactions. (In Russian). *Sov. J. Nucl. Phys.*, 31:260, 1980. [Yad. Fiz.31,497(1980)].

Ariel Zhitnitsky. Cold dark matter as compact composite objects. *PRD*, 74(4):043515, August 2006. doi:10.1103/PhysRevD.74.043515.

Ariel Zhitnitsky. Solar Extreme UV radiation and quark nugget dark matter model. *JCAP*, 2017 (10):050, October 2017. doi:10.1088/1475-7516/2017/10/050.

Ariel Zhitnitsky. Axion quark nuggets. Dark matter and matter-antimatter asymmetry: Theory, observations and future experiments. *Modern Physics Letters A*, 36(18):2130017, June 2021. doi:10.1142/S0217732321300172.

Ariel Zhitnitsky. Neutron stars as dark matter detectors. *PRD*, 109(6):063018, March 2024. doi:10.1103/PhysRevD.109.063018.

Ariel Zhitnitsky and Marios Maroudas. Mysterious Anomalies in Earth's Atmosphere and Strongly Interacting Dark Matter. *Symmetry*, 17(1):79, January 2025. doi:10.3390/sym17010079.

Ariel R. Zhitnitsky. 'Nonbaryonic' dark matter as baryonic colour superconductor. *JCAP*, 2003 (10):010, October 2003. doi:10.1088/1475-7516/2003/10/010.

F. Zwicky. Die Rotverschiebung von extragalaktischen Nebeln. *Helvetica Physica Acta*, 6:110–127, January 1933.